Alma Mater Studiorum · University of Bologna

SCHOOL OF SCIENCE
Physics Degree Course

Pulse Shape Studies of Neutral Particles with a Liquid Scintillator

Supervisor:
Prof. Cristian Massimi

Presented by:
Lucia Salvi

Co-Supervisor:
Dr.ssa Sofia Colombi

extraordinary session
Academic Year 2021 - 2022

Al mio papà... ancora più che mai

Abstract

The hadrontherapy exploits beams of charged particles such as protons, carbon and oxygen against deep cancers. These ions have a depth-dose profile in which there is a little release of energy at the beginning of their path, whereas there is a sharp maximum, the *Bragg Peak*, near its end path. Furthermore, ions such as carbon or oxygen, that are heavier then protons, have a better biological effectiveness at the Bragg peak and so they can be used to cure hypoxic cancers. However, if heavier ions are used, the fragmentation of the projectile can happen and the fragments can release some dose outside the treatment volume beyond the Bragg peak. The fragmentation process takes place also when the *Galactic Cosmic Rays* at high energy hit the spaceship during space missions. In both cases some neutrons can be produced and if they interact with the absorbing materials nuclei some secondary particles are generated which can release energy. For this reason, studies about the cross section measurements of the fragments generated during the collisions of heavy ions against the tissues nuclei are very important. In this context, the *FragmentatiOn Of Target* (FOOT) experiment was born, and aims at measuring the differential and double differential fragmentation cross sections for different kinetic energies relevant to hadrontherapy and space radioprotection with high accuracy. Since during fragmentation processes also neutrons are produced, tests of a neutron detection system are ongoing. In particular, recently a neutron detector made up of a liquid organic scintillator, BC-501A with neutrons/gammas discrimination capability was studied, and it represents the core of this thesis. More in details, an analysis of the data collected at the GSI laboratory, in Darmstadt, Germany, is effectuated which consists in discriminating neutral and charged particles and then to separate neutrons from gammas. From this analysis, a preliminary energy-differential reaction cross-section for the production of neutrons in the $^{16}\mathrm{O} + (\mathrm{C_2H_4})_n$ and $^{16}\mathrm{O} + \mathrm{C}$ reactions was estimated.

Contents

Introduction

Nowadays, it is estimated that globally one in five people will suffer from cancer during their lifetime as delineated in the report *Global Cancer Statistic 2020* written by the *American Cancer Society* (ACS) and the *International Agency for Research on Cancer* (IARC). In this document it is also said that the new cases of tumor in the world are 19.3 million and the deaths caused by cancer are 10 millions. For what concern Italy, every year there are 377·000 new diagnosis of cancer and only in 2021 the deaths were 181·330 which was a lower number with respect to the European ones. In medical clinics, several treatments are used to defeat cancer which contemplate surgery, radiotherapy, chemotherapy, immunotherapy and newly hadrontherapy. These treatments can be used alone or put together. Recent studies have shown that the radiotherapy is fundamental in 50% of cancer, so it is essential for 7 million new patients in the world every year. In conjunction with the well-established radiotherapy which uses photons, the hadrontherapy is also used and the number of patients treated with the latter treatment is growing up. Only in Italy, the number of people with cancer and treated with hadrontherapy is grown of over the 40% in the 2017 and it is still growing today.

The hadrontherapy makes use of the heavy charged particle behaviour when they lose their energy inside a material. It consists in treating patient with a beam of protons or charged nuclei up to oxygen ^{16}O, that release just a little quantity of their energy at the entrance, whereas they loose the majority of their energy in the last part of their path, where there is the treatment volume. The peak in which there is the maximum release of energy is called *Bragg peak* whose profundity in the patient body depends on the initial energy of the beam. If the Bragg peak of protons and the one of heavier ions are compared, it is found that heavy ions have a better biological effectiveness with respect to protons and so they can be used in hypoxic cancers in order to obtain the same effect with a minor dose. On the other hand, the fragmentation of the projectile and of the target can take place in the hadrontherapy causing the appearance of secondary charged particles and also neutrons. If the beam is composed of heavy ions and the fragmentation of the projectile happens, the produced fragments, that have equal velocity of the projectile but a lesser mass, can go further and release some dose over the Bragg peak in healthy tissues. In the protontherapy instead the target is fragmented and the produced fragments have a small path and so they release their energy locally. For this reason, this latter process

is more important in the entrance part of the beam where there are healthy tissues that can be harmed.

The fragmentation process is also important in the space radio-protection field. Since the beginning of the human flight in space it was found that energetic charged particles can cause health risks to astronauts. The first missions did not last a long time, usually some hours or days and they were restricted only to the *Low Earth Orbit* (LEO) where the explorers were exposed to solar particles or trapped radiation not at high energy. Therefore, in the LEO region there is the geomagnetic shielding against the *Galactic Cosmic Rays* (GCR), that consist in protons 90%, helium 9% and heavy ions 1% at very high energy, and there is also the protection given by the Earth that can stop in part the fluxes of particles. During these missions the explorers were exposed to a little but constant dose rate of $100-300$ μGy/day. The dose contribution in these area is equally given by the solar particles, which is composed of high energy protons, and trapped radiations; so, if the solar particles are not present the total dose is well below 1 mGy/day. Even if these rates are higher with respect to the one on Earth, which is 4 mSv/year, they do not represent a concern for missions which last few days or weeks because they are well below the threshold for acute diseases and they will not remarkably increase the probability to give rise to a fatal cancer during the lifetime of the astronauts. In the next year instead, several missions regarding the exploration of the Solar System, in particular a round-trip to Mars and long term expeditions to explore the Moon, are in program. The astronauts should be able to explore the space without being exposed to a very high radiation dose giving rise to risks for their health. In fact they would be exposed to radiation emitted from the sun and to space radiation, that consists in low levels of heavy charged particle, without having the protection given by the magnetosphere. These radiations can cause damages to biological materials but also to shielding materials. In particular, the GCR are very dangerous because they are very energetic and the majority of them tends to pass through the moderate shielding of the spaceship. In order to limit the exposure, shields are used to fragment the incoming particles to reduce the flux of heavy ions. For this reason materials that maximize the fragmentation are the chosen ones to reduce the exposure to high energy radiation. Nowadays, the studies regarding the cross section measurements of the fragments produced in the collisions between heavy ions and the nuclei of the tissues (hydrogen, carbon, calcium, oxygen or nitrogen) are not enough. In this context the *FragmentatiOn Of Target* (FOOT) experiment aims to perform precise measurements of the nuclear cross sections in two distinct fields: the hadrontherapy and radio-protection in space. Since the charged particles that pass through the patient can undergo nuclear interaction and produce fragments, a precise estimation of these process has to be carried out at the hadrontherapy energies, $150-400$ MeV/u, in order to optimize the treatment accuracy. For what concern the second purpose of FOOT, the energy range of the GCR goes from 700 MeV/u up to 1000 MeV/u. So the measurements done for the hadrontherapy can be superposed with the ones regarding the radio-protection in space, with the only difference given by the energy range. To reach the FOOT purposes,

the experiment exploits the inverse kinematics in order to overcome the problem represented by the particles with a very low path that would be very difficult to detect. Since using a target made of hydrogen can cause some problems, it is exploited the subtraction between the cross section on carbon and polyethylene. The experimental apparatus consists into a *Start Counter*, *Beam Monitor*, *Silicon Pixel Vertex Detector*, *Silicon Pixel Inner Tracker*, *Permanent Magnets*, *Silicon microStrips*, *TOF Wall*, *BGO calorimeter* and another setup in which it is used an *Emulsion Spectrometer* to do the cross-section measurements of the lighter fragments. It is also necessary to detect neutrons because, even if they are neutral particles, they can interact with absorbing material nuclei. In this way the neutrons are replaced by one or more secondary particles or they change their energy and direction. The secondary particles however are heavy charged particles produced by neutrons-induced nuclear reactions or they are the nuclei of the material that have acquired the energy from the neutrons during the collisions. These secondary charged particles can damage the body tissue and the shielding materials of spaceship. For this reason in the FOOT experiment a neutron detection system is introduced consisting in the BC-501A detector which is a liquid organic scintillator designed to detect neutrons in presence of gamma radiation by applying the *Pulse Shape Discrimination* method. In this analysis, the pulse shape discrimination has been applied to the data obtained by a beam of oxygen ^{16}O at 200 and 400 MeV/u against targets made of carbon and polyethylene with a thickness of 1.0 cm or 0.5 cm. In this way the neutrons and the photons are discriminated and it is possible to reconstruct the kinetic energy and the cross section differentiated in kinetic energy of emitted neutrons.

In Chapter 1, it is described the interaction of particles with matter introducing the concept of energy loss, mean range, energy straggling and nuclear fragmentation process. Also the neutral particles, neutrons and photons, are taken into account and their interactions with a medium are reported. Then, the biological effects of radiations are illustrated together with the most important dosimetric unities. In the end, a description of the hadrontherapy and space radio-protection is done in order to introduce the reasons behind the FOOT experiment.

In Chapter 2, the FOOT experimental setup is illustrated together with the neutron detectors, the BC-501A scintillator, whose main characteristic are, then, reported.

In Chapter 3, the data analysis is discussed. First of all the setup of the experiment performed at the GSI, in Darmstadt, Germany, is described then the analysis procedure is explained. In particular, the charged and neutral particles are discriminated by using a plastic scintillator as the veto for charged particles, than the amplitude, the time of flight and the area fast and slow of each digitized signal are extracted and used to discriminates neutrons from gammas. Once the neutrons are selected, their kinetic energy is reconstructed using the time-of-flight technique. Finally, the energy-differential neutron yield is estimated. Since the statistic accumulated in the measurement campaign is rather small, this thesis represents a first step in the direction of studying neutrons in FOOT experiment. In summary, the aim of this project was to study neutron detector

performances and related analysis procedure.

Chapter 1

Particles interaction with matter

1.1 Charged particles interaction with matter

When a charged particle passes through a material it will loss some of its energy and it will be deflected with respect to its original direction mainly due to the inelastic scattering with the electrons of the atoms. During this process, the particle transfers part of its energy to the material atoms causing the ionization or excitation of the latter ones. Although the amount of energy loss in each collision is a very small fraction of the charged particle total kinetic energy, in a dense material the particle makes more collisions for the same path length than in a less dense one and therefore the amount of energy loss results to be larger. When atomic collisions take place, there could be two final scenarios: in the first one the energy transferred is particularly small and only excitation can happened, whereas in the second case the energy transmitted is enough to cause the ionization of the atom. The first sample is called *soft collision*, whereas the second one is named *hard collision*.
Although the elastic scattering with nuclei can occur, it is much less frequent than scattering with electrons. Usually, in the elastic scattering of nuclei the quantity of energy transferred is low because the nuclear masses of most the materials are larger than the one of the incident particle. If this is not the case, some energy can be lost also with this process. Anyway, most of the energy is lost through collisions with atomic electrons.
Since the number of inelastic collisions in a large path length is high, it is possible to introduce the concept of average energy loss per unit of path length which is called *stopping power* and it is described by the Bethe-Bloch formula.

1.1.1 The Bethe-Bloch formula

The formula obtained by Bethe and Bloch [1] taking into account the quantum-mechanical calculations can be written as

$$-\frac{dE}{dx} = 2\pi N_a r_e^2 m_e c^2 \rho \frac{Z}{A}\frac{z^2}{\beta^2}\left[\ln\left(\frac{2m_e\gamma^2 v^2 W_{max}}{I^2}\right) - 2\beta^2\right] \tag{1.1}$$

where $2\pi N_a r_e^2 m_e c^2 = 0.1535$ MeV cm^2/g. The parameters of Eq. (1.1) are the following:

- r_e acts for the classical electron radius which is equal to 2.817×10^{-13} cm;
- m_e represents the electron mass;
- N_a stands for the Avogadro number that amounts to 6.022×10^{23} particles/mol;
- I denotes the mean excitation potential;
- Z indicates the absorbing material atomic number;
- A illustrates the absorbing material atomic weight;
- ρ symbolises the absorbing material density;
- z depicts the incident particle charge in units of e;
- β is the incident particle v/c;
- γ is the Lorentz factor, is equal to $1/\sqrt{1-\beta^2}$

The energy transfer in a single collision is maximum when the collision is a head-on one; if the incident particle has a mass M its expression can be parametrized as:

$$W_{max} = \frac{2m_e c^2 \eta^2}{1 + 2s\sqrt{1+\eta^2} + s^2} \tag{1.2}$$

in which $s = m_e/M$ and $\eta = \beta\gamma$. In case $M >> m_e$ the maximum energy transferred can be rewritten as:

$$W_{max} \simeq 2m_e c^2 \eta^2 \tag{1.3}$$

Two corrections are usually added to Eq. (1.1): the density correction, δ, and the shell correction, C. They are important at high and low energy, respectively. The density correction is due to the polarisation of the atoms along the particle path caused by the electric field of the particle itself. In this way, if an electron is not near to the particle path it will be shielded by the entire intensity of the electric field. So the collisions with the outer lying electrons will give a little contribution to the total energy loss. However,

this effect becomes more relevant when the energy of the particle grows and when the material density grows because in this case the induced polarisation is considerable.
The shell correction plays a role when the incident particle velocity is similar or smaller than the one of the orbital bounded electrons because, in this case, it is not possible to assume that the electron is stationary with respect to the incoming particle as it was supposed during the Bethe-Bloch formula derivation.
In this case the Bethe-Bloch formula can be rewritten as

$$-\frac{dE}{dx} = 2\pi N_a r_e^2 m_e c^2 \rho \frac{Z}{A}\frac{z^2}{\beta^2}\left[\ln\left(\frac{2m_e\gamma^2 v^2 W_{max}}{I^2}\right) - 2\beta^2 - \delta - 2\frac{C}{Z}\right] \tag{1.4}$$

in which δ expresses the density correction, C denotes the shell correction and W_{max} is the maximum energy which is transferred during a single collision.
In Figure 1.1, it possible to compare the Bethe-Bloch formula trend with and without the corrections described above.

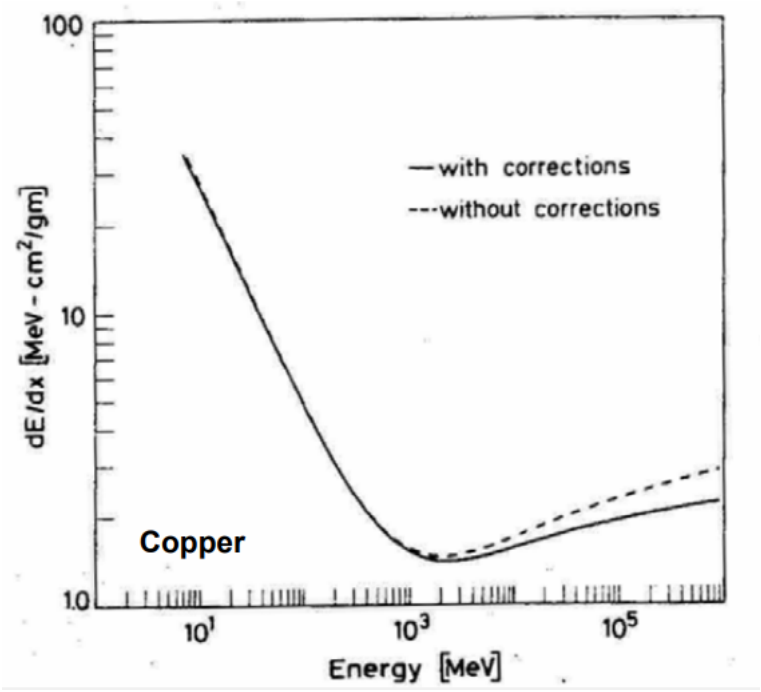

Figure 1.1: *Bethe Bloch formula when the density and the shell corrections are considered and also when these corrections are not contemplated. Copper is the material used* [2].

The stopping power described by Eq. (1.1) is valid, with an accuracy of few %, if the velocity of the particle is $0.05 < \beta\gamma < 10^3$ for material with an intermediate atomic number [1]. In this formula it is possible to notice that there is a dependence on the material density which means that for a more dense material there will be a higher

number of collisions and consequently a larger energy loss. The Bethe-Bloch equation is also a function of the Z/A ratio of the material which means that the energy loss becomes almost constant for a large variety of materials. In fact, the ratio between the atomic and mass number is more or less equal to 1/2 for light nuclei, and it becomes smaller when the nuclei are heavier because there are more neutrons than protons in the material nucleus. Another dependence present in the formula is given by the particle charge according to which the energy loss per unit of path length increases with the squared charge of the particle. Consequently, different particles with the same velocity will lose the same energy if they have equal charge. Furthermore, the stopping power described above has a dependence on the energy as it is represented in Figure 1.2.

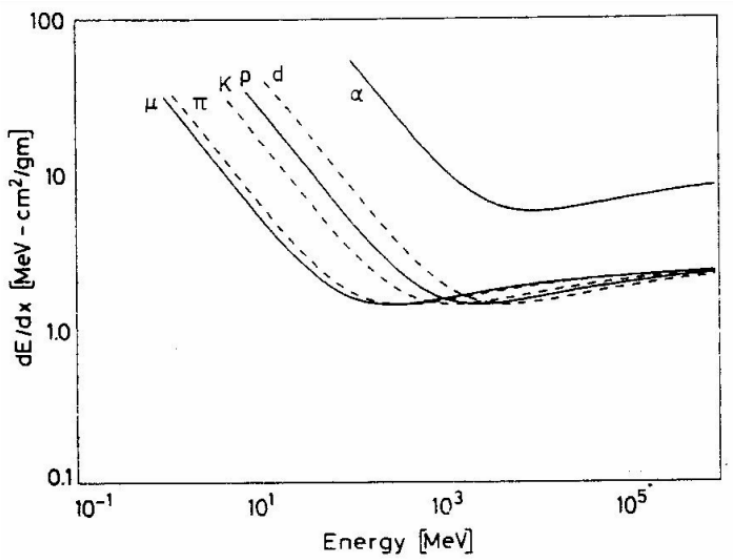

Figure 1.2: *Dependence of the stopping power on the energy of several particles* [1].

If the energies are not relativistic, dE/dx is ruled by the $1/\beta^2$ component which is the inverse of the square of the particle speed. The trend tends to diminish if the velocity grows up until a minimum is reached when $\beta\gamma = 3 - 4$ [3] as it is shown in Figure 1.3.

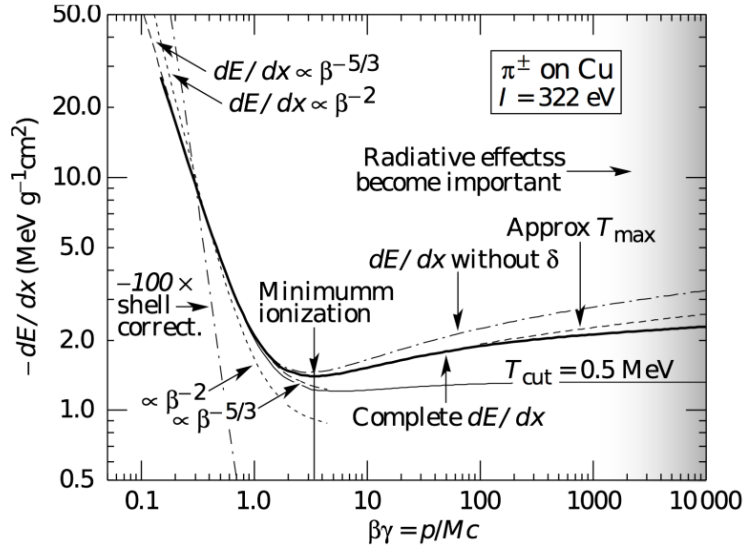

Figure 1.3: *dE/dx as a function of $\beta\gamma$ for pions on copper. It is possible to see the minimum which is reached when $\beta\gamma = 3 - 4$ [3].*

This minimum has more or less the same value for all the particles that have the same charge. Beyond this point, as the energy increases, the factor $1/\beta^2$ tends to one whereas the dE/dx grows up because of the logarithmic dependence of the Eq. 1.4. The relativistic growth is then balanced by the correction due to the density factor.
It is important to recall that when the kinetic energy is very small, the Bethe-Bloch's formula is no longer valid. In fact, it can be shown that the dE/dx rises until a maximum and then goes steeply down. In this region the particle tends to take up electrons and so the particle effective charge turns out to be less as well as its energy loss. The effective charge, which substitutes the particle charge, z, in Eq. (1.4), can be described by the Barka's formula [4] which is:

$$z_{eff} = z\left[1 - exp\left(-125\beta z^{-2/3}\right)\right] \tag{1.5}$$

The full behaviour of the stopping power of a charged particle for example a muon with a positive charge, is shown in Figure 1.4.

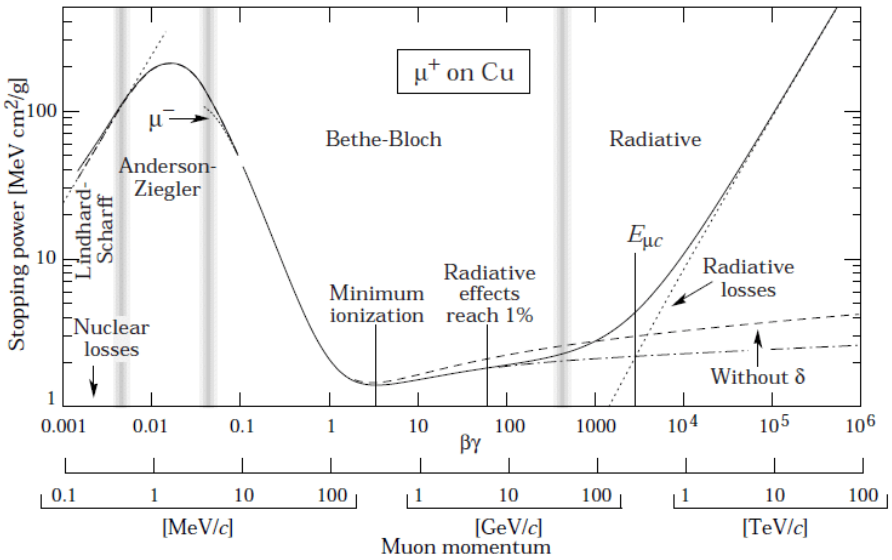

Figure 1.4: *Total stopping power of a positive muon in copper in function of $\beta\gamma$. As it is possible to see there are four region that describe the energy loss: the Lindhard-Scharff, the Anderson-Ziegler, the Bethe-Bloch and the Radiative region* [3].

One consequence of the dE/dx behaviour as a function of β is the Bragg peak, reported in Figure 1.5, in which the curves represent the energy release along the range of each particle. In Figure 1.5 is reported the Bragg peak, where there is the highest released of energy, for carbon ions at 250 and 300 MeV per nucleon (MeV/u). It is possible to notice that the position of the peak depends on the initial energy of the charged particle.

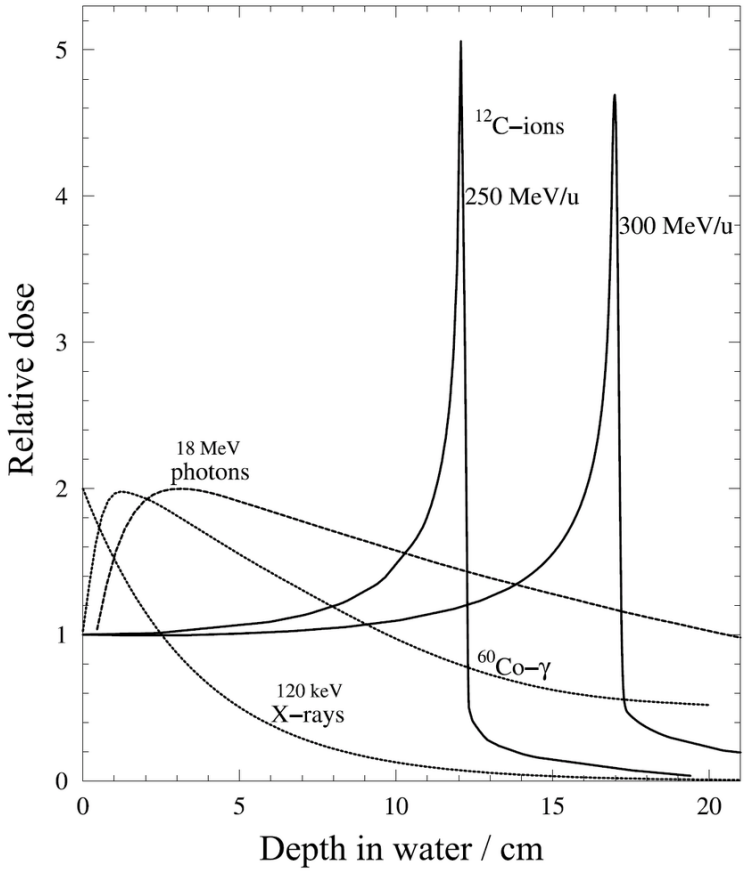

Figure 1.5: *Energy profile for different beams in function of the depth in water. The profile of γ-rays or x-rays has a behaviour in which the dose distribution tends to diminish with increasing depth. The hadrons instead have a behaviour which is the opposite with respect to the one of the γ-rays and x-rays: in fact, in the end of the range there is the maximum of the energy which is the Bragg peak* [5].

This behaviour clearly shows the reason why hadrons are used in hadrontherapy as it is described in section 1.5.

1.1.2 Mean range, energy straggling

By knowing the particle type, the initial energy and the material, it is possible to calculate the range of the particle, i.e. the distance travelled by the particle in matter before losing all its energy. The mean range of a particle, with initial kinetic energy equal to E_0, is expressed as:

$$S(E_0) = \int_0^{E_0} \left(\frac{dE}{dx}\right)^{-1} dE, \tag{1.6}$$

From Eq. (1.6) it follows that the path length becomes longer when the kinetic energy of the incoming particle grows up. However, the energy loss is a statistical process. This means that even if two equivalent particles with the same initial energy are considered, they will not undergo the same number of collisions and therefore they will not lose the same amount of energy. It follows that the total energy loss is given by the sum of the infinitesimal energy loss δE in each one of the N collisions. Therefore, the total energy loss has fluctuations and it is a mean value which is equal to:

$$\Delta E = \sum_{n=1}^{N} \delta E_n, \tag{1.7}$$

The energy transfer does not take place under a certain value called *excitation threshold* and the probability of energy transferred is larger for small energy losses which coincide with distant collisions [6]. Instead, collisions with large energy losses have a little probability to happen. The probability distribution of δE is asymmetric and this phenomenon is named *energy straggling*. An example is shown in Figure 1.6, where the straggling function for pions is reported.

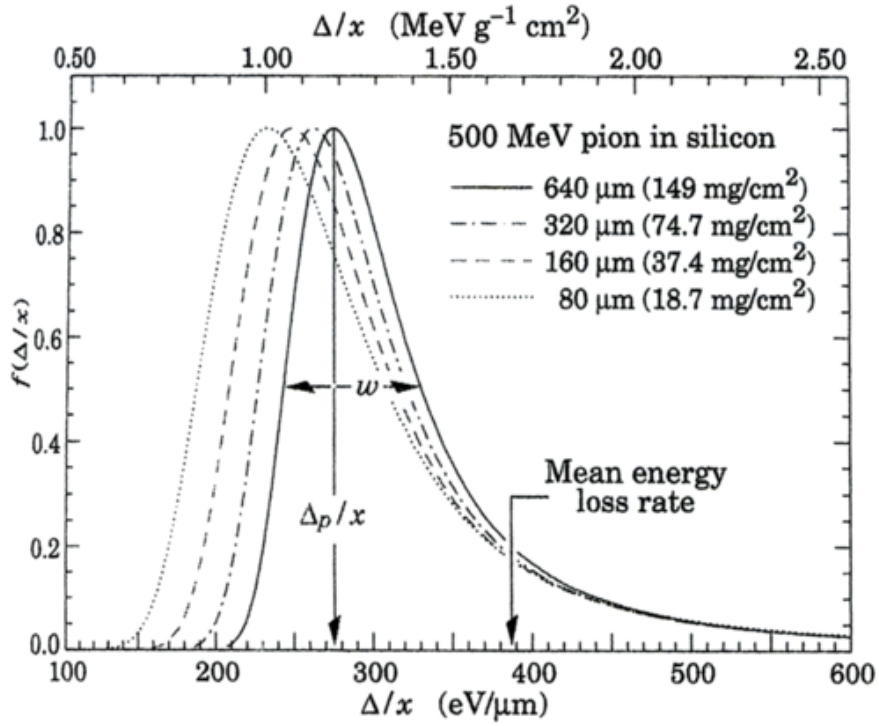

Figure 1.6: *Energy straggling of pions at* 500 *MeV in silicon: the stopping power function, which was first studied by Landau and Vavilov [1], is reported as a function of the energy loss. The* $\Delta p/x$ *is the most probable value, whereas* w *stays for the full width at half maximum. The tail that makes the distribution asymmetric is due to the possibility to have a large energy transfer with a single collision. This latter situation can take place when particles traverse thin layers of matter: in this case the number of collisions is too small for the Central Limit Theorem and so the energy loss distribution can not be Gaussian in form* [7].

Consequently, also the ranges have a statistical distribution around a centered mean range. This fact is called *range straggling*.
Since the interacting particles can undergo some deviations with respect to their initial direction caused by elastic collisions, the Multiple Coulomb Scattering process has to be considered. The angle describing the deviation from the initial direction has an inverse probability with respect to the momentum and velocity of the incoming particle as it is shown in the Multiple Coulomb Scattering equation [1] in eq. (1.8):

$$\theta_0 = \frac{13.6MeV}{\beta cp} z \sqrt{\frac{x}{X_0}} \left[1 + 0.038 \ln \left(\frac{xz^2}{X_0 \beta^2} \right) \right] \tag{1.8}$$

in which θ_0 is the planar angle of scattering and x/X_0 represents the medium thickness of scattering expressed in radiation length. The latter is defined to be the distance over which the electron energy is reduced by a factor $1/e$ because of the radiation loss.

1.1.3 Nuclear fragmentation

The kinds of interaction that can take place when a beam passes through a material are electromagnetic or nuclear with the absorber nuclei. In this latter case the nuclear reactions can be elastic or inelastic. If they are elastic, the charge and the kinetic energy of the involved nuclei are conserved whereas the spatial distribution of the incident particle varies. If instead the collision is inelastic, the nuclei of the target can break releasing secondary particles such as neutrons, protons and heavy ions. Moreover, the incoming particle can undergo fragmentation. One way to describe the secondary particles production is the *abrasion-ablation model* [8]. In this model two relativistic heavy particles interact with each other. They are indicated as the *projectile particle* and *target particle*. The projectile with an initial momentum p collides against the target at rest. The parts of their volumes which overlap are then cut off by the collision and create the hot reaction zone named *fireball*, whereas the other parts that are not overlapping are called *spectator* and they remain on their initial trajectory without changing their velocity. This stage, which is the fast one, is called *abrasion*. Subsequently, the projectile and target nucleus reach the final state when the excited spectators decay with gamma-ray emission and breakdown into nucleons or fragments. This last passage is named *ablation*. In Figure 1.7 an outline of the process is shown.

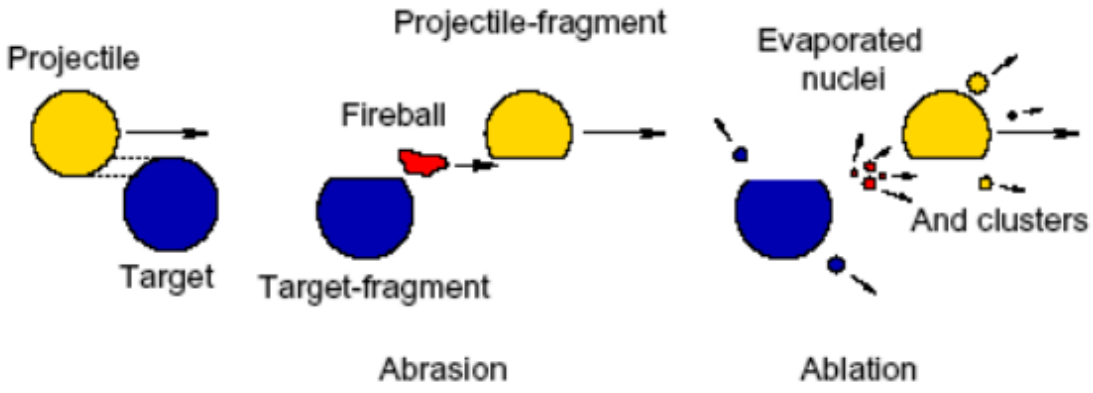

Figure 1.7: *The graph shows the outline of the process with the two stages: the abrasion and the ablation* [9].

Particles coming from the interaction are represented as *projectile fragments* and *target fragments*. The projectile fragments are forward peaked in the laboratory system because the projectile has a high initial velocity. Though broadly speaking it could be said that they maintain the direction and the velocity of the incoming particle, it is not exactly true because the direction and the velocity are not completely conserved. Instead, the fragments coming from the target are released isotropically with a lower velocity and they have an energy of the order of tens of MeV or less [10].

In heavy ions therapy, high energy fragmentation reaction can take place when the beam passes through the biological tissue. Because of these processes the primary beam flux is attenuated and low Z fragments are accumulated as the penetration depth increases. These latter fragments have longer ranges with respect to the primary ions. It is very important to study the fragmentation interactions because these processes can give rise to undesired consequences. In fact the fragments could release their energy outside the treatment volume. For instance, if the particles which originate the fragments are near the beam edge, that is the positions locus at which the particle beam intensity is 10% of the one along the beam axis, the fragments will release their energy outside the volume of interest. Therefore, it can be said that because of the projectile fragmentation a halo around the beam can be created. Another problem is represented, instead, by the production of the target fragments. These kind of fragments are produced isotropically and they can release a localised and very high quantity of energy near the interaction point. Due to the fragments production the depth-dose profiles of beams of heavy ions have a tail after the Bragg peak. As an example in Figure 1.8, the Bragg curves obtained by measurements with monoenergetic beams of ions, are shown. These results were acquired by using three different beams at the NASA Space Radiation Laboratory (NSLR) at the Brookhaven National Laboratory [10]. The beam with the shortest-range is the ^{12}C at 200 MeV/u that can penetrate into the material until it reaches a depth equal to 8.4 cm before stopping. The Bragg curve increases quietly fast with increasing depth of target because the primary ions have a low energy. In this case, the energy loss is dominant. If instead ^{12}C ions at 293 MeV/u are considered, it is found that they travel twice as far than the ^{12}C at 200 MeV/u and their Bragg curve has slower rise and a minor peak. This fact is due to the lower initial stopping power at higher energy and to the fragmentation of the primary beam ions which starts to become important. In the same plot there is also the Bragg curve regarding the ^{16}O at 600 MeV/u. The fragmentation process in now dominant with respect to the ionisation energy loss. In this case the dE/dx is low at the beginning and in a flat portion of the curve. In this way the Bragg peak is deeper in the target, more or less at 37 cm [10].

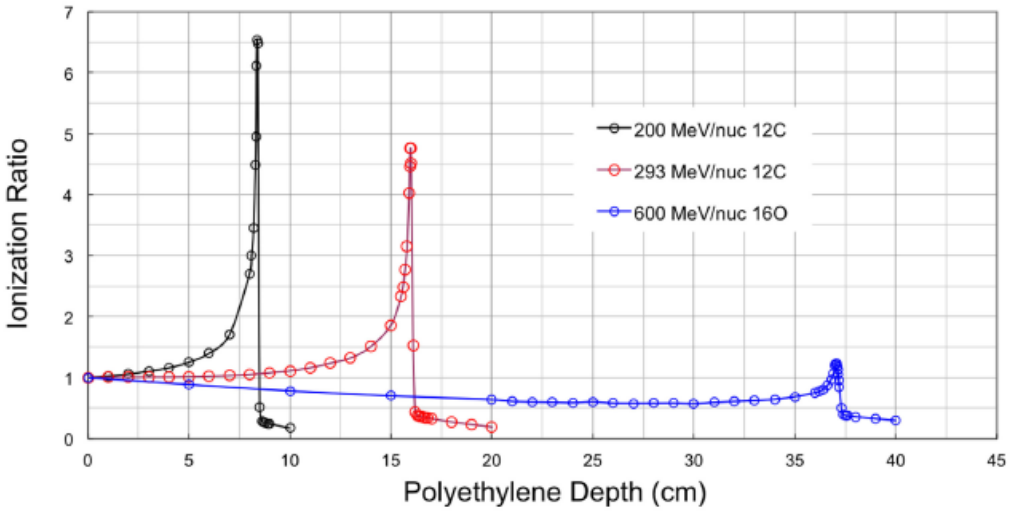

Figure 1.8: *Depth-dose curves for three beams measured at the NASA Space Radiation Laboratory. The beam with the smallest range is the* ^{12}C *with* 200 MeV/u *that penetrates the material until it reaches a depth of* 8.4 cm [10].

In protontherapy the primary beam (i.e., protons) can not fragments due to the low energy range up to 250 MeV [11]. In this way the fragments only come from the target. One way to estimate the average energy of the recoil fragments is the Goldhaber formula [12]:

$$E_f = \frac{3}{5}\frac{p_F^2}{2m_0}\left(\frac{A_t - A_f}{A_t - 1}\right) \tag{1.9}$$

in which A_f and A_t are the fragment and target mass number, m_0 is the proton rest mass and p_F represents the Fermi momentum defined as [12]

$$p_F = 281\left(1 - A_f^{0.568}\right) \tag{1.10}$$

From Eq. (1.9) and Eq. (1.10) it is possible to notice that light fragments will have higher mean energy for a given target material. Furthermore, the mean energy of the fragments is higher for increasing target mass. Moreover, if neutrons are also produced, they will undergo subsequent interactions giving rise to the production of additional secondary particles with high-LET. More details are reported in section 1.5

The fragmentation interactions are also studied to improve the space radiation protection. In this environment there are protons and high-charged particles that can have

nuclear interactions while crossing the spacecraft hull or the internal equipment. If nuclear interactions take place, a lot of secondary particles are produced. Usually, with the shielding it is possible to reduce the risk caused by heavy ions fragmentation. Even if the heavy ions (i.e. $Z > 2$) are only the 1% of the galactic cosmic rays, their contribution varies between 30% and 40% of the total dose because the energy loss is proportional to the square of the charge of the projectile. When the space radiation passes through the spacecraft wall, some neutrons can be produced because of the fragmentation interaction and they can reach the inhabited zones. This topic is discussed more in detail in section 1.6.

In this frame, the main goal of the FOOT (FragmentatiOn Of Target) experiment is to provide nuclear fragmentation cross section data as it is later shown in Chapter 2.

If an initial number of particles N_0 passes through a material with a thickness x, the number of particles that have not interacted is given by the exponential law:

$$N(x) = N_0 exp(-x/\lambda), \tag{1.11}$$

in which λ is the mean free path. The mean free path can be written as:

$$\lambda = \frac{M_{mol}}{N_0 \rho \sigma_r}, \tag{1.12}$$

where σ_r is the total reaction cross section M_{mol} stands for the molecular mass of the material, ρ represents the material density. Even if these processes are not very well known from the theoretical point of view, some measurements of the reaction cross sections have been done and some parametrizations are available, like the Bradt and Peters equation [13]:

$$\sigma_r = \pi r_0^2 \left(A_P^{1/3} + A_T^{1/3} - \delta_0 \right)^2 \tag{1.13}$$

where r_0 and δ_0 are parameters depending on the model, A_P and A_T are respectively the mass number of projectile and target. The cross section is a very important quantity that characterises the nuclear interaction and it is required in Monte Carlo simulations in order to calculate the nuclear interaction probability.

1.2 Photons interaction with matter

X-rays and γ-rays are both electromagnetic radiations but they have a different origin. The γ-rays are produced when an excited nucleus undergoes deexcitation, whereas x-rays are due to electrons that hit a target or when they rearrenge in an atom. Both the x-rays and γ-rays are more penetrating in matter with respect to charged particles because the cross section of their reactions are much smaller with respect to the inelastic electron collision cross section. The second characteristic regarding x-rays and γ-rays is

that a beam of photons is not degraded in energy but only attenuated in intensity when it passes through a layer of matter. This latter feature, instead, is due to the fact that during their interaction with matter, the photons are extracted from the beam because of absorption or scattering. Only photons that have not interacted can proceed and conserve their energy. The total number of photons in the beam is reduced after passing through a slab of matter, and it is described by the following exponential law, called Berr-Lambert law:

$$I(x) = I_0 e^{-\mu x} \tag{1.14}$$

where I_0 is the incident beam intensity, x is the absorber thickness and μ is the absorption coefficient depending on the absorber material and correlated to the total cross section. Photons can interact with matter in three ways:

- **Photoelectric effect**

  In the photoelectric effect a photon is absorbed by an atomic electron which is in turn ejected by the atom. The outgoing electron has an energy equal to

  $$E = h\nu - B.E. \tag{1.15}$$

  where $B.E.$ is the binding energy of the electron. The photoelectric effect can occur only with a bounded electron because in this way the recoil momentum is absorbed by the nucleus, while a free electron can not absorb a photon and conserve the momentum. In Figure 1.9 it is possible to notice that at energies above the highest binding energy of the electrons of the atom, the K shell, the cross section is small but it increases quickly as the K-shell energy is approached. After this point the K absorption edge takes place in which the cross section goes down because the K-electrons are no more available. Below this energy, the cross section grows again and declines as the L and M levels are passed. The latter ones are called *L-absorption* and *M-absorption* respectively.

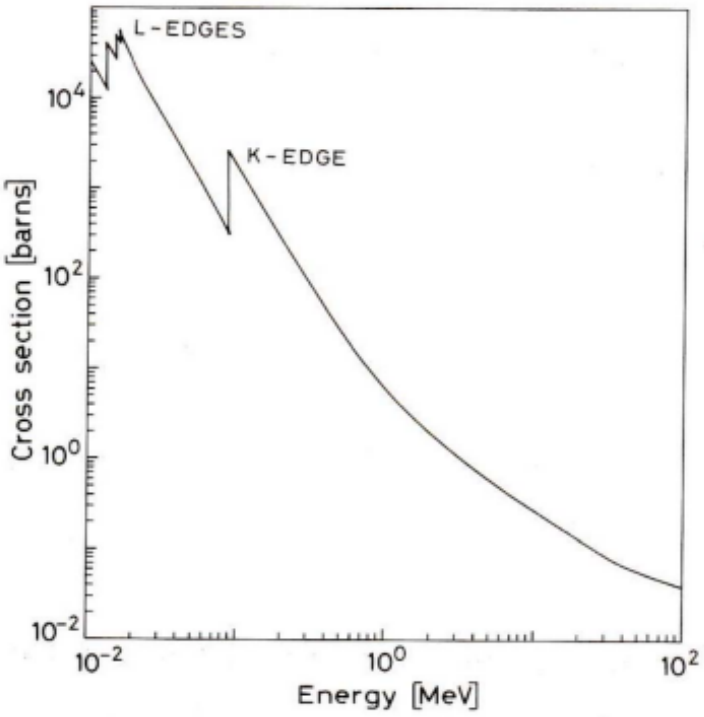

Figure 1.9: *Photoelectric cross section as a function of the energy of the incident photons in lead* [14].

The cross section of the process has a dependence on the photons energy and the atomic number Z of the material. If the incident photons have an energy in the range $0.1 < E_\gamma < 5$ MeV, the cross section has a dependence on Z given by $\sigma \propto Z^n$ where n is found to fluctuate between 4 and 5; otherwise the dependence of the cross section on Z is given by $\sigma \propto Z^5$ [14]. Usually the cross section is proportional to Z^4 at low energy, whereas it depends on Z^5 at high energy [15]. It is evident that the materials with higher Z are the most effective for the photoelectric absorption [14].

- **Compton scattering**

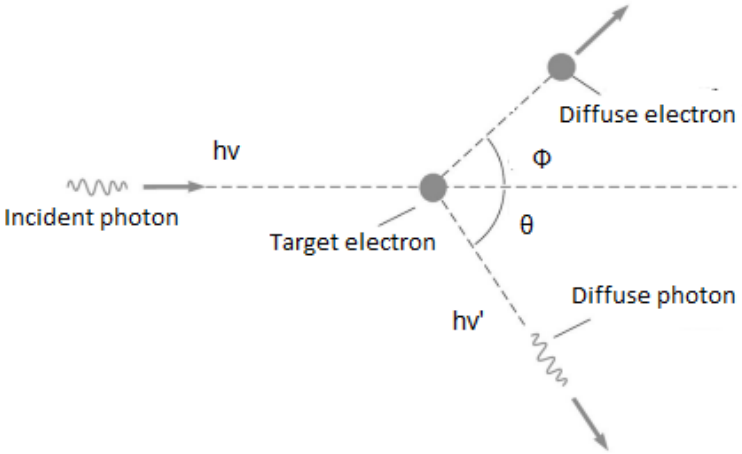

Figure 1.10: *Compton scattering process: $h\nu$ is the energy of the incoming photon, whereas $h\nu'$ stands for the energy of the diffuse photon. θ represents the scattering angle of the photon with respect to the direction of the incoming one, ϕ is instead the scattering angle of the electron with respect to the direction of the incoming photon* [16].

In this process photons scatter on free electrons. Since in matter the electrons are bound, the process can take place if the photon energy is much higher than the binding energy of the atomic electron. In this way, this latter energy can be ignored and the electron can be considered free. By applying energy and momentum conservation, it is possible to obtain the following relation:

$$h\nu' = \frac{h\nu}{1 + \gamma(1 - \cos\theta)} \tag{1.16}$$

$$T = h\nu - h\nu' = h\nu \frac{\gamma(1 - \cos\theta)}{1 + \gamma(1 - \cos\theta)} \tag{1.17}$$

$$\cos\theta = 1 - \frac{2}{(1+\gamma)^2 \tan^2\phi + 1} \tag{1.18}$$

$$\cot\phi = (1+\gamma)\tan(\theta/2) \tag{1.19}$$

where $h\nu$ is the incoming photon energy, $h\nu'$ represents the energy of the diffuse photon, θ stands for the photon scattering angle, ϕ is the electron scattering angle, $\gamma = h\nu/m_e c^2$ and T is the outgoing electron kinetic energy. The scattering angle, θ, can take any value between 0 and π. If it is equal to 0, the forward scattering takes place in which the photon energy does not change whereas the electron kinetic energy is null. If instead it is equal to π, the process is called *backward scattering* which is characterised by the fact that the photon energy is minimum and the electron energy is maximum:

$$h\nu' = \frac{h\nu}{1+2\gamma} \tag{1.20}$$

$$T = h\nu\frac{2\gamma}{1+2\gamma} \tag{1.21}$$

The Figure 1.11 represents the recoil Compton electrons energy distribution.

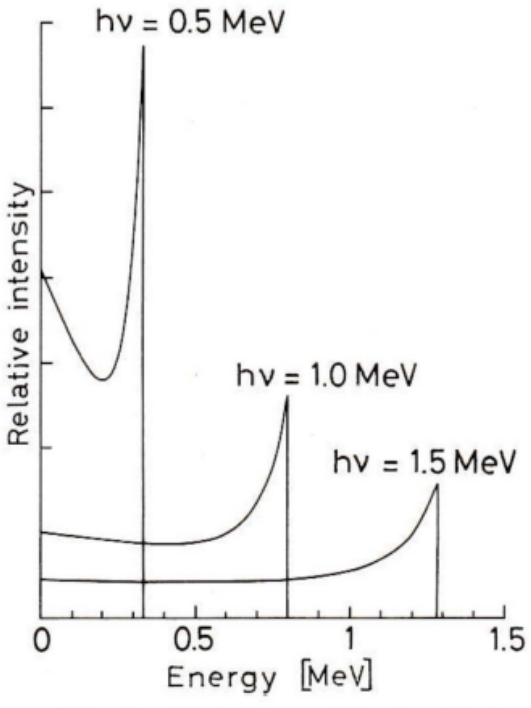

Figure 1.11: *Recoil Compton electrons distribution of energy: the rapid fall down at the maximum recoil energy is known as Compton edge* [14].

The Compton scattering differential cross section is described by the Klein-Nishina formula:

$$\frac{d\sigma}{d\Omega} = \frac{r_e^2}{2} \frac{1}{\left[1+\gamma\left(1-\cos\theta\right)\right]^2} \left(1+\cos\theta^2 + \frac{\gamma^2\left(1-\cos\theta\right)^2}{1+\gamma\left(1-\cos\theta\right)}\right) \tag{1.22}$$

in which r_e represents the classical electron radius. If an integration over $d\Omega$ is applied, it will be found the total cross section, whose behaviour in function of energy is reported in Figure 1.12,

$$\sigma_c = 2\pi r_e^2 \left\{ \frac{1+\gamma}{\gamma^2} \left[\frac{2\left(1+\gamma\right)}{1+2\gamma} - \frac{1}{\gamma}\ln\left(1+2\gamma\right) \right] + \frac{1}{2\gamma}\ln\left(1+2\gamma\right) - \frac{1+3\gamma}{\left(1+2\gamma\right)^2} \right\} \tag{1.23}$$

The cross section depends on the atomic number of the material as $\sigma \propto Z$ [14].

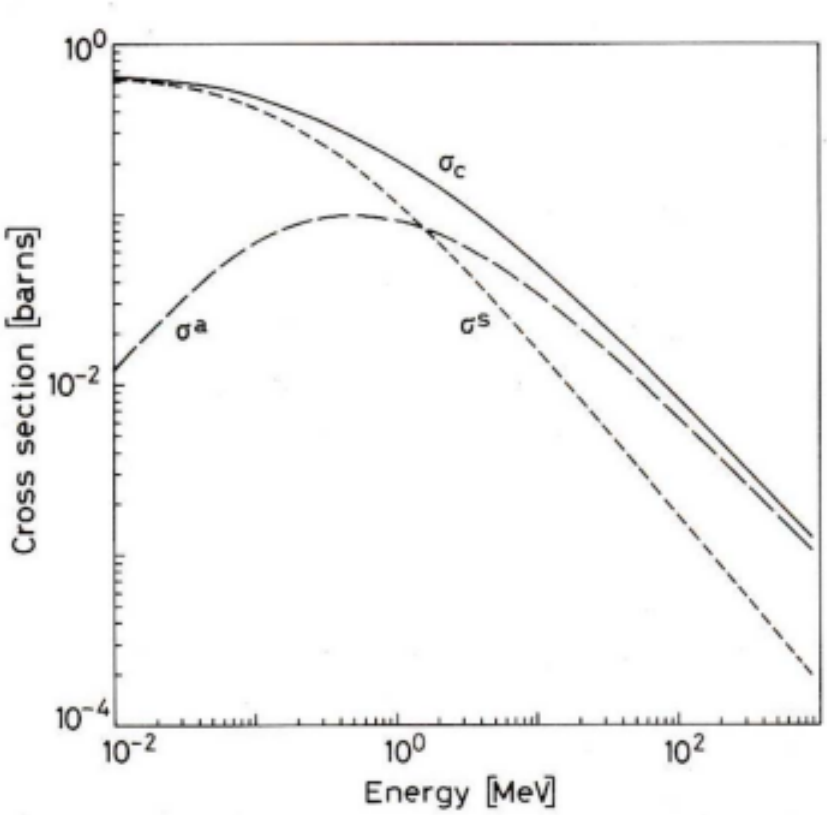

Figure 1.12: *The graph shows the total cross section of the Compton effect* [14].

- **Pair production**

  In this process, a photon is transformed into an electron-positron pair. Since the momentum must be conserved, a third body in the process is required, usually a nucleus. The energy of the photon in order to produce the pair has to be at least 1.022 MeV because it has to exceed twice the electron rest-mass energy. The probability of the process to take place is usually very small below several MeV; the energy in excess is transformed into the kinetic energy of the electron and positron. Successively, the positron tends to annihilate and so two annihilation photons are produced as secondary products. The probability of the pair production has a magnitude which depends on the quadratic of the absorber atomic number, $\sigma \propto Z^2$ [14].

The relative importance of the three types of interaction as function of the absorber atomic number is shown in Figure 1.13. In the graph it is possible to notice that there are three different areas where a process is dominant. Starting from the left the two black curves represent the energies at which the photoelectric effect and the Compton scattering, and the Compton scattering and the pair production, have the same probability to occur, respectively.

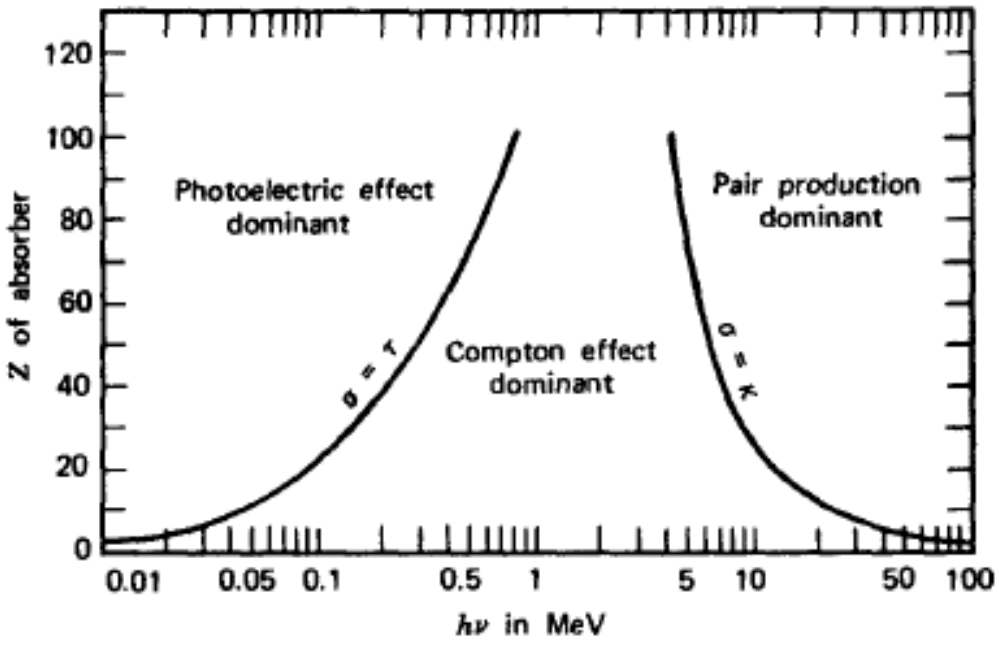

Figure 1.13: *Relative importance of the three kind of interaction of photons with matter. The lines represent the Z value and the energy hν for which the two adjacent processes have the same probability to take place* [17].

1.3 Neutrons interaction with matter

The neutrons have no electric charge and so they can not interact with matter via the Coulomb force. The only case in which they interact it is with the nuclei in matter, either elastically or inelastically. In this latter case, the neutron is replaced by one or more secondary radiation, while in case of elastic scattering it changes its energy or direction. The secondary radiation produced in the interaction can be either gamma rays or charged particles. These charged particles can have two origins: they can come from neutrons-induced nuclear reaction, or they are the recoil nuclei of the absorbing material that have acquired energy from the collisions with neutrons. This last kind of effect is often exploited in neutron detectors.

The relative probabilities regarding the different kind of neutron interactions change with the neutron energy, and the processes that can occur are listed in the following, were the notation $X\,(x,y)\,Y$ means particle x that collides against a nucleus X and a particle y together with a nucleus Y that are produced (if the $*$ symbol is present, it means that the particle or the nucleus is left in an excited state [1])):

- Elastic scattering, $A\,(n,n)\,A$, which is the main interaction for neutrons at the energy range of MeV [1];
- Inelastic scattering, $A\,(n,n')\,A^*$ or $A\,(n,2n')\,B$, in which the nucleus is excited, and can have a gamma decays to its ground state. In this kind of reaction, the neutron must have enough energy in order to excite the nucleus whereby this type of process can happen at an energy scale of 1 MeV or more;
- Radiative neutron capture, $A\,(n,g)$, whose cross section is inversely proportional to the neutron velocity [1]. Therefore the radiative capture is more probable at low energy;
- Other nuclear reactions, for example (n,p), (n,d), (n,α), where the neutron is captured and charged particles are emitted. Similarly to the radiative neutron capture, the cross section depends on the inverse of the velocity, $1/v$;
- Fission, which occurs at thermal energies and/or above to some MeV;
- High energy hadron shower which can happen at very high energy, $E > 100$ MeV.

Since neutron interactions have a strong energy dependence, neutrons are classified according to their energy; so if the neutrons have more than 100 MeV they are *high energy neutrons*, whereas the *fast neutrons* are the ones with an energy within the range of a few hundred of keV to few tens of MeV. If instead the range is between 0.1 eV and 100 keV the neutrons are called *epithermal*. In the latter case, when the energy is similar to the thermal agitation energy at the room temperature, ($E = 0.0253$ eV), the neutrons

are known to be *thermal* or *slow*. If the energy is even lower, such as milli- or micro-eV, the neutrons are named *cold* or *ultra-cold*. To find the probability of neutron interaction in matter it is necessary to sum the cross sections of each possible process:

$$\sigma_{tot} = \sigma_{elastic} + \sigma_{inelastic} + \sigma_{capture} + ... \tag{1.24}$$

If the eq. (1.24) is multiplied by the atoms density, the mean free path length, λ, of the neutrons results to be:

$$\frac{1}{\lambda} = N\sigma_{tot} = \frac{N_a \rho}{A}\sigma_{tot} \tag{1.25}$$

where A is the mass number and N_a is the Avogadro's number. As in the photons case, a neutrons beam that crosses a piece of matter is attenuated by the exponential law:

$$N = N_0 \exp\left(-x/\lambda\right) \tag{1.26}$$

in which x is the material thickness. Usually, they have a large depth in matter because, as it was said at the beginning of this paragraph, they do not easily interact with matter. Normally, if the neutrons energy is low ($E_n <$ eV) the mean free path is under a centimeter, whereas for high energy neutrons ($E_n >$ 100 KeV) the mean free path is more than 10 centimeters [6]. Consequently, in order to detect a neutron, it has to lose its energy so it can interact and produce charged particles that can be detected. Basically, neutrons are slowed down in order to be captured. The process thanks to which the fast neutrons are slowed down is the moderation [1]. When a neutron enters into a material, it undergoes some elastic and inelastic scattering back and forth on the nuclei. In this way it loses some energy until it reach the thermal equilibrium with the material atoms. Then it will diffuse until a nucleus captures it or another reaction, such as fission, takes place. The main process thanks to which the fast neutrons lose their energy is the elastic scattering shown in Figure 1.14.

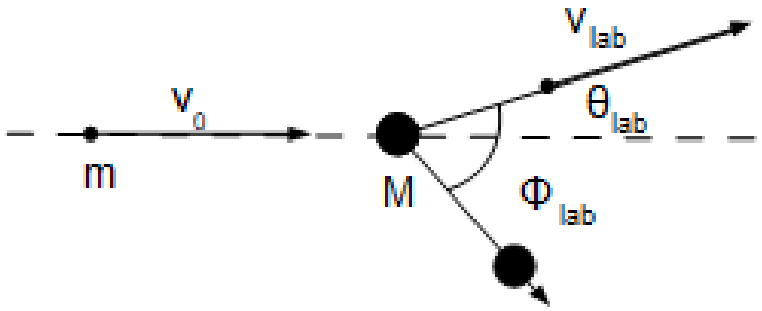

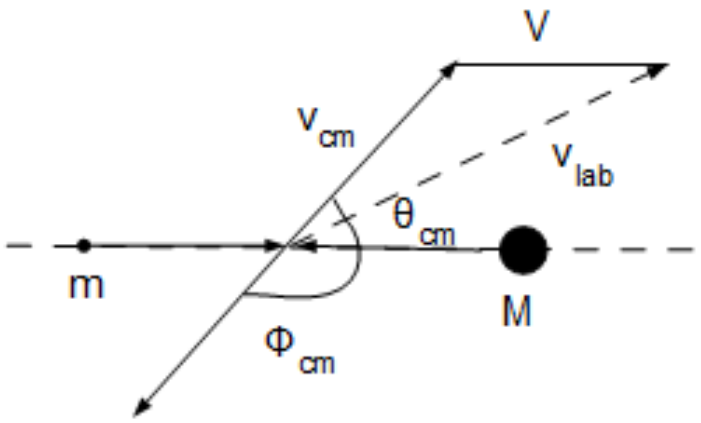

Figure 1.14: *Elastic collision of a neutron on a nucleus with mass M. In the top panel, the scattering is shown in the laboratory system, whereas in the bottom illustration the collision is made in the center of mass system.*

If the calculation are made in units of the neutron mass, $m_n = 1$, and the nucleus mass is just the atomic mass number A. A transformation into the center of mass system is applied and it is derived that the velocity of the neutrons is given by [1]:

$$v_{cm} = \frac{A}{A+1} v_0 \tag{1.27}$$

whereas the nucleus velocity is:

$$V = \frac{1}{A+1} v_0 \tag{1.28}$$

The neutron velocity in the laboratory system is connected to the one in the center of mass system thanks to relation

$$(v_{lab})^2 = (v_{cm})^2 + V^2 - 2 v_{cm} V \cos(\pi - \theta_{cm}) \tag{1.29}$$

in which θ_{cm} is the center of mass scattering angle. When in the Eq.(1.29), the Eq.(1.27) and (1.28) are reported, it is possible to obtain:

$$(v_{lab})^2 = \left(\frac{A}{A+1}\right)^2 v_0^2 + \left(\frac{1}{A+1}\right)^2 v_0^2 - 2\frac{A}{(A+1)^2} v_0^2 \cos(\pi - \theta_{cm}) \tag{1.30}$$

If the kinetic energy is considered, which is equal to $E = \frac{1}{2} m v^2$:

$$\frac{E}{E_0} = \left(\frac{v_{lab}}{v_0}\right)^2 = \frac{A^2 + 1 + 2A\cos\theta_{cm}}{(A+1)^2} \tag{1.31}$$

The laboratory angle is instead retrieved from the following relation as:

$$(v_{cm})^2 = (v_{lab})^2 + V^2 - 2v_{lab}\cos\theta_{lab} \tag{1.32}$$

$$\cos\theta_{lab} = \frac{A\cos\theta_{cm} + 1}{\sqrt{A^2 + 1 + 2A\cos\theta_{cm}}}. \tag{1.33}$$

The recoil nucleus has the following scattering parameters:

$$E_A = E_0 \frac{4A}{(A+1)^2}\cos^2\phi_{lab} = E_0 \frac{2A}{(A+1)^2}(1 + \cos\phi_{cm}) \tag{1.34}$$

$$\cos\phi_{lab} = \sqrt{\frac{1+\cos\phi_{cm}}{2}}. \tag{1.35}$$

If the eq.(1.31) is taken into account it is possible to notice that the energy of the scattered neutron is included in the range:

$$\left(\frac{A-1}{A+1}\right)^2 E_0 < E < E_0 \tag{1.36}$$

where the extremes represent the scattering when the $\cos\theta_{cm}$ is respectively equal to $+1$ and -1. If the scattering is made onto a proton, which has $A = 1$, the result is:

$$0 < E < E_0 \tag{1.37}$$

Evidently, a lighter nucleus absorbs more recoil energy from the neutron with respect to a heavier one. Therefore, the best moderator results to be the hydrogen because if a neutron collides against a hydrogen nucleus, the neutron will loose up to all its energy in a single collision [17]. For this reason, materials with a high hydrogen concentration are the preferred ones for the radiation protection in space. The lightweight polyethylene plastic, named RFX1, that is made of lightweight carbon and hydrogen [18], and the Kevlar [19], which is an aramid fiber [20], are some of the materials used in order to shield radiation since they can reduce the dose rate of $32 \pm 2\%$ and they can reduce the dose equivalent rate of $55 \pm 4\%$ for a shield of 10 g/cm^2 [19]. This topic will be covered with more details in section 1.6. Another consequence of the fact that the hydrogen is the best moderator is related to neutron detection. In fact, in order to detect higher energy neutrons it is necessary to detect the recoil protons of the elastic scattering process. For this reason materials containing a large number of hydrogen atoms, such as plastic or organic compounds, are the most widely used. In the present thesis work, the liquid scintillator BC-501A was used in order to detect the fast neutrons and to discriminate them from γ-rays, which are usually emitted in neutron reactions, thanks to the *pulse shape discrimination*. The characteristic of the BC-501A and the pulse shape discrimination will be treated more in detail in section 2.3.1 and 3.3, respectively.

1.4 Biological effects of radiation

Genetic information is carried into the cells by two macromolecules of nucleic acids: *deoxiribonucleic acid* (DNA) and *ribonucleic acid* (RNA). The DNA archives instructions in order to synthesise proteins, whereas RNA molecules translate and transcribe the DNA information for the mechanics of protein synthesis. The nucleic acids are composed by nucleotides whose hydrolysis gives rise to a heterocyclic amino base, to a monosaccharides with five carbon atoms and a phosphate ion. In the case of DNA the monosaccharides is the $2-\text{deoxy}-\text{D}-\text{ribose}$ and it is in the center of the nucleotide with the phosphate group bound to the monosaccharides as phosphate ester in C5' or in C3'. Instead the nitrogen base is bound to the deoxyribose thanks to a β type $\text{N}-$glycosidic bond. The amino bases are divided into *purines*,

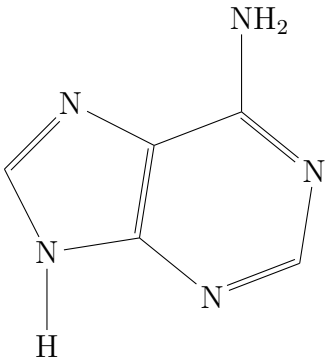

adenine (A)

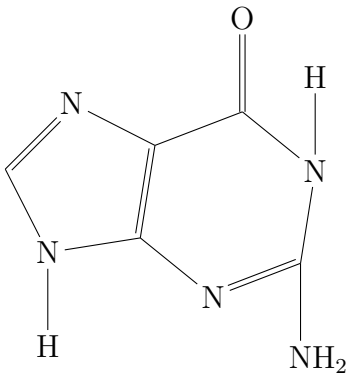

guanine (G),

and into *pyrimidines*.

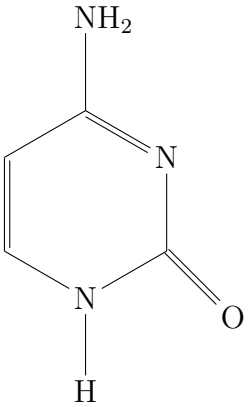

cytosine (C)

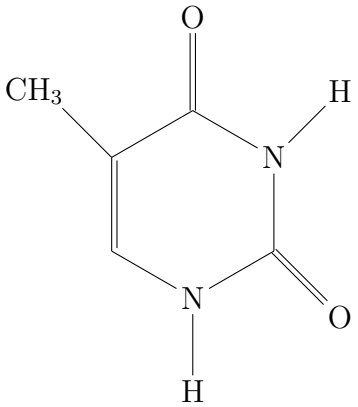

thymine (T).

Finally, the deoxiribonucleic acid has a double helix structure with two molecular filaments bonded with hydrogen bonds that is represented in Figure 1.15. In particular, there are three hydrogen bonds between cytosine and guanine, whereas adenine and thymine are bonded with two hydrogen bonds.

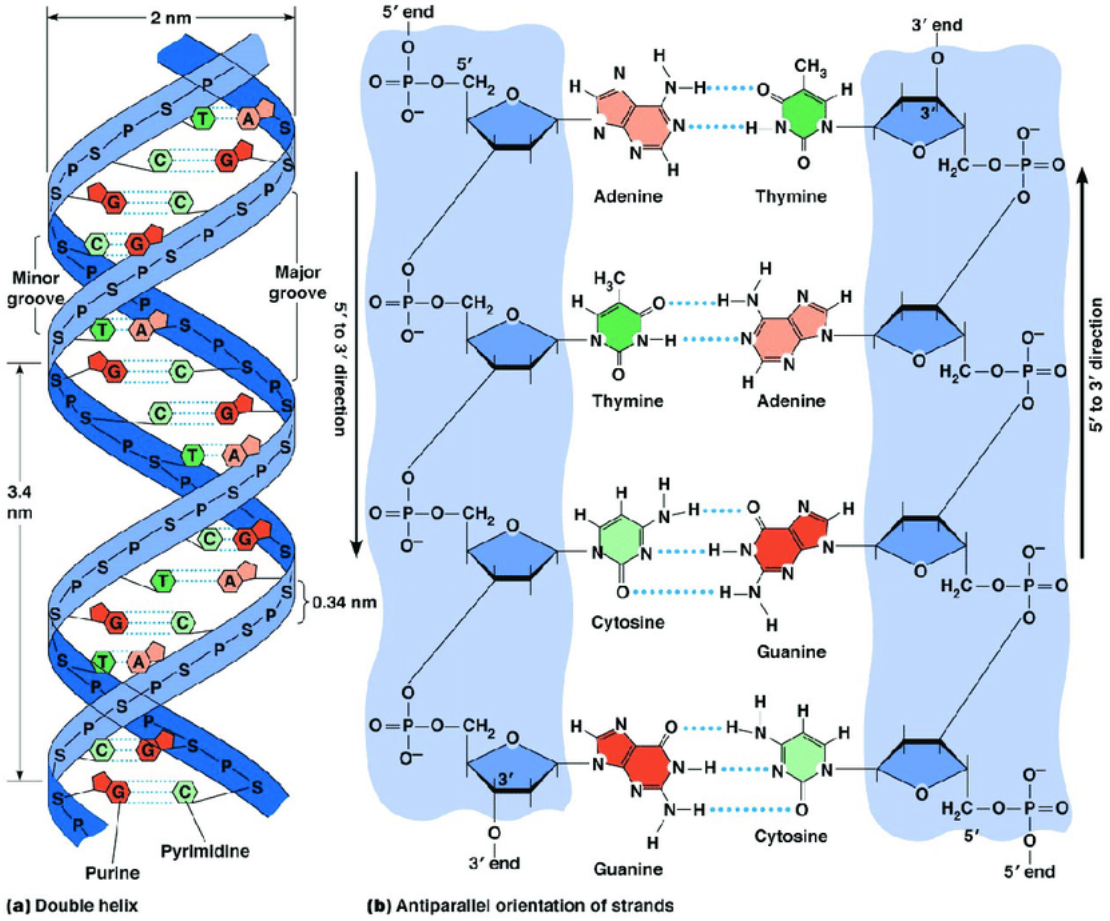

Figure 1.15: *Double helix structure of the DNA* [21].

It is thanks to the sequence of the basis that the information to synthesise proteins is transported [22]. Because of the radiation the DNA can undergo some damages which are the *Single Strand Break* and the *Double Strand Break*. The Single Strand Break can be repaired because the strand that has been damaged can be reconstructed by copying the right sequence from the other strain. If instead a Double Strand Break takes place, it can be repaired if the damages are in different parts of the strand, whereas the damage is irreparable if both the strands of the DNA are broken.

Since the radiations can cause biological damages, in order to quantify the radiation received by a body, different units are used. The oldest one is the *Röntgen* that measures the exposure and it is defined as the quantity of x-rays which produce an ionisation of $2.58 \cdot 10^{-4}$ C/Kg in air. As it expresses the ability to ionise air and create charges, it is mainly used for X-rays and γ-rays [1]. More relevant quantities are the *dose*, the *equivalent dose* and the *effective dose*. The dose represents the total energy absorbed

per unit mass and it is measured in *Gray* (Gy):

$$D = \frac{dE}{dm} \tag{1.38}$$

Usually, the standard hadrontherapy treatment consists in the administration of 1 - 2 Gy on the tumor volume for each fraction for a total of 30 - 35 fractions [11]. However, this unit does not consider the biological effects unlike the equivalent dose, measured in *Sievert* (Sv), that is defined as:

$$D_{eq} = \sum_R w_R D \tag{1.39}$$

It is expressed as the sum on all possible radiation, each of which has its own dangerousness weight or quality factor. The latter is given by the ratio between the biological damage produced by 1 Gy absorption of that radiation and the biological damage caused by 1 Gy of γ-ray. In this way the effect due to 1 Sv of any radiation is the same due to 1 Gy of γ-ray. The dose of 1 Sv always gives the same damage regardless of radiation. In the effective dose, instead, the biological effects caused by the radiation type are considered together with the nature of the target tissues. It is also measured in Sievert and it is defined as follows:

$$D_{eff} = \sum_T w_T D_{eq} = \sum_T w_T \sum_R w_R D \tag{1.40}$$

in which w_T is the tissue weight and D_{eq} is the equivalent dose absorbed by the tissue. If a tissue is very sensitive, like the ones having great cell reproduction, the radiation can destroy the cancer very easily. If instead the tissue is a resistant one, as the one with low cellular reproduction, it is not easy to destroy cancer with radiation.

Another important concept, that has to be introduced, is the *linear energy transfer*, LET, which is defined as the energy transferred per unit of distance, from the ionising particle to the material and it is measured in KeV/μm or in MeV/cm. It is similar to the stopping power. In fact, in the stopping power the focus is on the particle, whereas in the LET the focus is on the material that surrounds the particle because what matters is the energy transferred near the track of the particle with the exclusion of the secondary high energy electrons that have a long range. In formula:

$$L.E.T. = -\frac{dE}{dx} \tag{1.41}$$

in which the dE is the energy lost by the radiation and the dx is the track length. The LET depends on the velocity and on the charge of the ionising particles. The ionizing partciles can be classified into those with *high LET* and those with *low LET*. The ones with low LET release less energy per unit path length and therefore the ionizing events are isolated and less frequent. In this way the time it takes to them to lose all their

energy is greater. On the contrary, the ionizing particles with high LET release a high amount of energy per unit of path length and therefore they have more probability to cause damages to the DNA thanks to double strand break events. These latter ones are more efficient at giving rise to localised DNA damages that are difficult to repair. The double strand break can be repaired if the injuries are in different strand regions whereas it cannot be repaired if the injury is in the same strand region.

To find out the number of surviving cells (S) at a certain dose (D), the linear quadratic model is used and it is given by:

$$S = e^{-\alpha D - \beta D^2} \tag{1.42}$$

In this formula, the αD term represents the unrepairable damages whereas the term βD^2 performs the repairable damages because it takes into account the fact that a lot of chromosomal aberrations are caused by double strain breaks and that there are cell recovery processes. The α and β terms depend on the tissue; they are respectively measured in $[\text{Gy}]^{-1}$ and $[\text{Gy}]^{-2}$ and they correspond to the *lethal cell damage* and to the *sublethal cell damage* (it is below the lethal threshold). In the above formula the part proportional to the dose represents the double strain break whereas the part proportional to the square of the dose corresponds to the single strain break, therefore if a radiation has a high energy transferred per unit of distance the double strain breaks are more probable from one track and the survival curve can be described only by the single exponential $Ae^{-\alpha D}$. In this latter case the survival curve is described as

$$S = e^{-\alpha D} = e^{-\frac{D}{D_0}} \tag{1.43}$$

It is useful to define the dose needed to reduce the cell survival to 10% :

$$\begin{aligned} ln(S) &= -\frac{D}{D_0} \\ D_{10} &= -D_0 \cdot ln(0.1) = 2.3 D_0 \end{aligned} \tag{1.44}$$

Two other important quantities are

$$\begin{aligned} D_{37} &= D_0 \\ D_{50} &= 0.69 D_0 \end{aligned} \tag{1.45}$$

which represent, respectively, the doses needed to reduce the cell survival to 37% and to 50%. An important value, that depends on the tissue, is given by $\frac{\alpha}{\beta}$. It gives the dose amount at which the linear and the quadratic parts cause the same effect. Thanks to this parameter, the tissues can be classified into two different ranges:

- if $0.5 < \frac{\alpha}{\beta} < 6$ Gy, the tissues are *late responders*, they have a low reproduction activity and they are more resistant to the radiation. Examples are the spinal cord, the lung, the bone and the cartilage.

- if $7 < \frac{\alpha}{\beta} < 20$ Gy, the tissues are *early responders*, they have a high reproduction activity and they are less resistant to the radiation. Many cancers fall into this category. Examples are the mucosa and the skin.

In Figure 1.16 the cell survival curve is shown.

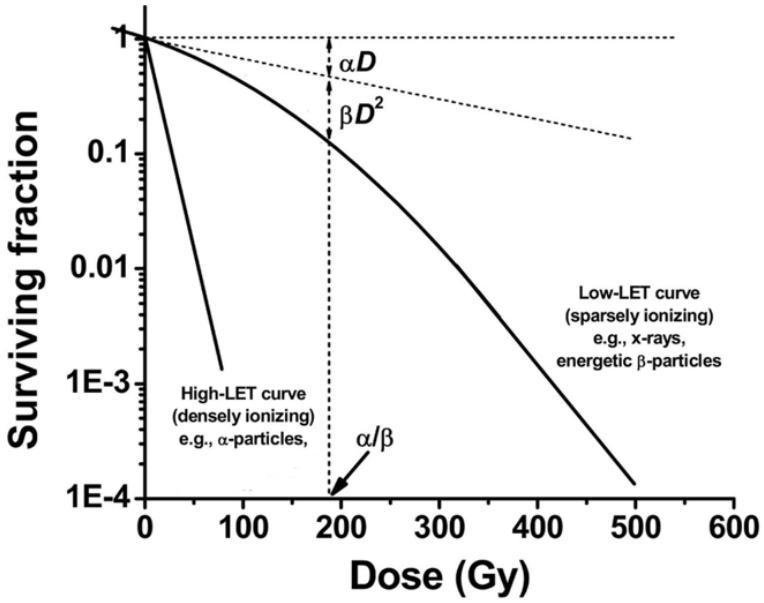

Figure 1.16: *Mammalian cells are shown after a high and a low LET radiation. If the particles are densely ionizing, the logarithmic response is linear whereas if the particles are not densely ionizing the logarithmic response is linear quadratic* [23].

Since the response of the cell to the radiation depends on the kind of the radiation, radiations with different LET but equal dose can give rise to non-identical biological responses. In order to quantify this effect the *relative biological effectiveness*, (RBE), is introduced. It is defined as the ratio between the dose provided by γ-ray and the one provided by hadrons in order to obtain the same effect as shown in the following equation:

$$R.B.E. = \left(\frac{D_{X-ray}}{D_H}\right)_{same\ effect} \tag{1.46}$$

Protons have a RBE roughly equal to 1.1 which is similar to the gamma's one, whereas heavy ions have the RBE greater than one and this means that the hadrons are more effective than gamma rays, in fact the hadrontherapy has an effect three or four times better than that of radiotherapy. The RBE depends on several factors:

- radiation type;

- radiation energy;
- linear energy transfer;
- cell type;
- survival definition.

It is also in function of the LET, as it is shown in Figure 1.17.

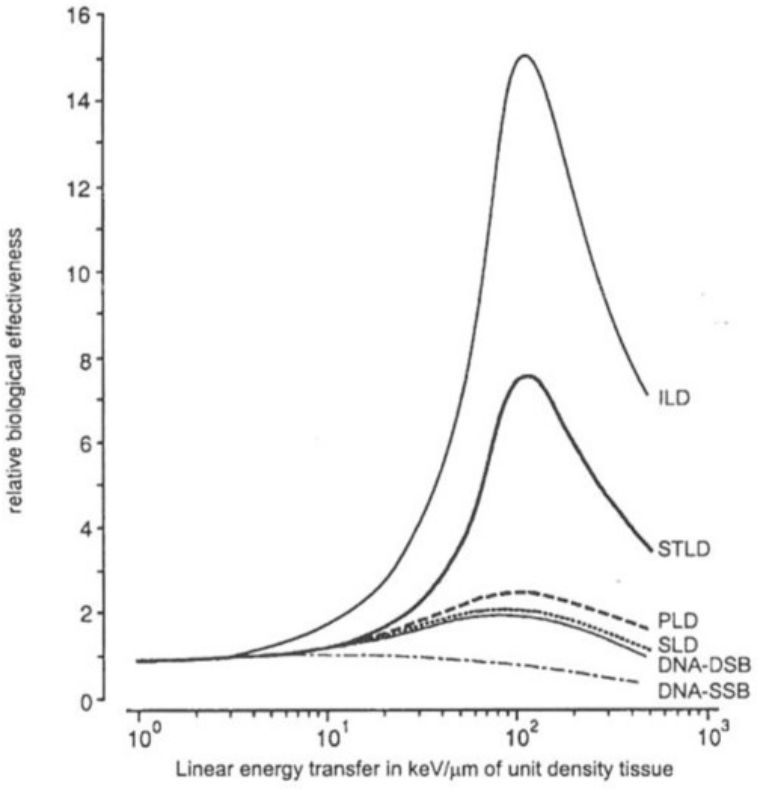

Figure 1.17: *RBE as a function of the LET for several kind of lethal damages in the mammalian cells and also for DNA damage. ILD is the irrepairable lethal damage; PLD stands for potentially lethal damage; STLD represents the single track lethal damage; SLD illustrates the sublethal damage. The DNA-DSB is the double strand break in DNA, whereas DNA-SSB stands for the single strand breaks in DNA* [24].

The RBE increases with the LET up to a maximum after which the RBE decreases due to a saturation effect that starts because too much energy is deposited and therefore it is wasted.

The oxygen concentration can also affect the biological effects. Depending on the concentration, there are three possible cases: *anoxia*, when there is no oxygen, *normal concentration* of oxygen and *hyperoxia* if there is an abnormal presence of oxygen. The *oxygen enhancement ratio* is used to quantify this effect and it is defined as the ratio of the radiation dose necessary to produce a given biological response in the anoxia or normal or hyperoxia state to the dose required to achieve the same response in the presence of oxygen.

$$O.E.R. = \left(\frac{D_{anox,norm,hyper}}{D_{normal}} \right)_{same\ effect} \tag{1.47}$$

By definition the OER is equal to one in normal condition, whereas it is different in case of anoxia and hyperoxia. In case of anoxia the ratio is greater than one which means that it is needed more dose in order to have the same effect, whereas in case of hyperoxia the OER is less than one and less dose is needed for the same effect. The oxygen concentration is important because the oxygen presence amplifies the free radicals action [11]. The molecule of oxygen itself is a biradical species because each of the two atoms has an unpaired electron. In this way the oxygen can accept electrons. If it accepts one electron, it becomes a radical anion, $O_2{}^-\cdot$, called *superoxyde*. The superoxyde has both positive and negative apsects because it is used against pathogens by the immune system but it also takes part to the degenerative processes such as aging and oxidative damage to vital cells. The level of the superoxyde is regulated by the superoxyde dismutase enzime that catalyzes the conversion of the superoxyde into hydrogen peroxide and molecular oxygen. However, the hydrogen peroxide is dangerous because it can produce hydroxyl radicals OH·. The catalase enzime prevents the release of hydroxyl radicals because it converts the hydrogen peroxide into water and oxygen as it can be seen in the next reactions [22]:

$$2\,O_2{}^- + 2\,H^+ \xrightarrow{\text{superoxide dismutase}} H_2O_2 + O_2$$

$$2\,H_2O_2{}^+ \xrightarrow{\text{catalysis}} 2\,H_2O + O_2$$

However, the radiation can increase the concentration of free radicals OH· and H· and of ions H^+ and e^-. The free radicals are very reactive neutral molecules or atoms with an unpaired electron in the last orbital. These particles can give rise to the following reaction mechanisms:

$$O_2 + H\cdot \rightarrow HO_2\cdot$$

$$HO_2\cdot + H\cdot \rightarrow H_2O_2$$

and

$$O_2 + e^- \rightarrow O_2{}^-$$

$$2\,O_2{}^- + 2\,H^+ \rightarrow H_2O_2 + O_2{}^-$$

In the products the hydrogen peroxide is always present and it causes damages to the cells. Therefore, a bigger effect is expected in presence of oxygen, namely, if OER is greater than one. Another aspect to take into account is the LET. If the LET regime is low (< 10 KeV/μm), the probability to produce the hydrogen peroxide is increased by the presence of the oxygen and so the indirect damage to the cells also increases. In this case the OER is equal to 3, which means that the cells treated with normal oxygen concentration are three times more sensitive with respect to the ones treated in anoxia conditions. When the LET is low, the radiolysis events are isolated and the following chemical reaction is favoured:

$$OH\cdot + H\cdot \rightarrow H_2O$$

The formation of only one water molecule in the products does not contribute to the cell damage. If instead the LET regime is high (> 10 KeV/μm), the OER is equal to 1 and there is a saturation effect because the concentration of the hydrogen peroxide, produced by water radiolysis, is already very high and therefore the oxygen presence does not increase the production of the H_2O_2. When the LET is high, the radiolysis events are more frequent and the favoured reaction is the following, in which the hydrogen peroxide is produced:

$$OH\cdot + OH\cdot \rightarrow H_2O_2$$

1.5 Hadrontherapy

The first scientist to propose the use of particle beams to treat tumors was Robert R. Wilson during the second half of the last century [25]. In 1946, Wilson found that thanks to the 150 MeV cyclotron it was possible to produce high-energy protons for particle therapy. In fact, he discovered that the Bragg peak of proton beams in a medium could be employed for radiation therapy. The first studies regarding the particle beams therapeutic application were performed at the Berkeley Radiation Laboratory by John Lawrence and Cornelius A. Tobias, whereas the first clinical studies regarding the application of helium-ion therapy for malignant cancers started in 1976. In the same period the first treatments were performed at the Bevalac facility in which the patients were treated with neon-ion beams accelerated at 670 MeV/u. Subsequently, in 1994, at the National Institute of Radiological Science (NIRS) in Chiba (Japan), new studies regarding treatments with carbon ions started. Nowadays, the radiotherapy made with protons and carbon ions has been analysed for several kind of cancers such as head tumors, lung cancer and their metastasis, gastrointestinal malignancies and also pediatric tumors. The advantage of the use of the ions in radiotherapy is given by their depth-dose profile. In fact, for

X-rays and in photon beams the dose has a sharply exponential decrease with depth, whereas the charged particle beams have a plateau at the entrance region and they reach a peak, the Bragg peak, at the end of their range. In this way, the energy released in healthy tissues around the treatment volume is low whereas most of energy is deposited inside the target volume. However, if a beam of carbon ions is used, there will be some distal energy deposition due to carbon fragmentation as explained in paragraph 1.1.3.

Since the depth in tissue to be reached is not always the same, it is possible to regulate the position of the Bragg peak by varying the kinetic energy of the incident particles. Usually, more beams at different energies are used during a treatment because if only one beam is employed, the Bragg peak produced is too strait to irradiate the entire cancer volume. In this case the Bragg peak created is named *Spread Out Bragg Peak* and an example of it is shown in Figure 1.18

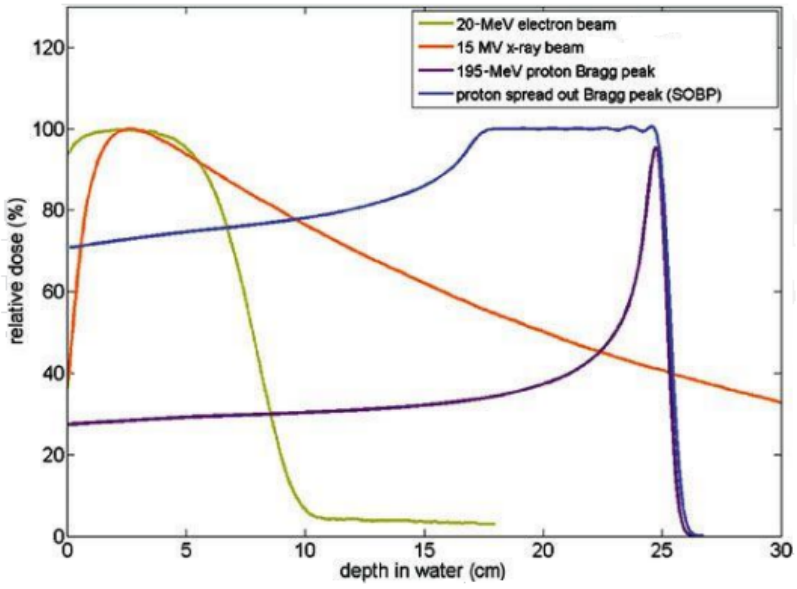

Figure 1.18: *Depth-dose curves for X-rays, electron and proton beam. For the proton beam is shown the Bragg peak and also the Spread Out Bragg Peak* [26].

The Spread Out Bragg Peak can be obtained in two ways: *passive modulation* and *active modulation*. In the former some passive layers are interposed to the beam in order to adapt the beam energy distribution, in the latter the energy is varied during the treatment session. This last method provides a more precise dose distribution reducing secondary particles and neutrons formation inside passive layers which can give rise to radioinduced secondary cancer. Since the dose deposition of the charged particles is really spatially accurate, this kind of treatments are more sensible to uncertainties in beam range than photon treatments. If the range is not well evaluated, the position of

the Bragg peak will be shifted arousing an under-dosage in the treatment volume and an over-dosage in the healthy tissues preceding and following the tumor volume. Typically, the errors are caused by patient motion, such as breathing, anatomical changes, as weight loss or cancer regression, and so on.

Since the LET and RBE, defined in section 1.4, are very high, the treatment with charged particle beams is used with radioresistant cancers. In addition, with the increasing of the particle mass and charge the lateral scattering decreases and so the lateral profile of the beam is narrower allowing to have less damages in the healthy tissues which are beside the cancer. This may suggest that it should be better to use ions with the highest possible atomic number because in this way the LET and the peak-to-plateau ratio is maximum whereas the lateral extension is minimum. However, there is a disadvantage given by the dose tail after the Bragg peak caused by the nuclear interactions, explained in section 1.1.3, which grows up with the charge of the primary particle. This phenomenon causes a worse fall-off in the profile of the dose. Because of this nuclear interactions the LET profile can be modified due to fragments that have different ranges and angular distributions. It is necessary to know very well these processes in order to estimate the fragments contribution in a treatment and improve the irradiation of protons and heavy ions. In the therapeutic energy range, however, the fragmentation processes have not been completely studied by experimental measurements and so the fragments spectra are estimated only thanks to Monte Carlo simulations which have many uncertainties due to the fact that no calculable model is applicable to describe these events.

Another aspect connected to the fragmentation is the neutrons production from the tissues which are hit by hadrons. If a lot of them are produced during the fragmentation, they might cause secondary cancers. From the study carried out by M. Anwar Chaudry, [27], it is shown that more than 4.2 neutrons with energies bigger than 5 MeV are produced for each incident carbon ion of 400 MeV/u during treatment. If the incident energy of C-ions is smaller, the number of neutrons produced will be lower. The lesser production of neutrons also occurs when protons are used instead of carbon ions because in this last case it must be considered that more protons are necessary in order to release the same dose as C-ions of similar energy. These secondary neutrons result to have a real potential to give rise to new cancers. However, since there are not a lot of studies regarding the production of secondary neutrons at relevant energies to hadrontherapy, also the FOOT experiment is being upgraded in order to evaluate their production in conjunction with the charged fragments. In this way it is possible to put more constraints on the Monte Carlo nuclear production models which are used for particle therapy and radioprotection in space.

1.6 Radiation protection in space

During a space mission, the astronauts can be subjected to risks coming from the extravehicular activities (EVA). Thanks to the magnetosphere the Earth is protected by the radiation coming from the space and from the sun, whereas the astronauts are exposed to the galactic cosmic rays (GCR) and to the solar particle events (SPE). The GCR are composed by low levels of heavy charged particles, usually nuclei, which come from outside the solar system but inside the Milky Way galaxy. The galactic cosmic rays pervade the interplanetary space and they are composed of 85% hydrogen, 14% helium and 1% high-energy and highly charged particles (HZE) like carbon, iron or nickel nuclei with a high atomic number and high kinetic energy. The SPE, instead, are made of fluctuating levels of high energy protons together with x-rays, gamma-rays and electrons produced during solar flares and coronal mass ejection (CME). Both these types of radiation, GCR and SPE, can cause damages to the shielding materials and to the biological systems. Even if the dose due to space radiation is low, the effects are cumulative and since the solar activity is not stable, the risks increase as time spent in space grows. That's why space radiation is the main landmark for long-term missions. Some space radiations can pass through the spacecraft material altering it and giving rise to secondary particles which can increase the damages. Usually the GCR can ionize the matter through which they pass and they cross the spacecraft material or the astronauts skin unconstrained. They are the most difficult to shield and the dominant radiation source.

In order to reduce the effects of radiations, the exposition of the astronauts is limited, so they can stay at the Space Station for $3 - 6$ months. If missions of long duration are taken into account, such as exploration to the Moon or a round-trip to Mars [18], other precautions have to be taken involving a better shielding and mitigating strategies. For what concern the shielding, the radiation shielding requirements are different depending on the kinds and level of radiation. The gamma-rays and the GCR are the most penetrating ionizing radiations that can cross also aluminium. They can be stopped by materials with high density and thickness such as cement. However, it has to be considered that these materials must be lifted into orbit, so, it is necessary to minimize the weight. For this reason, if the International Space Station is taken as an example, most of its outer shell is made of aluminium [28]. Other shielding materials used on the space station are hydrogen-rich substances or polyethylene. These latter kind of materials have reduced the exposition of the crew to the space radiation. Researchers have so found that materials with a high hydrogen concentration such as polyethylene can shield 50% better from solar flares and it can shield 15% better against the galactic cosmic rays with respect to aluminium [18]. Instead, if a base on the Moon surface is considered, more shielding will be necessary. In this latter case the shield should be very thick and made of metal shell in order to protect the astronauts from the primary cosmic rays. However, if the space radiations interact with the shield atoms, secondary particles, such as neutrons and other particles, are produced. These latter particles, if the shield is not

sufficiently thick to contain them, can be worse for the health of astronauts than the primaries. Heavier elements, as lead, can produce more secondaries than lighter ones as carbon or hydrogen. In fact, from the Bethe-Bloch formula it is possible to notice that the stopping power decreases as the mass number of the target increases.

For what concern the neutral particles such as neutrons produced during the interaction of the primaries, they will not undergo Coulomb interaction because they have no charge and so they will proceed for a longer path with respect to charged particles before stopping. Neutrons are so the most dangerous neutral particles because of their lack of charge and high rest mass. Anyway, materials with a high hydrogen concentration are also effective in shielding neutrons. As explained in paragraph 1.3, the neutrons energy can be attenuated thanks to elastic scatterings which diminish neutrons energy until they can be absorbed by the target material. During an elastic scattering the neutron looses part of its energy which is transferred to the target nucleus. As already shown in paragraph 1.3, the lighter elements such as hydrogen are the best at slowing down neutrons with the elastic collisions. When neutrons pass through a material rich in hydrogen, they will loose more or less half of their energy at every collision and in this way they are slowed down quickly. For this reason the better material to shield neutrons are organic compounds which have a high hydrogen concentration.

Chapter 2

The FOOT experiment

The FOOT experiment, as it was already introduced in section 1.1.3, has the purpose to study the differential cross sections of the secondary fragments which are originated during nuclear fragmentation processes between primary beam and target. The beams in analysis can have energies up to 700 MeV/u [29]. These data are used in hadrontherapy and in space radiation protection. Nowadays, several cancer patients are treated with particle therapy which has a very good efficacy in treating tumors that can not be cured with surgery. Since nuclear fragmentation can occur when the beam passes through the patient, this effect has to be carefully studied in order to increase the treatment accuracy at the hadrontherapy energies that range from 150 MeV/u up to 400 MeV/u.

Regarding the second purpose of the FOOT experiment, Solar System explorations are planned, which include long term missions as the exploration to Mars. The main risk is represented by the *Galactic Cosmic Rays* exposition. They have a mean energy range between 700 MeV/u and 1000 MeV/u [30]. Due to the fragmentation process, when they hit the spacecraft shield they can create showers of neutrons or light fragments. The Galactic Cosmic Rays are mainly composed of protons, helium and heavy ions. So, there is an overlap with the measurements for the hadrontherapy aims whereas the principal difference is the energy range [30].

As already pointed out in Chapter 1, fragmentation effects are important and they need to be carefully understood. Due to the experimental difficulties in detecting target fragments, not a lot of data regarding the target fragmentation are available in literature or do not completely describe the fragments produced by beams of charged particles. For this reason, FOOT aims to measure with 5% precision the differential cross sections with respect to kinetic energy and angle at which the fragments are produced. In FOOT studies the fragmentation of beams composed by ^{4}He, ^{12}C and ^{16}O ions hitting against a thin target of carbon or a target with a high hydrogen concentration as polyethylene in the energy range $200 - 800$ MeV/u. The design of the experiment allows to detect, track and identify the charged fragments produced when ions collide against different targets. The goal of the experiment is to measure the projectile and target fragmentation. The

latter one is of great interest when the proton-nucleus collisions take place, but it is very difficult to study because the produced fragments have a short range. So, even if the solid target is thin, the probability of the fragments to escape from the target is really low. For this reason, an *inverse kinematic* approach is used. The fragmentation of several ion beams, such as ^{12}C and ^{16}O against target with a high hydrogen concentration are studied. The cross sections of the proton-nucleus collisions are obtained by subtracting the data taken from $(CH_2-CH_2)_n$ and C targets as described more in details in section 2.1. In addition, the FOOT experiment can measure directly the cross sections of the projectile fragmentation given by beams of He, C and O hitting on a graphite target or polyethylene. Since the material of the target can be changed, other collisions with different nuclei of biological interest are going to be studied. For example the study of collisions against a target of polymethyl methacrylate, PMMA, [30] (for the chemical structure see appendix A) are in the physics FOOT plan.

The aims of the experiment are to measure the differential cross sections with respect to the kinetic energy ($d\sigma/dE_{kin}$) of the target fragments and the double differential cross sections ($d^2\sigma/dE_{kin}d\theta$) of the projectile fragments. The precision required in this two measurements have to be better than 10% and 5% respectively. In order to have this precision, the charge of the fragments and the isotopic identification must be of the order of 3% and 5% respectively, otherwise it will not be possible to have a good separation of the produced fragments [30].

2.1 Inverse kinematics approach

The fragments produced by the target have a low energy and a short range as it was said in section 1.1.3. Since their range is of the order of μm, the fragments will stop inside even the thinnest target practically feasible. As a matter of fact, a target with a thickness of the order of μm has several problems because the target would be fragile and difficult to handle. Furthermore, the interaction rate would decrease and so the time necessary to collect a sufficient quantity of data would become very big.

To overcome this problem, the *inverse kinematics* approach has been introduced. It consists in a switch between the target and the projectile role. In this way it is not a proton beam which is shot against a target of tissue-like material (carbon, oxygen), but tissue-like nuclei will be accelerated against a proton target. This transformation will be only a reference frame change if the kinetic energy per nucleon does not vary. So, the fragments coming from carbon or oxygen beam will have an higher energy with respect to the ones produced by a proton beam with the same kinetic energy per nucleon. Also the mean range will increase and so it will be easier to detect them and to reconstruct the event kinematics. It is possible to employ thicker target in order to have an increased interaction rate.

In order to switch from the two reference systems and derive the cross section, the

Lorentz transformations are applied to convert the coordinates from one inertial reference frame to another one. The beam direction is taken along the positive z-axis and two reference frames are identified: the *laboratory frame*, S, and the *system frame*, S'. In the first one the proton target is at rest whereas the ion beam is in motion along z with velocity β; in the second one the ion is at rest while the proton is moving along the z with equal β but opposite direction. The four-momentum of the ion in S and of the proton in S' are respectively equal to $\mathbf{P} = (E/c, \mathbf{p})$ and $\mathbf{P'} = (E'/c, \mathbf{p'})$ in which E and E' stand for the ion and proton energies. So the components of the proton four-momentum in S' are

$$\frac{E'}{c} = \gamma\left(\frac{E}{c} - \beta p_z\right) \tag{2.1}$$

$$p'_x = p_x \tag{2.2}$$

$$p'_y = p_y \tag{2.3}$$

$$p'_z = \gamma\left(-\beta\frac{E}{c} + p_z\right) \tag{2.4}$$

which can be rewritten with a matrix form

$$\mathbf{P'} = \Lambda\mathbf{P} \tag{2.5}$$

The matrix Λ is a 4×4 matrix given by

$$\Lambda = \begin{pmatrix} \gamma & 0 & 0 & -\beta\gamma \\ 0 & 1 & 0 & 0 \\ 0 & 0 & 1 & 0 \\ -\beta\gamma & 0 & 0 & \gamma \end{pmatrix}. \tag{2.6}$$

In this way, eq. 2.5 can be written as

$$\begin{pmatrix} E'/c \\ p'_x \\ p'_y \\ p'_z \end{pmatrix} = \begin{pmatrix} \gamma & 0 & 0 & -\beta\gamma \\ 0 & 1 & 0 & 0 \\ 0 & 0 & 1 & 0 \\ -\beta\gamma & 0 & 0 & \gamma \end{pmatrix} \begin{pmatrix} E/c \\ p_x \\ p_y \\ p_z \end{pmatrix} = \begin{pmatrix} \gamma E/c - \beta\gamma p_z \\ p_x \\ p_y \\ -\beta\gamma E/c + \gamma p_z \end{pmatrix} \tag{2.7}$$

The inverse Lorentz transformation instead is given by

$$\mathbf{P} = \Lambda^{-1}\mathbf{P'} \tag{2.8}$$

where the inverse matrix Λ^{-1} is

$$\Lambda^{-1} = \begin{pmatrix} \gamma & 0 & 0 & \beta\gamma \\ 0 & 1 & 0 & 0 \\ 0 & 0 & 1 & 0 \\ \beta\gamma & 0 & 0 & \gamma \end{pmatrix} \tag{2.9}$$

from which it is possible to notice that $\Lambda^{-1}(\beta) = \Lambda(-\beta)$ [31].

Due to the Lorentz boost introduction, this kind of approach needs an emission angle measurement with a resolution of the order of mrad. For this reason the projectile and fragments directions are measured very precisely and the multiple Coulomb scattering of every beam particle must be maintained below the mrad. It is also necessary to have a target with a thickness density of the order of 1 gcm^{-2} or lower in order to minimise the probability to have secondary fragmentation inside the target.

The cross section of hydrogen is obtained by combining the cross sections on C and $(C_2H_4)_n$ targets in the following way [32]

$$\frac{d\sigma}{dE_{kin}}(H) = \frac{1}{4}\left(\frac{d\sigma}{dE_{kin}}(C_2H_4)_n - 2\frac{d\sigma}{dE_{kin}}(C)\right) \tag{2.10}$$

2.2 The experimental apparatus

The FOOT experiment [33] is designed intending to do measurements with the desired resolutions and the experimental setup realization is still ongoing in some parts and it will be completed in 2022. It is an experiment whose detector setup has to be transportable because the measurements will be done in different European laboratories. For an experiment with a fixed target, such as FOOT, a magnetic spectrometer made of a dipolar magnet and high precision tracking detectors together with some particle identification detectors is suitable.

A Monte Carlo (MC) simulation, in which an ^{16}O beam with a kinetic energy of 200 MeV/u hits against a target of $(C_2H_4)_n$, has been performed in order to study the angular aperture of fragments. In Figure 2.1 and in Figure 2.1 the simulation results are shown as fragments yields with respect to production angle and kinetic energy of the fragments themselves respectively.

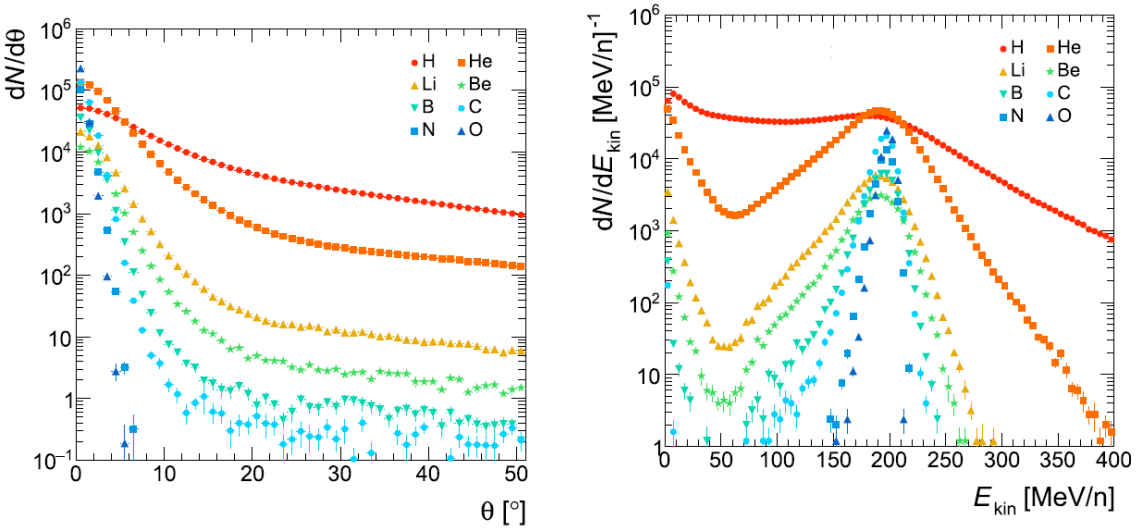

Figure 2.1: *On the left, Monte Carlo simulation of the angular distribution of several fragments originated by a beam composed by* ^{16}O *ions with an energy equal to* 200 MeV/u *hitting against a* 0.5 *cm thick target made of polyethylene [33]. On the right, Monte Carlo simulation of the kinetic energy distribution of several fragments originated by a beam composed by* ^{16}O *ions with an energy equal to* 200 MeV/u *hitting against a* 0.5 *cm thick target made of polyethylene* [33].

It is found that heavier fragments ($Z \geq 2$) have a forward peak inside a polar angle equal to 10° and they have a kinetic energy per nucleon with a peak near to the corresponding primary beam value. On the other hand, the light fragments have the angular and the kinetic energy distributions much more wider. These latter distributions are the ones considered during the arrangement of the experimental set up of the FOOT experiment. Since the lighter fragments, ($Z \leq 3$), have a larger angular aperture, the required magnet size, weight and cost to track not feasible fragments with the required precision, are impossible for a "table top" designed setup. So, the region for the fragments tracking and identification, which includes also the target, can have two different experimental setups: an electronic detector and a magnetic spectrometer developed for fragments heavier than ^{4}He; an emulsion chamber spectrometer for the measurements of low Z fragments. These two experimental setups cover an angular acceptance up to a polar angle equal to 10° and 70° with respect to the beam axis, respectively.

2.2.1 Electronic detector setup

The electronic detector setup [29], [33] has the purpose to measure the fragments which have $Z \geq 4$. In Figure 2.2 is shown the entire setup.

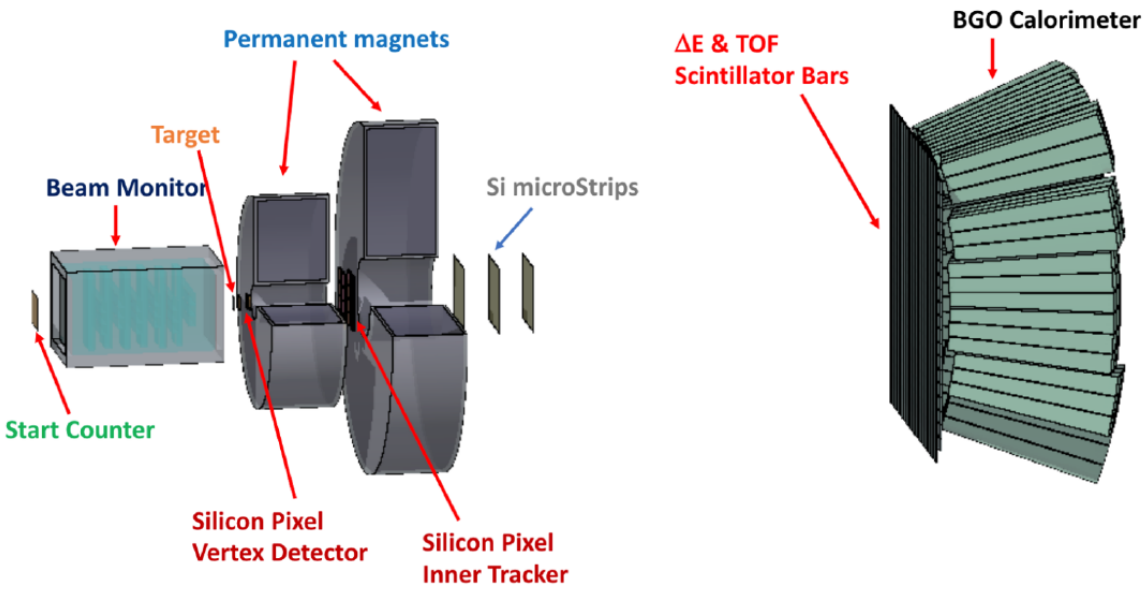

Figure 2.2: *Scheme of the electronic detector setup. All the regions are shown: the pre-target, the tracking and the downstream regions* [33].

The regions in which the setup is subdivided are three and they are:

- *pre-target region*: it consists of the *Start Counter* and the *Beam Monitor*;
- *magnetic spectrometer and tracking region*: the tracking region incorporates the interaction region and it is composed by the target which is followed by three stations of silicon pixels and strips detector placed upstream, between and downstream with respect to the two permanent magnets;
- *downstream region*: it includes two orthogonal planes of thin plastic scintillator bars (*TOF Wall*) placed 1 m far from the target which gives the stop to the TOF signal, and a BGO calorimeter after the TOF Wall to measure the fragment kinetic energy.

Pre-target region

The pre-target region is composed by detectors whose aim is to monitor the beam, providing its direction and the point of interaction on the target and giving the number of impinging ions. The amount of material crossed by the beam has to be minimum in order to bring down the out-of-target fragmentation and the multiple scattering of the beam. For this reason in the pre-target region there are two detectors: the *Start Counter* which is a thin plastic scintillator, followed by a *Beam Monitor* drift chamber detector placed upstream the target.

The *Start Counter* (SC) [33], which is shown in Figure 2.3, is made of a thin squared foil of EJ-228 plastic scintillator with a thickness of 250 μm. The active surface of the foil has a side of 5 cm and it is held thanks to an aluminium support which is encompassed by a black 3D printed box in order to supply the light tightness necessary for the detector functioning. There are two windows in the black box which are placed in correspondence with the scintillator field of view and which are closed thanks to a thin layer made of a 4 μm aluminized mylar (for the chemical structure see appendix A).

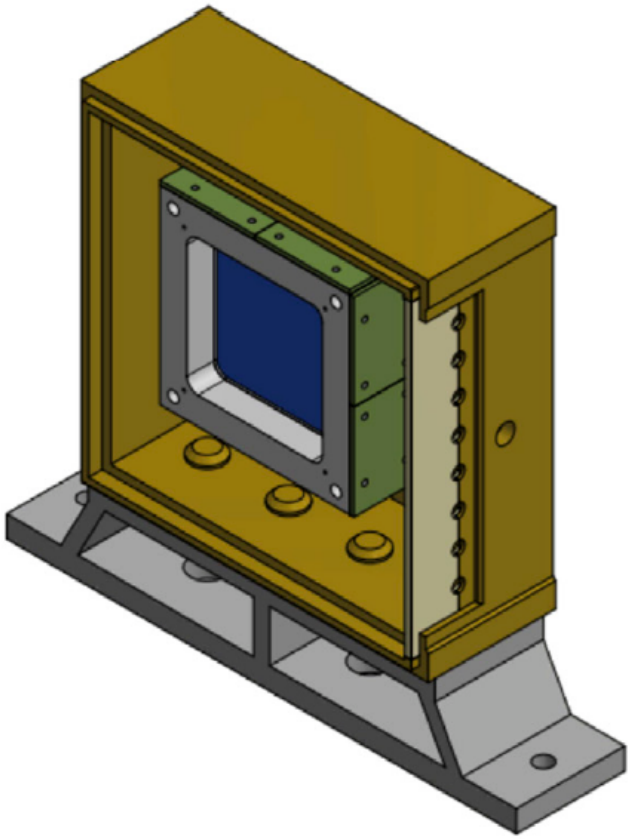

Figure 2.3: *Start counter detector surrounded by the plastic box. The aluminium support holds the plastic scintillator, EJ-228, which is coloured in blue* [33].

The light originated in the scintillator is laterally gather thanks to 48 SiPMs with dimension 3×3 mm^2, 12 for each side, grouped in eight electronic channels, every one reading a chain of six SiPMs. The *WaveDAQ system* controls the readout and the powering of the SiPMs and it can sample the signals until a rate of 5 Gsamples/s in a dynamic range of 1 V. To the arriving signal, before the digitisation process, it is possible to apply a gain between 0.5 and 100 in order to optimise the response of the detector when different beam types or energies are used. Doing so, it is also possible to improve

the detector efficiency that compensates for the low light signal delivered because of the very thin scintillator. The purposes of the SC are to give the minimum bias trigger of the experiment, to do a measurement of the entering ion flux with an efficiency of the order of $\geq 99\%$, to provide to all the other detectors the time of reference and to do the *Time Of Flight* (TOF) estimation together with the TOF-detector and described in section 2.2.1.

The *Beam Monitor* (BM) [33], which is shown in Figure 2.4, is a drift chamber composed by twelve wire layers, with three drift cells for each layer.

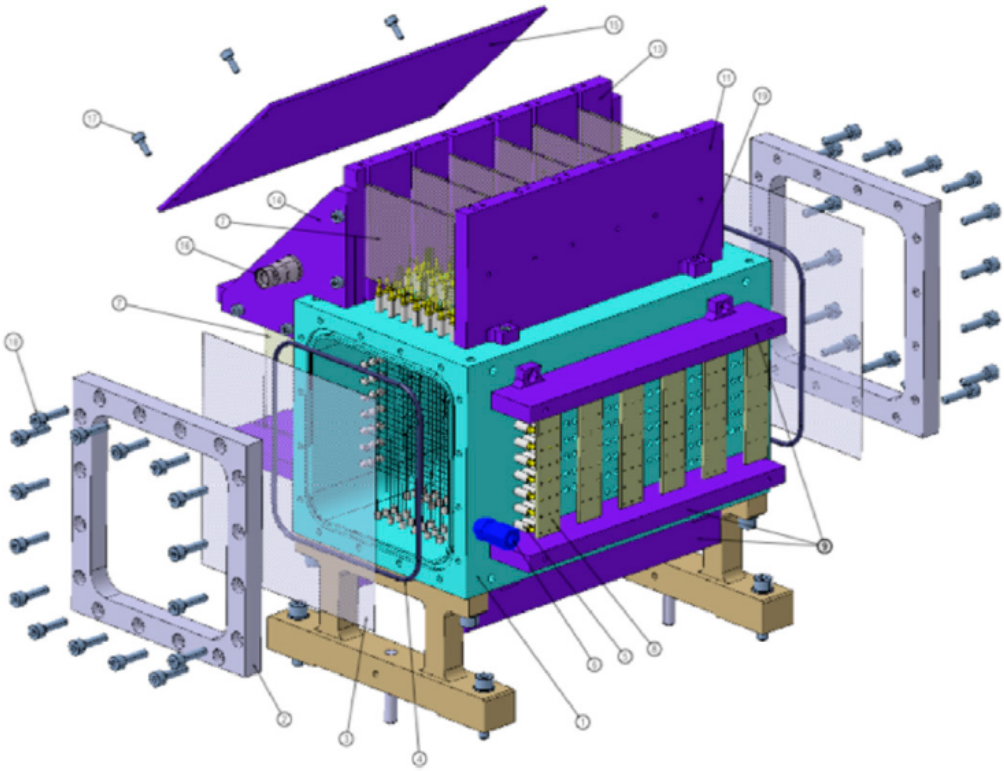

Figure 2.4: *Beam monitor drift chamber with the perpendicular views of the $x - y$ wires and the two windows, made of mylar and held by an aluminium structure, that surround the BM* [33].

In order to reconstruct the beam profile along the x and y axis, the planes containing the wires and orientating through these axis are alternated. The cells have a rectangular shape with dimension of 16×10 mm^2. The BM works at a pressure equal to $\simeq 0.9$ bar with a 80/20% mixture of gas made of argon and carbon dioxide, Ar/CO_2, at a working point between 1850 and 2000 V depending on the primary beam. The efficiency for several different ion beams and energies has been measured and it is equal to $\simeq 90\%$ [33]. The beam monitor is located between the SC and the target and it has to measure

the beam direction and the hitting point on the target. This is necessary to deal the pile-up equivocation in the devices of tracking placed downstream with respect to the target and to reject events during which the beam has produced fragments in the SC giving rise to one or several deviated tracks. To measure the fragments direction with respect to the beam axis, a high spatial resolution is needed in the beam monitor device. In this way the accuracy of the fragments direction will be of the order of few mrad which is necessary in the inverse kinematic to do the measurement of the energy with the desired resolution.

Magnetic spectrometer and tracking region

Since the goal of the FOOT experiment is to accurately identify the charge and isotopes of the produced fragments, it is necessary to do several measurements of the various kinematic variables applying different particle identification (PID) methods. Therefore, in the setup of FOOT also a Time-Of-Flight (TOF) device and a calorimeter are present in order to measure the fragments energy. This latter information, together with the released energy measurements performed by thin detectors and the information given by the magnetic spectrometer, allow to determine the isotope mass. The charge of the fragments that reach the TOF Wall is calculated thanks to the energy loss ΔE and the TOF by means of the Bethe-Bloch function described in section 1.1.1. Measuring the tracks inside the magnet allows to find the fragment rigidity (p/Z) and its path L which gives, together with the TOF and the Z measures, the values of the momentum p and velocity $\beta \cdot c = L/TOF$ of the particle. In the end, the mass of the fragment is found thanks to the momentum p, the velocity β and the kinetic energy E_{kin} measurements applying the following relations

$$\begin{aligned} p &= mc\beta\gamma \\ E_{kin} &= mc^2\left(\gamma - 1\right) \\ E_{kin} &= \sqrt{p^2c^2 + m^2c^4} - mc^2 \end{aligned} \tag{2.11}$$

in which γ represents the Lorentz factor. If the mass and the charge are measured, the fragment is identified in an uniquely way. In the following, the experimental resolutions that are needed to reach the desired precision on the final cross section measurements are reported [33]:

- $\sigma\left(p\right)/p \sim 4 - 5\%$;
- $\sigma\left(TOF\right) \sim 100$ ps;
- $\sigma\left(E_{kin}\right)/E_{kin} \sim 1 - 2\%$;
- $\sigma\left(\Delta E\right)/\Delta E \sim 5\%$.

The design of the detector must keep at minimum the contribution of the fragments generated by the detector materials.

The total length of the detector is of the order of 2 m [32] but it ranges between $2-3$ m when the beam energy is more than 700 MeV/u because the setup length varies with the β of the beam in order to have a constant resolution on the TOF of the fragments.

In Figure 2.5 the tracking system of the FOOT experiment is shown, in which there are three measuring devices put upstream, between and downstream the two permanent magnets.

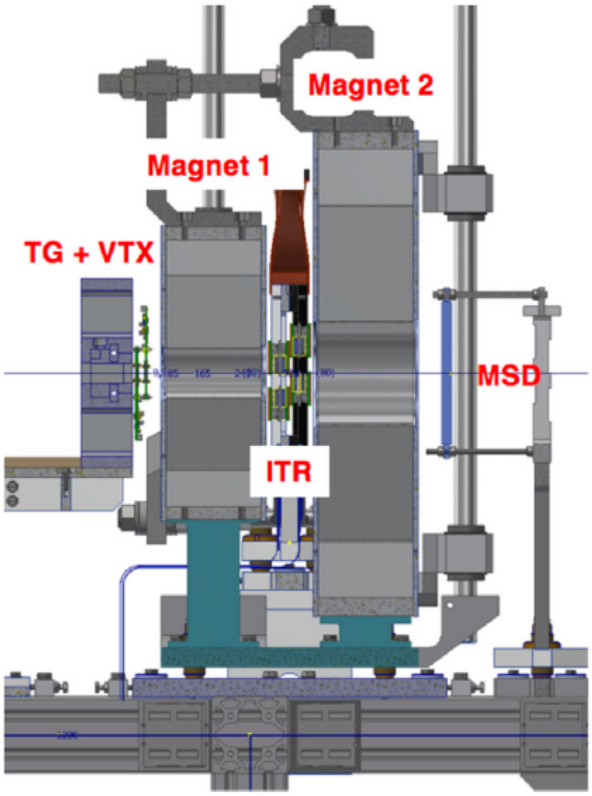

Figure 2.5: *Interaction and tracking system of FOOT. The beam arrives from the left and passes through the target, vertex detector, the magnet region, the inner tracker and, after the second magnet, the micro strip detector* [33].

The first tracking device is the *Vertex Detector* (VTX). In the two upstream stations, the VTX and the *Inner Tracker* (ITR), monolithic pixel sensors are used because of the demands regarding the momentum resolution and global acceptance along with the minimisation of the multiple scattering and re-fragmentation in both the mechanical and the sensors structures themselves. In the downstream region, a *telescope of silicon microstrip detector* (MSD) would be located. Among the three devices there are two

permanent magnets.

The *Target* and the *Vertex Detector* [33] are put in a structure that can support up to five different targets in a sliding tray. In the VTX there are 4 different pixel sensor layers with transverse dimension equal to 2×2 cm^2 put along the z axis. The layers are respectively $0.6 - 0.9 - 2.1 - 2.4$ cm away from the target center in order to have a geometrical acceptance of the order of 40° for the released fragments. Every VTX layers has the technology of the MIMOSA-28 (M28) *Monolithic Active Pixel Sensor* (MAPS), whose sensor is formed by 928×960 (rows×columns) pixels of 20.7 μm of pitch. The global dimension of the chip is 20.22×22.71 mm^2. Each M28 sensor has a thickness equal to 50 μm and so the overall thickness of the VTX is 200 μm. The VTX detector has a spatial resolution of 5 μm that supplies an angular accuracy of the order of milliradiant together with the information coming from the BM. Furthermore, the multiple scattering process is minimised thanks to the lessen material used both in the BM and VTX.

In order to bend the fragments originated in the target, a *Magnetic System* (MS) [33] is used. Since the system is required to be portable and because of the desired resolution on the momentum, the magnets are permanent and gives rise to the needed $\left(\vec{B} \times \vec{L}\right)$ in which $B = B(z)$ is the intensity of the magnetic field and L is the length of the magnetic field region along the z axis. This region is approximately between the VTX and the MSD trackers and in it the particles feel the magnetic field effect. The final MS configuration is given by a magnetic system held in air with two magnets arranged in the Halbach configuration. This configuration permits to have a further tracking station between the two needed in order to achieve the desired momentum resolution. Furthermore, thanks to the Halbach configuration the magnetic field inside the internal hole of the cylindrical permanent magnet is roughly a dipolar one. The magnetic field grows up with the external radius of the cylinder whereas it diminishes with the gap radius. Thus, two magnets with different dimensions are used in order to achieve the desired momentum resolution with the needed $(B \times L)$ and the angular acceptance equal to 10° for the produced fragments. The first one has a diameter gap equal to 5 cm whereas the second magnet has the diameter gap of the order of 10.6 cm. The maximum intensities are respectively 1.4 T and 0.9 T along the y direction in the internal cylindrical hole. The intensity along the z axis of the cylinder has a Gaussian behaviour for every magnet. The inner tracker, which is located between the two magnets, feels an intensity of the order of ~ 0.6 T. In every magnet there are twelve units made of Samarium-Cobalt which are able to conserve their magnetic properties even in environments with a high radiation level. The two magnets are grouped in a single mechanical system which is able to resist to the produced magnetic forces and to supply a high precision during the alignment with the tracking stations. In Figure 2.6 the magnetic map is reported.

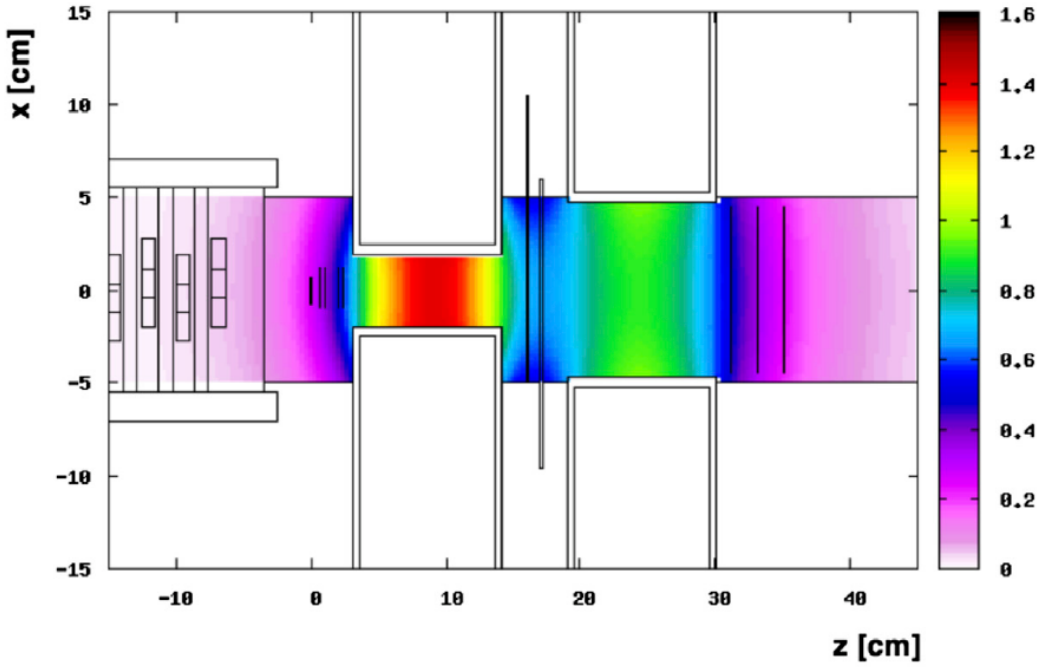

Figure 2.6: *Magnetic field map given by the magnets of FOOT arranged according to the Halbach configuration. In the palette it is reported the magnetic field intensity of the component along the y axis* [33].

The magnets can be also displaced along the vertical direction of nearly 40 cm with respect to the beam line. In this way, it is possible to inter-align the tracking stations during some particular run without the magnets.

The *Inner Tracker* (ITR) [33] is composed by two planes of pixel sensors with the aim of tracking the fragments in the magnetic region. In order to achieve the desired acceptance, granularity and tracking performance, every plane has a sensitive area equal to 8×8 cm^2 and 16 M28 sensors per layer. Since the detector area is larger than the one of the VTX, a mechanical support is necessary. The ITR ladder performs a double-sided layout which has two M28-sensor layers modules. The layers are glued on the opposite sides of the support structure, with a thickness equal to 2 mm, that is made of low density silicon carbide (SiC) foam. In every module there are four M28 sensors which are glued and bonded on a flex cable made of kapton-metal. The cables are used to provide the communications and services of the sensors to and from the external world. The total budget of the ITR ladder material is equal to $x/X_0 \simeq 0.3\%$ in which x is the ITR ladder whole thickness and X_0 represents the radiation length of the ITR ladder itself. The ITR is formed by two ladders for each plane with in total four ladders held thanks to a metallic structure which supports the entire tracker.

The *Microstrip Silicon Detector* (MSD) [33] has the purpose to track the fragments in the region downstream the magnetic one in order to measure the momentum and to

compare the reconstructed tracks with the hits in the TOF Wall and in the calorimeter. The MSD can also give information about the dE/dx for the reconstruction of the fragments charge together with the one given by the TOF Wall. The three $x-y$ planes of the MSD have an active area equal to 9.6×9.3 cm^2 and they are separated by a gap of 2 cm along the beam line. They are positioned just after the second magnet to have the required angular acceptance for the measuring of the ions with $Z > 2$. Every MSD $x-y$ plane has two orthogonal *Single-Sided Silicon Detector* (SSSD) sensors 150 μm thick. In this way the amount of material is minimised and it is possible to readout the $x-y$ coordinates. Every sensor is fixed on a hybrid *Printed Circuit Board* (PCB) which gives the mechanical support and the interface with the readout of the MSD. Metallized sensors backplane are used to guarantee the light tightness. A 50 μm strip pitch is used to reduce the pile-up of the fragments in the same strip. Making a digital readout of the strip with a 150 μm pitch, the spatial resolution is $\simeq 40$ μm.

Downstream region

This region represents the last part of the apparatus. It is at a distance of 1 m from the target and its goal is to give the stop to the TOF measurement and to measure the fragment energy loss and kinetic energy. It is formed by two perpendicular planes of plastic scintillator bars followed by the BGO calorimeter. In Figure 2.7 a layout of the fragment identification region is shown.

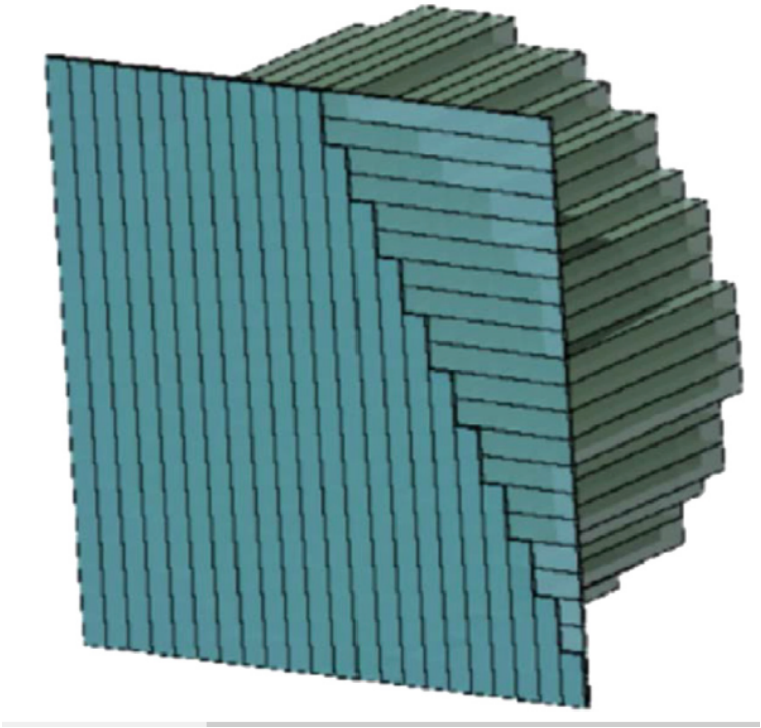

Figure 2.7: *Scheme of the fragment identification region with the two perpendicular plane of* 20 *bars made of plastic in front of the BGO crystal matrix used in the calorimeter* [33].

In the *TOF Wall detector* (TW) [33] there are two layers of 20 plastic scintillator bars, EJ-200, settled in a perpendicular way and enveloped with reflective aluminium and black darkening tape. The thickness, the width and the length of every bar are 0.3 cm, 2 cm and 44 cm, respectively. The detector active area is 40×40 cm^2 and it gives the measurements of the deposited energy, ΔE, the information required to determine the TOF and the hit position. Thanks to the concurrent measurement of TOF and ΔE, it is possible to determine the charge Z of the incoming ions thanks to the Bethe Bloch formula (1.4). The identified Z of the particle is used to find out the fragment mass and, in conjunction with the $x - y$ hit position, as a seed for the tracking of the fragments throughout the magnetic region. The transverse dimensions are constrained by the angular aperture of the heavy fragments at a distance of the order of $1 - 2$ m, whereas the granularity is selected in order to have the pile-up of several fragments in the same bar lower than 1%. The bar thickness, instead, has been selected as a compromised between a high scintillation signal, so a better resolution in timing and energy, and a lower probability of secondary fragmentation in the bars, which would ruin both the identification and tracking of the particle. Four silicon photomultipliers are connected to each of the two borders of the TW bars, with an active area is 3×3 mm^2 and the microcell pitch of the order of 25 μm. The bars thickness and the chain of the readout are

chosen in order to achieve a resolution on the TOF better than 100 ps and a resolution on the energy loss of heavier fragments equal to $\sigma(\Delta E)/\Delta E \simeq 5\%$. The fragments can be identified even if they release different energies because the number of pixel per channel of the SiPM is very high, 4×14400. In the end, thanks to the elevated precision time measurement it is possible to find the hit position along the bar with precision better than 8 mm.

The *calorimeter* [33] is the last detector of the whole setup and it has the goal to measure the kinetic energy of the fragments necessary to calculate their mass. Different kind of phenomena can happen inside the calorimeter depending on the energy of the entering fragment. For higher energies of the order of $\simeq 700 - 800$ MeV/u, which are of interest for space radiation protection studies, hadronic shower occur since the threshold for the production of the pion is exceed. However, a very good resolution is needed in the studies regarding the target fragmentation in which beams of ^{12}C and ^{16}O of energies up to 200 MeV/u are used. At these energies the principal process of energy loss is through electromagnetic interaction with the electrons and nuclei of the target. So, it is possible to achieve a good containment of the fragments and to maximise the resolution of the energy. Nevertheless, a systematic error is present that ruins the energy resolution because neutrons are produced during interactions causing an escape of some energy of the fragments. Anyway, this effect can be minimised thanks to the surplus of information derived from the other detectors. Because of the low intensity of the beam in FOOT, the calorimeter is made of a dense crystal which has a high light yield and no stringent requisites regarding the response velocity. For these reasons the material chosen is the bismuth germanium oxide, $Bi_4Ge_3O_{12}$ or BGO, that has a high density, $\rho = 7.13$ g/cm^3, therefore assuring a high stopping power and a light yield of the order of $\simeq 10$ photons/KeV. In the FOOT calorimeter there are 320 BGO crystals placed according to a disk-like structure with a radius of $\simeq 20$ cm and divided in modules of 3×3 crystals because in this way it is easier to control their positioning and weight. The crystals shape is a 24 cm length truncated pyramid whose front face has a dimension equal to 2×2 cm^2 whereas the back face is 3×3 cm^2. The transverse size of the BGO crystal and the granularity of the TOF Wall are very similar. Even if multi-fragmentation events occur, the probability of pile-up in the same crystal is maintained below $\simeq 1\% - 2\%$ depending on the energy of the beam and on the configuration of the setup in the experimental room. The depth of the crystal is chosen to minimise the leakage of the energy essentially given by the neutrons that escape from the calorimeter. To each $Bi_4Ge_3O_{12}$ crystal a 25 SiPMs matrix is linked with an active surface equal to 2×2 cm^2. Every microcell has 15 μm pitch which is sufficiently small to have a linear response up to 10 GeV energy. Every SiPMs matrix is linked also to a readout board which is designed in order to correspond the SiPMs dimensions. In this way the design of the overall detector results to be very compact. The Front-end board is interfaced with the WaveDAQ system which is the same employed in the SC and TW detectors. That system can sample the signal at 1 Gsample/s and so it is possible to do measurements that depend on both signal amplitude

and integral and to do a shape analysis. This board is used also to perform the readout of the SiPM temperature sensor which is used to compensate the variation of the system response due to variations in the temperature and to equalise the response offline of the calorimeter. The energy resolution, $\sigma(E_{kin})/E_{kin}$, has been measured and it is less than 2% as it is asked for the heavier fragments.

2.2.2 Emulsion spectrometer

The *emulsion spectrometer* (ES) [33] is used in order to identify the low Z fragments production. In Figure 2.8 the ES arrangement inside the FOOT experiment is shown.

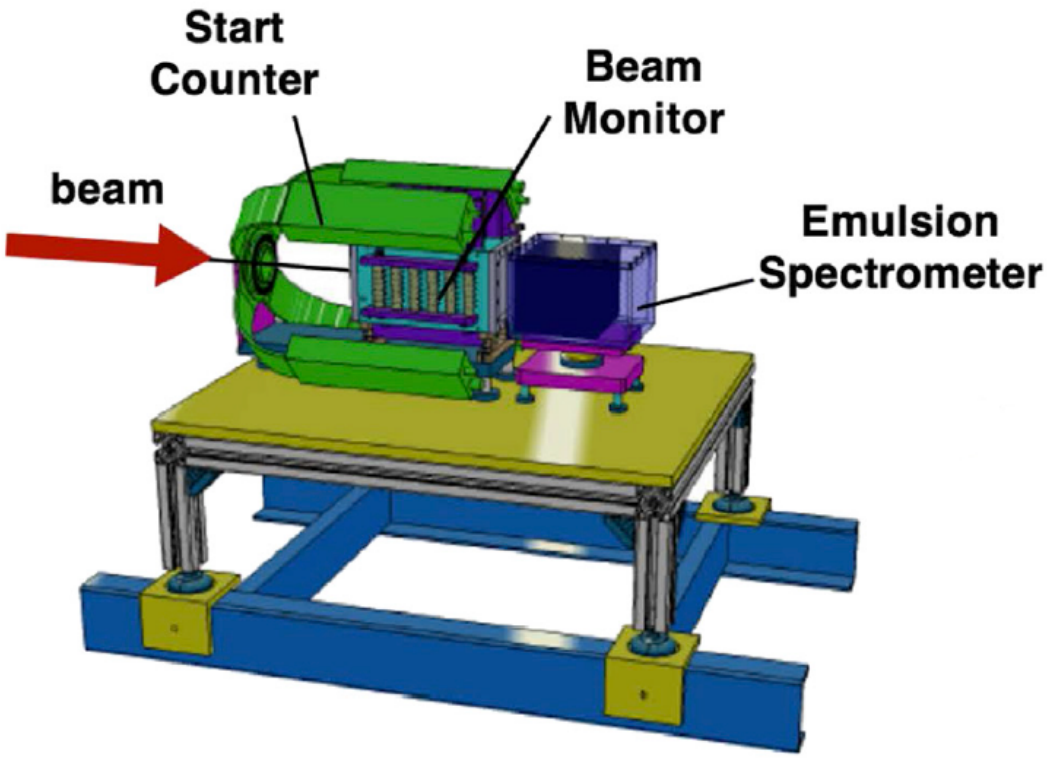

Figure 2.8: *Setup of the emulsion spectrometer which is placed downstream with respect to the SC and BM* [33].

It is located after the SC and the BM with the beam arriving from the left. The SC and BM are used to control the beam flux on-line in order to avoid a spatial pile-up of events on the ES active surface. The emulsion detectors have the highest spatial resolution, of the order of submicrometer, for tracking ionizing particles among the tracking instruments. The setup composed by the ES, target and detector is really compact and thanks to the emulsion chamber it is possible to rebuild very precisely the interactions

that have taken place inside the target. The main characteristics of the emulsion chambers are their capability to measure particles that are emitted with an angular acceptance over 70° with respect to the incident angle with a high spatial resolution. For this reasons they are employed in experiments in which fragments at large angles are produced by ^{12}C ions hitting against thin target at the energy range of proton therapy.

In FOOT, the nuclear emulsion films are composed by two sensitive layers with a thickness of 70 μm which are placed on both sides of a plastic base which is 210 μm thick. The final thickness is therefore 350 μm. The sensitive regions are made of silver bromide crystals, AgBr, with a diameter equal to 0.2 μm and that are dispersed in a gelatin binder which can detect charged particles. Thanks to sensitised crystals along the particle path, it is possible to reconstruct the track. Through the *development*, a chemical process, the latent images are increased and a silver clusters growth (grains) is produced. The grains have a diameter of 0.6 μm and so they can be seen with optical microscopes. There is a direct proportionality between the charge particle ionization and the number of grains inside the dynamical range of the detector. The emulsions are so scanned to obtain an image which is analysed with a software in order to identify clusters of dark pixels aligned. These letter ones represent the track of the incoming particle. The *micro-track* is given by a series of pixels in one layer of emulsion, whereas the *base-track* is set by two aligned micro-tracks that are part of the top and bottom emulsion film layers. The found base-track has a position accuracy equal to 1.0 μm and an angle accuracy of 3 mrad. If the base-tracks are on the same straight line through several films, a *volume-track* is formed. The pixel sum of the grains of a specific volume-track is sensible to the particle charge.

In FOOT the ES is composed by passive materials alternated with nuclear emulsions films which are used as tracking devices and ionization detectors. The ES is made of three part:

- *Interaction and vertexing region*: it is composed by layers made of target element, C and $(C_2H_4)_n$, alternated with film of emulsion as it is shown in Figure 2.9.

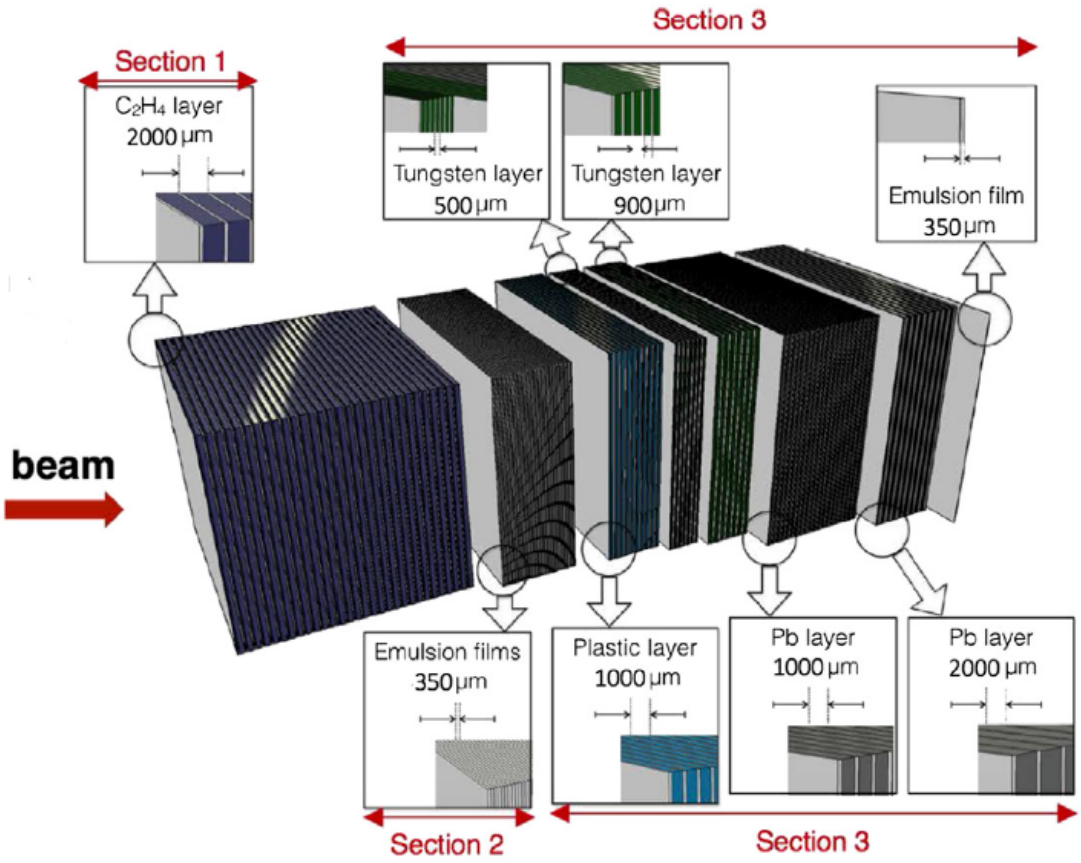

Figure 2.9: *ES composition scheme with the target made of* $(C_2H_4)_n$ [33].

If the ion beam interacts with this cells giving rise to the production of secondaries, the fragments are detected by the subsequent spectrometer regions. The emulsion detector will reconstruct the fragments tracks and the position of the interaction vertex. The total number of cells is optimised in order to have a statistically significant number of reactions.

- *Charge identification region*: when the particles are at the minimum of their ionizing power, they give rise to thin tracks in the emulsion whose grains density is between 30 and 50 grains/100 μm. Particles with high ionizing power can cause a saturation effect which prevents the charge identification. Anyway, if the emulsion is kept for approximately 24 hours at high temperature, above 28 °C, and at high degree of humidity, 95%, it is possible to induce a fade which can partially or totally cancel the tracks of the particles. Using several layers and having undertaken different thermal processes after the exposition can solve saturation effects of particles that have different ionizations. In this part of the ES the identification of

low Z fragments (H, He, Li) charge is done thanks to elementary cell constituted by four emulsion films. Each emulsion is exposed to a different thermal treatment after the exposure and before the development. In this way, every track is identified by four track volume variables for every thermal condition. These variables will be proportional to the density of the silver grains along the trajectory. All the tracks in the emulsion which is not thermally treated, will be visible and because of the saturation effect the separation of the charge is impossible.

- *Momentum measurement region*: this part of the ES is composed by emulsion films alternating with layers made of passive materials. The section length, the passive layers number and the layers thickness will depend on the beam energy. Usually, the passive materials are tungsten, W, lead, Pb and Lexan which is a polycarbonate. The momentum will be estimated thanks to the range technique in which it is used the correlation between the range and the kinetic energy. For this reason the tracks length of all the particles is measured. This method however depends on the segmentation in passive layers, on their thickness and the material they are made of. The material is chosen in order to stop the crossing fragments, so at the beginning of the stack there will be passive layers made of lower Z materials whereas at the end of the stack there will be higher Z material layers. In this way the dynamical range of the momentum measurement is grown up. Thanks to the measurement of the particle trajectory it is possible to evaluate also the momentum of the charged particles using the *Multiple Coulomb Scattering* method (MSC). The $x-y$ spatial coordinates and the slope (θ_x, θ_y) are estimated for every particle track and the momentum is found thanks to the relation

$$p\,(MeV/c) = \frac{13.6}{\beta\delta\theta\,(mrad)} Z\sqrt{\frac{x}{X_0}} \tag{2.12}$$

in which p represents the momentum of the fragment, β is its velocity, Z stands for its charge, X_0 denotes the radiation length in the material and $\delta\theta$ illustrates the track slope deviation along the fragment path. Thanks to the range and MSC methods together with the charge measurement, the mass of the fragments for the identification of isotopes can be found.

2.3 Neutrons detection in the FOOT experiment

The scintillator detectors [1] are widely used to detect particles and they exploit a characteristic, named *luminescence*, of certain materials which can emit a flash of light, called *scintillation light*, when they are hit by particles or radiation. The scintillation is converted into an electric signal thanks to an amplifying instrument as the photomultiplier. In this way the electric signal can be analyzed in order to derive information regarding

the incoming particle. In Figure 2.10 the elements composing a scintillator detector are shown. The incident ionizing radiation is transformed into visible light which is detected by a photomultiplier tube and converted into an electric signal.

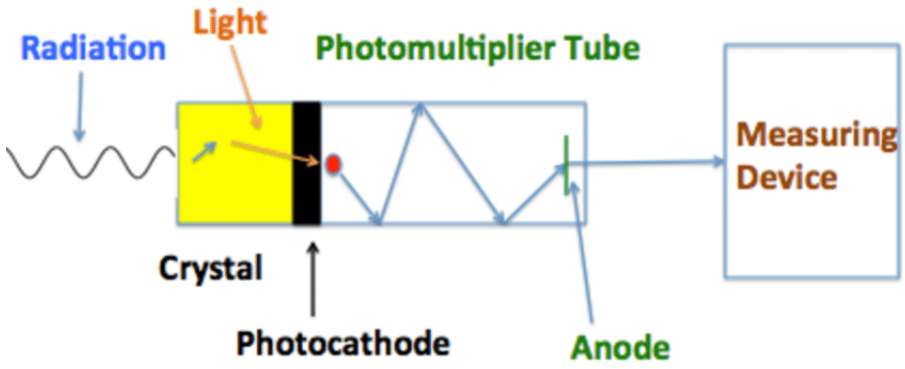

Figure 2.10: *Scheme of a scintillator detector. The radiation hits the crystal in which some light is produced. Then, the light is detected by a photomultiplier tube and converted into an electric signal which can be analyzed* [34].

Normally, a radiation passes through the scintillator exciting its atoms and molecules. In this way some light is emitted and it is transmitted to the photomultiplier (PM) which is optically link to the scintillator either directly or with light guides. In the PM, the light is converted into a weak photoelectrons current that is amplified thanks to an electronmultiplier system. The final electronic signal is then transmitted to an electronic system in order to be analyzed. The most important characteristics of a scintillator are the following:

- *Sensitivity to energy*: above a given threshold the light emitted from the scintillator is directly proportional to the exciting energy. Also the amplitude of the final electric signal is proportional to the energy deposited in the scintillator because the PM is a linear instrument.

- *Fast time response*: with respect to the other detectors the scintillator ones are faster and their response and recovery times are shorter. This characteristic allows to derive some time information and to use higher count rates because the dead time, which is the time lost during the scintillator recovery, is lower.

- *Pulse shape discrimination*: with some scintillators it is possible to do particles discrimination by analyzing the signal shape of the emitted light. This is caused by the excitation of different mechanism of fluorescence given by particles that have several ionizing energy.

- *Efficiency*: the efficiency in the conversion of the exciting energy into fluorescent light must be high.
- *Transparency*: the medium must be transparent to its own fluorescent radiation in order to transmit the light.
- *Detectable emission*: consistence between the emission spectral range and the spectral response of the photomultipliers.
- *Decay time*: the decay constant of the induced luminescence must be short to generate fast signal pulses.

If the scintillation process takes place 10^{-8} s after the absorption, it is called *fluorescence* whereas if more time is necessary, it is named *phosphorescence* or *afterglow* and it can last from few microsecond to hours depending on the material.

The reemission process time can be described with a two-components exponential decay

$$N = A \exp\left(\frac{-t}{\tau_f}\right) + B \exp\left(\frac{-t}{\tau_s}\right) \tag{2.13}$$

in which N is the number of emitted photons per unit time t, τ_f represents the fast decay constant, τ_s stands for the slow decay constant, whereas A and B are the magnitudes of the fast and slow components respectively. These two magnitudes depend on the material even if the fast one is usually dominant. In Figure 2.11 the relation between the fast and slow component is reported.

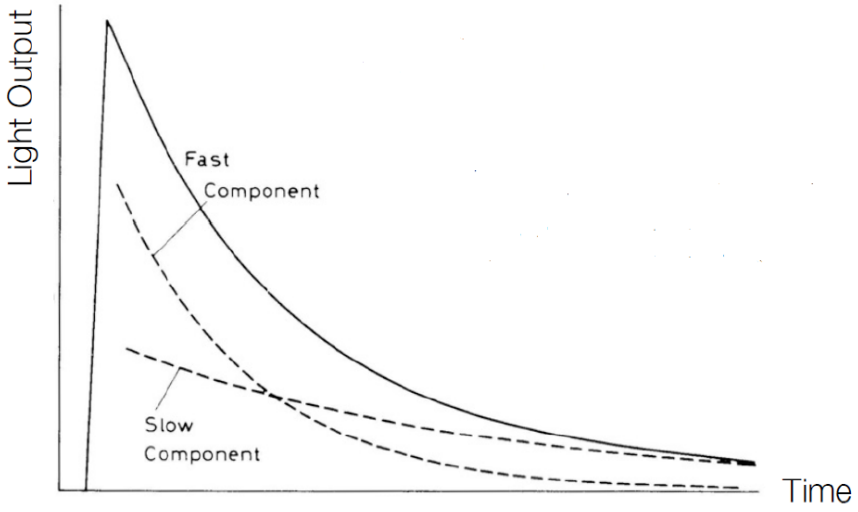

Figure 2.11: *Exponential decay of a scintillator with the two exponential components, the fast and the slow one, drawn with two dashed lines. The solid line represents the total curve of the light decay* [35].

Currently, there are six kind of scintillator materials which are the organic crystal, organic liquids, plastics, inorganic crystals, gases and glasses. For what concern the analysis done in this thesis, an organic liquid scintillator described in detail in section 2.3.1 is used, for the reasons explained in section 1.3.

The organic scintillators are aromatic hydrocarbons in which several benzene molecules (for the chemical structure see appendix A) are condensed together or linked. Their most important characteristic is the very fast decay time which is of the order of few nanoseconds or less. The scintillation light is produced thanks to the transitions of the free valence electrons that belong to the π *molecular orbitals* of the molecules. In every aromatic compound these free electrons do not belong to a given atom in the molecule but they are delocalized and they form two electronic clouds one above and the other under the ring plane [22]. An energy diagram of these kind of orbitals is shown in Figure 2.12.

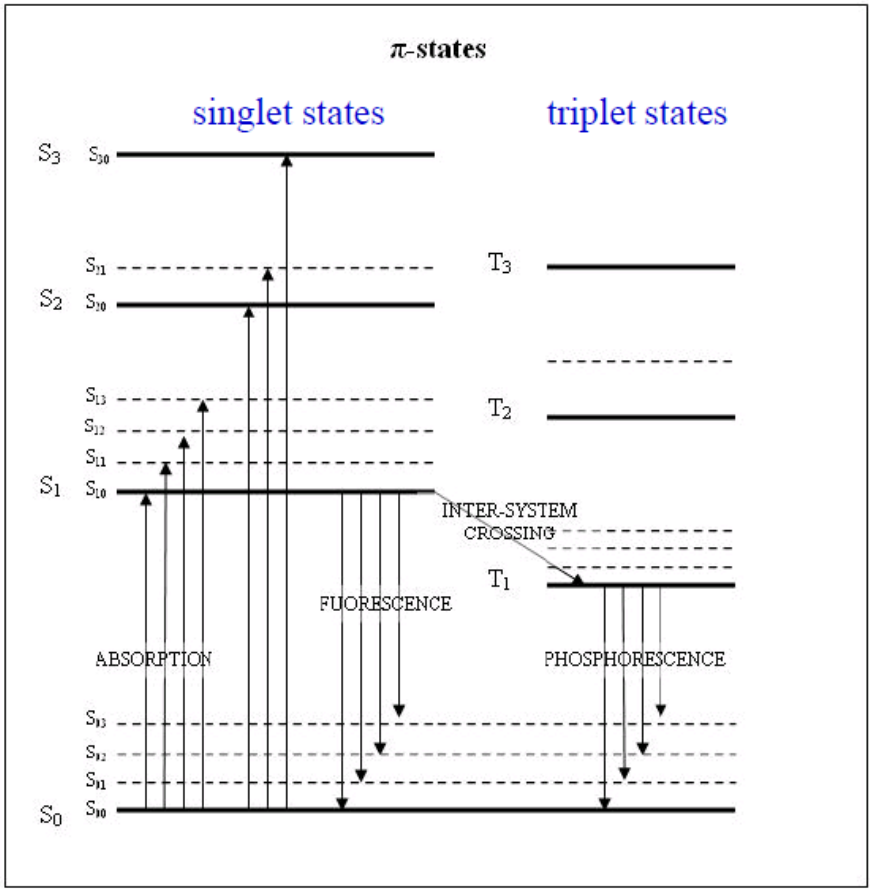

Figure 2.12: *Energy diagrams of the π molecular orbitals in which the singlet and triplet states are shown. S_0 is the ground singlet state, the S_1, S_2 and S_3 represent the excited singlet states, whereas T_1, T_2 and T_3 stand for the excited triplet states. The states S_{00}, S_{01}, S_{10}, S_{11} and so on denote the vibrational sublevels* [35].

Above the ground singlet state, S_0, there are the excited singlet states, S_1, S_2 and S_3, the lowest triplet state, T_1, and its excited states, T_2 and T_3. Related to every electron level there is the fine structure which is the excited vibrational sublevels of the molecule. The energy gap between the electron levels is of the order of few eV, whereas the space between the vibrational levels is of the order of few tenths of eV. The ionization energy released by the incoming radiation can excite both the electron levels and the vibrational sublevels. The time necessary to the singlet excitation to decay to the S_1 state without emitting radiation is very short, $\leq$ 10 ps. This process is called *internal degradation*. Then, from the S_1 state usually a radiative decay to a vibrational level of the ground state S_0 takes place in few nanoseconds. The process just described is the fluorescence one and it is represented by the prompt exponential component in eq. 2.13. During the decay of S_1 state into a vibrational state of S_0 the emitted radiation energy is less then the one necessary for the transition $S_0 \rightarrow S_1$. This explains the transparency characteristic of the scintillators to their own radiation. For what concern the triplet excited states, instead, an internal degradation similar to the singlet one takes place and it brings the system to the lowest triplet state. Since the decay from a T_1 state to a S_0 state can happen but it is highly forbidden, the T_1 state needs to interact with one more excited T_1 state molecule in order to leave one of the two molecules in S_1 state. The reaction described above is reported in the following equation

$$T_1 + T_1 \rightarrow S_1 + S_0 + photons \tag{2.14}$$

Subsequently, the S_1 state emits the radiation as it was reported before. The light produced in this process is emitted with a delay time which is a characteristic of the interaction among the excited molecules. This light represents the slow or delayed component of the scintillator which is important only in some organic materials otherwise its contribution is not so considerable. Since the luminescence is a characteristic of the organic compounds they are used as detector scintillators both in crystal form and liquid or solid solutions. So, the organic scintillators can be divided in organic crystal, plastic and organic liquids.

The *organic crystals* used in scintillator detectors usually are the anthracene the naphtalene and the trans-stilbene (for the chemical structure see appendix A). The response of these compounds is very fast, more or less few nanoseconds, except for the anthracene whose decay time is $\simeq$ 30 ns. On the other hand, their amplitude response is anisotropic and so it differs with the orientation of the crystal. For this reason the energy resolution is not good if the source is not collimated. Anyway, the crystals are very hard and durable and in particular the anthracene has the characteristic of having the highest light output with respect to all the other organic compounds. Therefore, it is taken as reference to which compare the light outputs of other scintillators as it was done for the BC-501A in section 2.3.1. The outputs are so indicated as percent of the anthracene light.

The *plastic scintillators* are composed of solutions in which a liquid organic solute is dissolved in a solid plastic solvent. Usually the plastics used are similar to the polystyrene (for the chemical structure see appendix A). Together with primary solutes, which have concentrations of the order of 10 g/L, sometimes secondary solutes at very low concentrations are present in order to shift the wavelength. The plastics scintillators give a very fast signal with a decay constant equal to $2 - 3$ ns and they have a high light output. Furthermore, they are flexible and enough robust even if they can be damaged quite easily by organic solvents or acids.

The *organic liquid scintillators* are made of liquid solutions made up of one or more liquid organic scintillator solutes dissolved into an organic solvent. The energy is mainly absorbed by the solvent and then it is given to the scintillation solutes by a transfer which is very fast and efficient. The compounds most used as solutes are the p-Therphenyl, the POPOP (for the chemical structure see appendix A) and similar, whereas the best solvents are the benzene, the toluene, the mixture of the three xylene compounds, the decaline (for the chemical structure see appendix A) and other cyclic or aromatic compounds. One of the properties of these scintillators is that their efficiency grows up with the concentration which is usually of the order of 3 g of solute per litre of solvent. The scintillators response is fast enough and the decay times are of the order of $3 - 4$ ns. An advantage of these scintillators is that they can be filled with other substances to grow up the efficiency for a given application. Some of the materials added are *wavelength shifters* that can absorb light with a given frequency and then emit it with another one. In this way the emitted light spectrum is more compatible with the one of the photomultiplier cathode. However, adding this substances can cause an increase in the decay time and a decline in the light output because of the quenching effect which is the reduction of the population in an excited state [36]. Furthermore, the liquid organic scintillators are more sensible to solvent impurities.

2.3.1 The BC-501A detector

The BC-501A [37] is a liquid scintillator used to detect neutrons when also gamma-radiation is present. It yields a very good *pulse shape discrimination* (PSD), (see section 3.3), in order to carry out a neutron-gamma discrimination. Often the BC-501A is enclosed in cells made of metal or glass. In Table 2.1 the scintillation characteristic and the atomic composition of the constructing materials are reported, whereas in Table 2.2 more specific technical data are shown.

Table 2.1: *Characteristics of BC-501A detector regarding its scintillation quality and its atomic composition. The hydrogen, carbon and electrons concentrations are reported in molarity [M], which is measured mol/L and gives the solute moles in a liter of solution* [37].

Scintillation Properties	BC-501A
Light Output [% Anthracene]	78
Wavelength of maximum emission [nm]	425
Decay time, short component [ns]	3.2
Atomic Composition	
H concentration [M]	80
C concentration [M]	66
Ratio H:C	1.212
Electron concentration [M]	48

Table 2.2: *Technical data of the BC-501A detector* [37].

General Properties	BC-501A
Density [g/cm^3]	0.874
Refractive index, n_D	1.505
Refractive index at 425 nm	1.530
Flash Point, T.O.C.	24°
Mean decay times of first three components [ns]	3.16 – 32.3 – 270
Mean life time for energy transfer from solvent to solute [ns]	1.66
Number of photoelectrons/ KeV energy loss using Burle 8575 phototube	1.7
Ratio alpha:beta fast	0.073
Ratio alpha:beta slow	0.098
Response to protons	$E = 0.83P - 2.82\left[1 - exp\left(-0.25P^{0.93}\right)\right]$ in which P is the proton energy in MeV and E represents the electron energy in MeV that gives the same light output

Figure 2.13 shows the BC-501A detector emission spectrum required to find the luminous response that the photodetector needs to have in order to obtain a good conversion of the emitted light into electric current. In Figure 2.14, instead, the pulse shape discrimination execution is reported for three different energy thresholds. It is possible to notice two kinds of pulses, the first one corresponds to the gammas whereas the second one represents the neutrons.

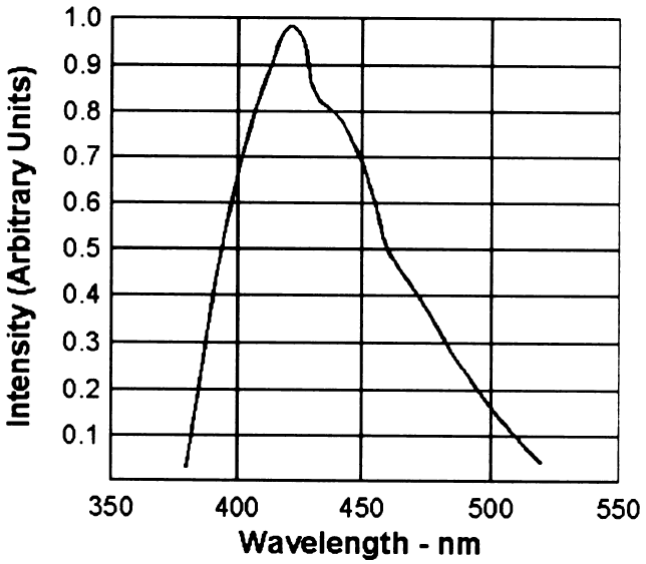

Figure 2.13: *Spectrum of the BC-501A detector* [37].

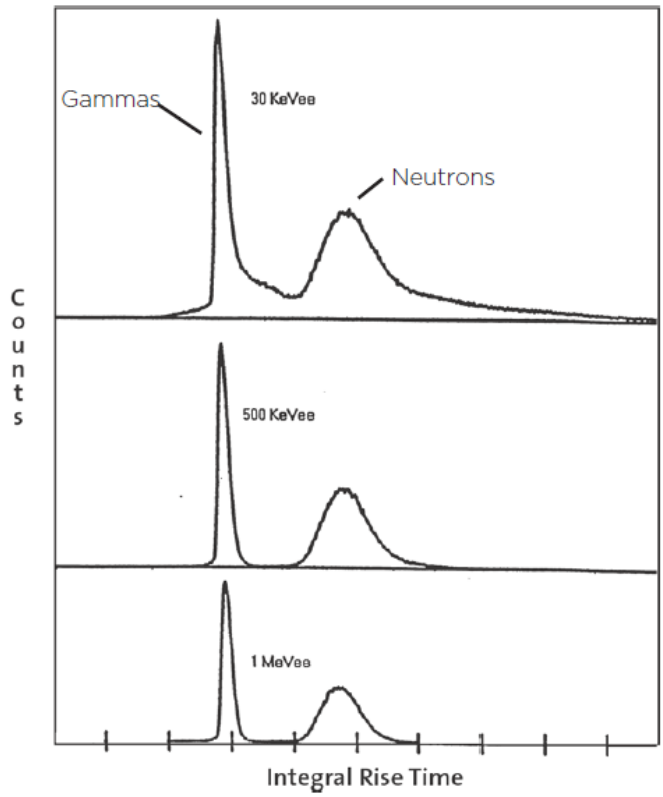

Figure 2.14: *Pulse shape discrimination execution of the BC-501A detector* [37].

Chapter 3

Data Analysis

3.1 Data sample

The FOOT setup used at GSI, in Darmstadt, Germany, [38] is shown in Figure 3.1. It is located at a height of 198 cm from the floor and it is 2 deg lower than the beam line.

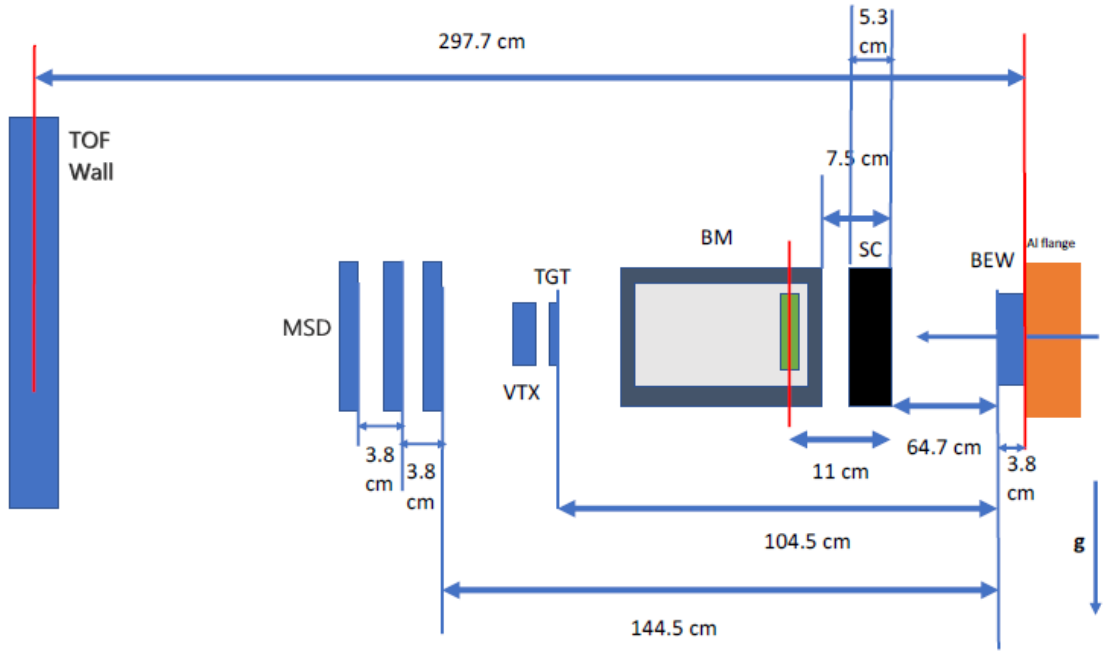

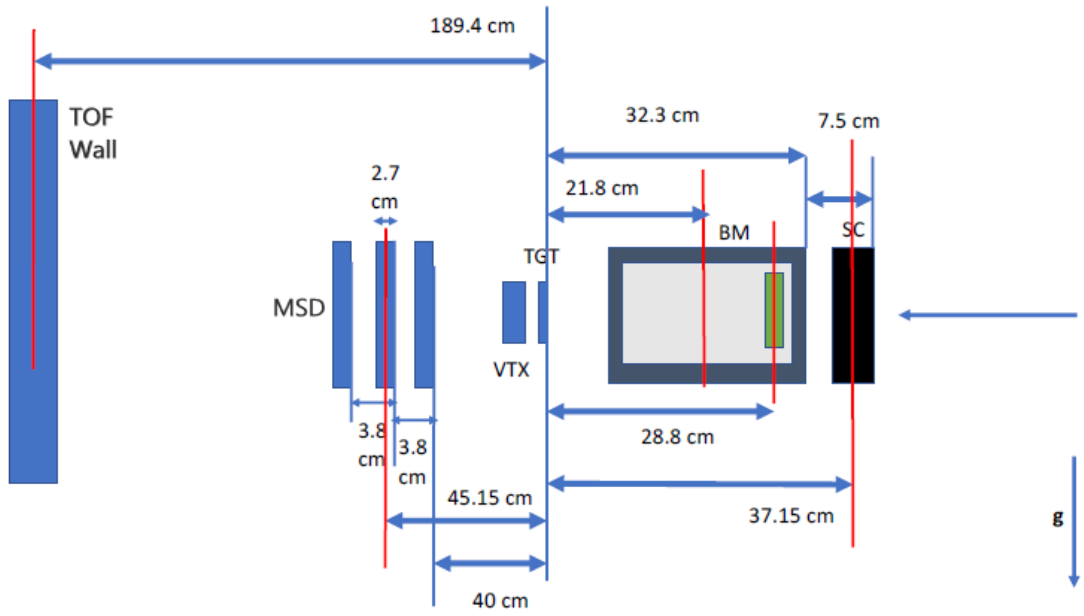

Figure 3.1: *Geometry of the experiment done at the GSI seen from above.*

In the experiment, a beam of oxygen, ^{16}O, exits the *beam exit window* (BEW) with an energy equal to 200 MeV/u and 400 MeV/u. At a distance of 64.7 cm there is the *Margherita Start Counter* (SC) which gives the trigger signal to the entire experiment. The SC, [32] [33], is made of a thin squared foil of plastic scintillator, EJ-228, with a thickness of 250 μm and an active surface with 5 cm side that can cover the transverse size of the beam. The light generated in the scintillator is then collected laterally thanks to 48 *Silicon Photomultiplier* (SiPM) with dimension 3×3 mm^2, 12 per side, grouped in eight electronic channels. Each channel reads a chain composed of six SiPMs. The principal trigger of the experiment is given by the minimum bias trigger which is based on the signals produced by the SC. It is activated when the multiplicity of channels over thresholds is more than a given value (majority trigger). In this way the systematic errors caused by the event trigger selection are minimised. The electronic employed in the trigger function is a CAEN V2495 board, with programmable logic. The CAEN module can receive at least four logic signals arriving from the four PMTs of the detector and one signal from every detector. The trigger signal is generated when a time coincidence between two PMT signals in a gate of 20 ns is present. The internal trigger is transmitted to all detectors when all the devices are inactive and sufficient time has passed from the preceding trigger in order to conclude the cycle of the readout. The *Beam Monitor* (BM) is 2.2 cm from the SC. It is between the SC and the target in order to measure the

direction and the hitting point of the beam on the target. In this way, the events in which the fragmentation has happened in the SC creating deviated tracks, are rejected. For this reason the BM and the devices downstream the target need a very precise alignment. Then, there is the *Target* (TGT) which is made of carbon or polyethylene with a thickness equal to 0.5 or 1 cm and that is 104 cm from the BEW. After the target, there is the *Vertex Detector* (VTX) which is the tracking part of the experiment. After the VTX there is the *Microstrip Silicon Detector*, (MSD), composed by three planes active area 9.6×9.3 cm^2, separated by 2 cm gap along the beam line. It ensures the matching of the track reconstructed thanks to the hits in the *TOF Wall* (TW). The TW, at a distance of 189.4 cm from the TGT and at a distance of 297.7 cm from the BEW, consists of two layers of 20 bars of plastic scintillator which are disposed perpendicularly and wrapped with darkening black tape and reflective aluminium. The bars are 0.3 cm thick, 2 cm wide and 44 cm long. The active area of the detector is equal to 40×40 cm^2 and it provides the deposition of energy, the time of flight (TOF) with the start given by the SC, and the hit position. The detectors, *Nike 1* and *Nike 2* are respectively at 26.8 deg and 24.5 deg with respect to the beam line and they are at a distance of 235 ± 1 cm and 237 ± 1 cm from the target. The two Nike detectors work at a voltage of $1150 - 1200$ V and they have the diameter and length of 7.62 cm. They are two BC-501A liquid scintillators equivalent to NE-213 [39]. The NE-213 [40] is an aromatic molecules solution dissolved in a solvent of xylene. It is highly corrosive and flammable with the flash point at 26 °C. However, it has a high gamma-ray rejection and an excellent detection efficiency for fast neutrons. In front of every Nike there is a *veto* which is a plastic scintillator with dimension of 9×9 cm^2, a thickness of 0.5 cm, both operated at a voltage of 1200 V. The vetoes are 0.2 cm distant from each Nike and they are respectively 98.5 cm and 106 cm far from the beam line. In this way a charged particle produces a signal both in the veto and in the detector, whereas a neutral particle produces a signal only in the BC-501A [29] [32] [33]. In Figure 3.2 a simplified sketch of the FOOT setup used at GSI is shown.

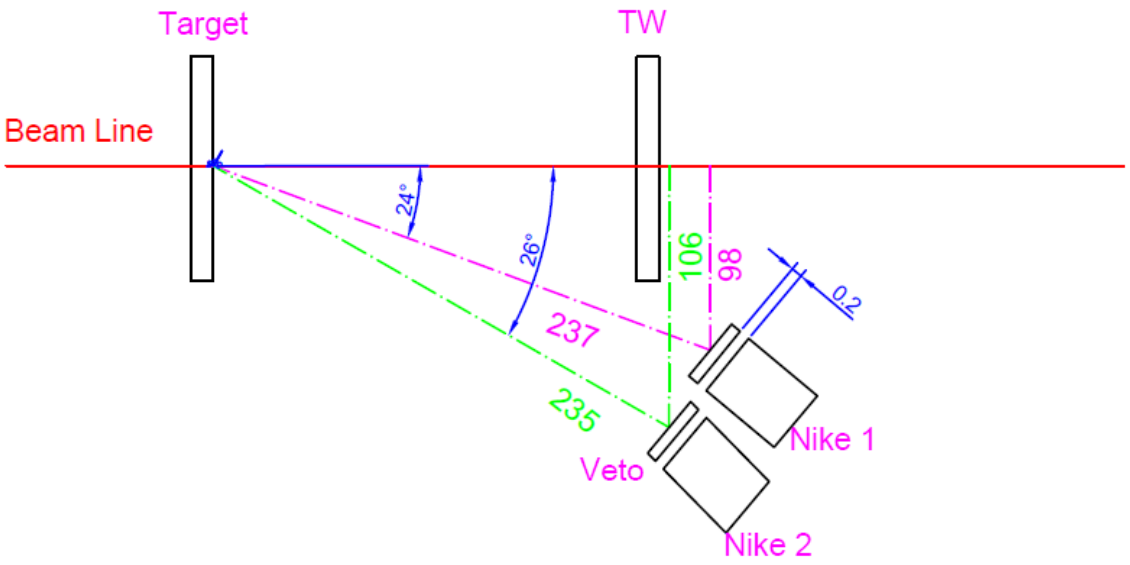

Figure 3.2: *Simplified sketch of the FOOT setup at GSI. The length measurements are in centimeters whereas the angles are reported in deg. The uncertainties are ±1 cm and ±1 deg respectively.*

3.2 Time calibration

In order to evaluate the time of flight, a calibration of the time is required. It is based on the prompt gammas produced in the interaction of the beam with the target. In fact, travelling at the speed of light c, they cover the distance, L, from the target to the detector in a TOF:

$$TOF_\gamma = \frac{L}{c}. \tag{3.1}$$

corresponding to approximately 7.84 ns in case of detector 1, L being 235 cm; and 7.91 ns in case of detector 2, where $L = 237$ cm.

Experimentally, the TOF is measured from the difference between the start signal from the SC and the stop signal from the neutron detector. Because of a time delay introduced by cables and readout electronic, the experimental TOF need to be calibrated. In fact, when the same procedure is applied to all signals, the distribution of these time of flight without the calibration is done. In Figure 3.3 one distribution of the time of flight without calibration is shown, whereas in Figure 3.4 the fit of the same curve is reported. In these figures and in the ones beyond, the events in the prominent peak are attributed to prompt gamma rays produced in the interaction of the beam with the target. On the

other hand, the counts at higher TOF are induced by neutrons and charged particles as well as gamma rays.

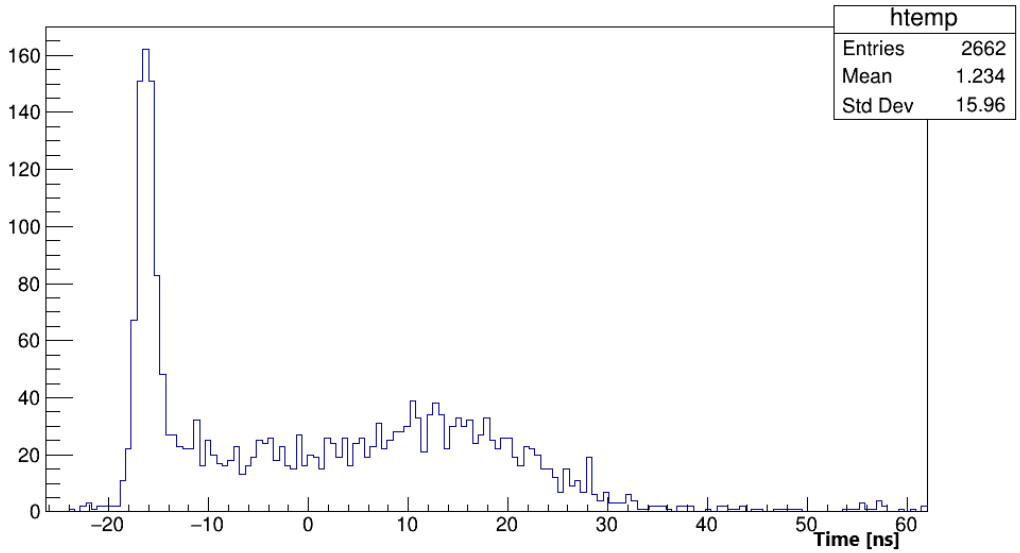

Figure 3.3: *The time-of-flight distribution before the time calibration of the detector 2. The data refer to a beam of ^{16}O of 400 MeV/u which hits against a 1 cm thick $(C_2H_4)_n$ target.*

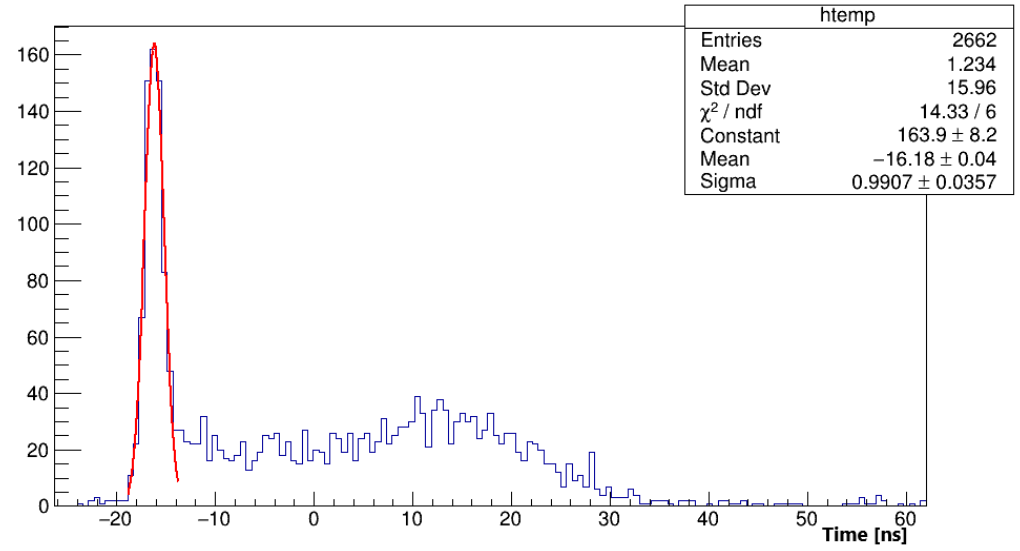

Figure 3.4: *Fit of the time-of-flight distribution before the calibration of the detector 2. The data refer to a beam of ^{16}O of 400 MeV/u which hits against a 1 cm thick $(C_2H_4)_n$ target.*

Subsequently, a Gaussian fit is applied to the peak corresponding to the prompt gamma. The value at which the gamma are picked, that is the mean value μ, does not correspond to the value calculated before. For this reason, in order to have the gamma with the peak at L/c, a translation is performed. In Table 3.1 and in Table 3.2 the values obtained from the fit are reported.

Table 3.1: *Fit values of the time of flight before the calibration for the detector 1.*

Beam energy [MeV]	Target	Target thickness [cm]	TOF Mean μ [ns]	TOF Sigma σ [ns]
400	polyethylene	1.0	-15.14 ± 0.05	0.86 ± 0.05
400	polyethylene	0.5	-15.04 ± 0.08	0.99 ± 0.08
400	carbon	0.5	-15.36 ± 0.09	0.97 ± 0.08
200	polyethylene	0.5	-12.21 ± 0.08	0.91 ± 0.09
200	carbon	0.5	-10.99 ± 0.10	0.70 ± 0.09

Table 3.2: *Fit values of the time of flight before the calibration for the detector 2.*

Beam energy [MeV]	Target	Target thickness [cm]	TOF Mean μ [ns]	TOF Sigma σ [ns]
400	polyethylene	1.0	-16.18 ± 0.04	0.99 ± 0.04
400	polyethylene	0.5	-16.42 ± 0.05	0.91 ± 0.05
400	carbon	0.5	-16.15 ± 0.07	1.00 ± 0.06
200	polyethylene	0.5	-12.85 ± 0.09	0.98 ± 0.10
200	carbon	0.5	-12.12 ± 0.08	0.86 ± 0.09

Then, on the gamma peak of the translated curve, which represents the time of flight, a new Gaussian fit is done. In Figure 3.5 and in Figure 3.6 are shown the time of flight distribution and the time of flight distribution with the fit respectively.

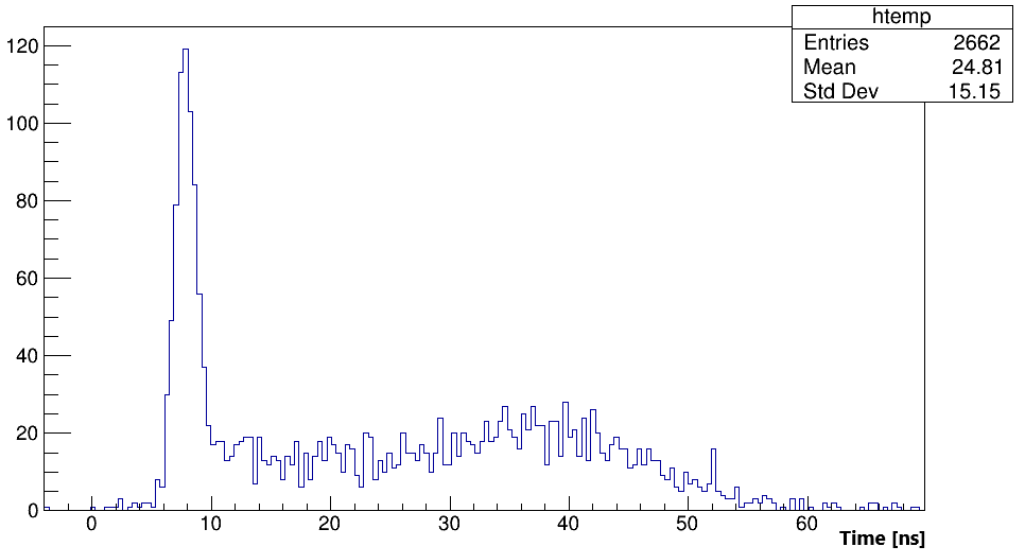

Figure 3.5: *Time-of-flight distribution of the detector 2. The data refer to a beam of ^{16}O of 400 MeV/u which hits against a 1 cm thick $(C_2H_4)_n$ target.*

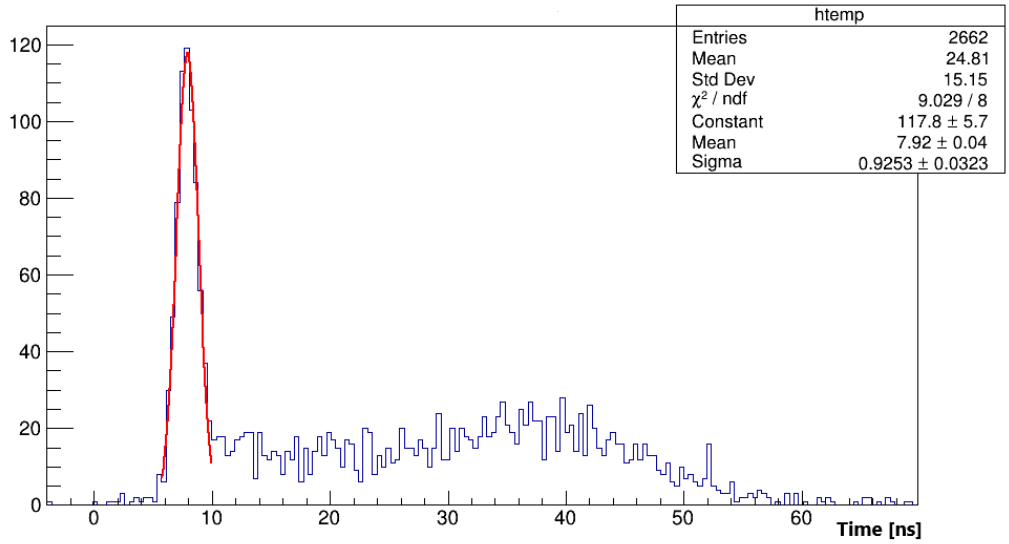

Figure 3.6: *Fit on the gamma peak of the time-of-flight distribution of the detector 2. The data refer to a beam of ^{16}O of 400 MeV/u which hits against a 1 cm thick $(C_2H_4)_n$ target.*

After applying the time calibration, the mean value of the fit represents the TOF of the prompt gamma. In Table 3.3 and in Table 3.4 the values obtained from the fit are

shown. The procedure is applied to all of files.

Table 3.3: *The time-of-flight after time calibration for the detector 1.*

Beam energy [MeV]	Target	Target thickness [cm]	TOF Mean μ [ns]	TOF Sigma σ [ns]
400	polyethylene	1.0	7.90 ± 0.05	0.92 ± 0.05
400	polyethylene	0.5	7.83 ± 0.09	1.00 ± 0.10
400	carbon	0.5	7.57 ± 0.20	0.98 ± 0.20
200	polyethylene	0.5	7.95 ± 0.10	0.92 ± 0.10
200	carbon	0.5	7.49 ± 0.20	1.13 ± 0.30

Table 3.4: *The time-of-flight after time calibration for the detector 2.*

Beam energy [MeV]	Target	Target thickness [cm]	TOF Mean μ [ns]	TOF Sigma σ [ns]
400	polyethylene	1.0	7.92 ± 0.04	0.93 ± 0.03
400	polyethylene	0.5	7.99 ± 0.05	0.99 ± 0.05
400	carbon	0.5	7.86 ± 0.07	0.98 ± 0.07
200	polyethylene	0.5	7.81 ± 0.08	0.94 ± 0.08
200	carbon	0.5	7.96 ± 0.08	0.95 ± 0.09

3.3 Pulse shape discrimination

In order to discriminate particles the *pulse shape discrimination* (PSD) technique is used in this analysis. To apply it, scintillators whose light emission has a fast and a slow decay components with a strong dependence on the dE/dx are employed. Usually, scintillators with this characteristic are the organic ones, in particular the liquid scintillators. In fact, most of them have the scintillation light which is given by the prompt fluorescence, but sometimes there could be also a longer-lived component that is the phosphorescence. The light-yield curve is so obtained by the sum of these two exponential functions, the fast and the slow one, that represent the two decays. The fast component has a prompt decay time of the order of nanoseconds, whereas the slow one has a decay time of the order of several tens or hundreds of nanoseconds. Most of the light yield takes place in the prompt component, but the delayed one can be used to distinguish different particles. In this way, it is possible to distinguish different incident particles by analyzing the shape of the pulse of the emitted light. Regarding the neutron and gamma discrimination, their pulse shapes with the respective integrals are taken into account as it is shown in Figure 3.7, retrieved from literature [17]. Then, a measurement of the time between the beginning of the pulse and the point in which the pulse integral has reached a given value is done. In this way, diverse pulse shapes will have different time measurements.

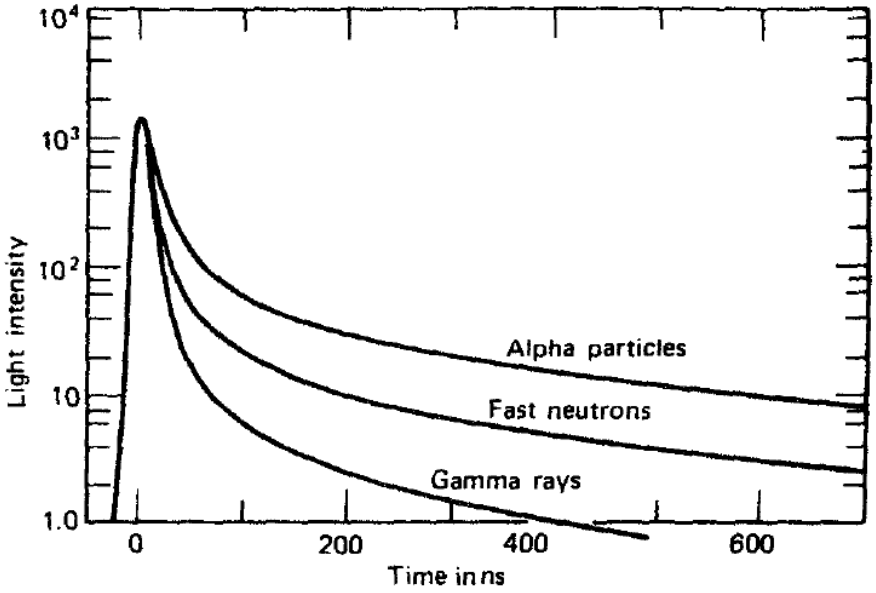

Figure 3.7: *Pulse shapes of alpha particles, fast neutrons and gamma rays as a function of time. In this figure taken from the literature, the scintillator is made of stilbene* [17].

3.4 Particles discrimination

The first discrimination among particles is done by selecting the charged and the uncharged ones. The charged particles will give signal both in the veto and in the neutron detector, whereas the neutral ones will give signal only in the detector and not in the veto as it was mentioned in section 3.1. In order to do this, two boolean functions called *Is_On* and *Is_Coinc* are constructed. The first one identifies whether the detector was hit or not, whereas the latter one provides the information about the coincidence between the veto and the detector. For charged particles the detector has to be on and the coincidence between veto and detector must be present, whereas for neutral particles the detector has to be on but the coincidence between veto and detector must not occur. This discrimination is done both for detector 1 and detector 2, and coincidences and anticoincidences events are sorted. Table 3.5 and Table 3.6 report the number of coincidence and ainticoincidence events in detector 1 and in detector 2, respectively.

Table 3.5: *Number of coincidence and anticoincidence events in detector 1.*

Beam energy [MeV]	Target	Target thickness [cm]	Number coincidence events	Number anticoincidence events
400	polyethylene	1.0	329	1302
400	polyethylene	0.5	153	847
400	carbon	0.5	112	481
200	polyethylene	0.5	459	658
200	carbon	0.5	417	350

Table 3.6: *Number of coincidence and anticoincidence events in detector 2.*

Beam energy [MeV]	Target	Target thickness [cm]	Number coincidence events	Number anticoincidence events
400	polyethylene	1.0	466	2662
400	polyethylene	0.5	251	1835
400	carbon	0.5	160	952
200	polyethylene	0.5	548	1435
200	carbon	0.5	475	767

Subsequently, the signals of the detectors 1 and 2 for signals in anticoincidence with the veto and the signals of the detectors 1 and 2 for signals in coincidence with the veto are plotted and they are shown in Figure 3.8, Figure 3.9, Figure 3.10 and Figure 3.11 respectively. In Figure 3.12 and in Figure 3.13, instead, the signal on the first and second veto are reported, which are faster than the ones of the two detectors.

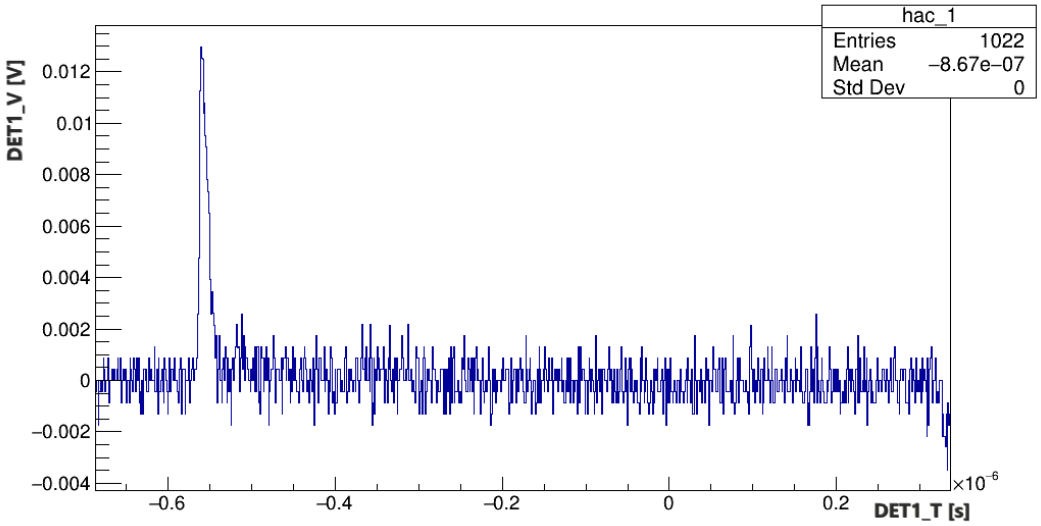

Figure 3.8: *Signal of the first BC-501A for signals in anticoincidence with the veto detector (i.e. gamma-rays and neutrons). The data refer to a beam of ^{16}O of 400 MeV/u which hits against a 1 cm thick $(C_2H_4)_n$ target.*

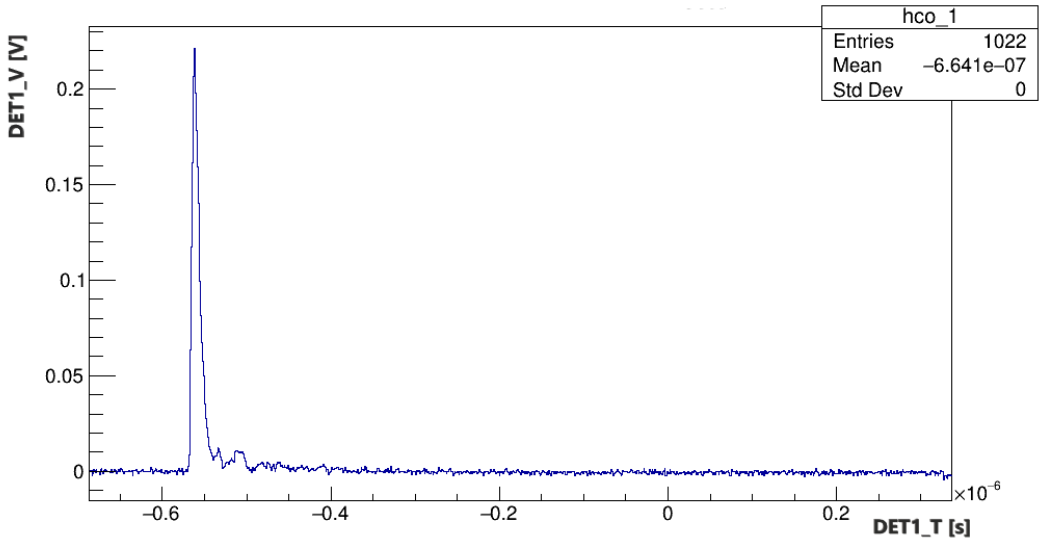

Figure 3.9: *Signal of the first BC-501A for signals in coincidence with the veto detector (i.e. charged particles). The data refer to a beam of ^{16}O of 400 MeV/u which hits against a 1 cm thick $(C_2H_4)_n$ target.*

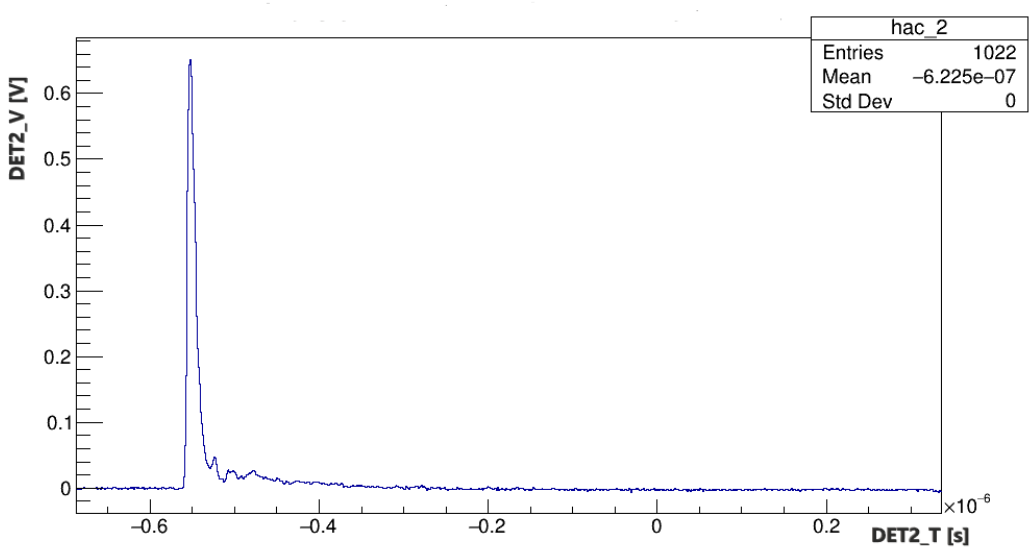

Figure 3.10: *Signal of the second BC-501A for signals in anticoincidence with the veto detector (i.e. gamma-rays and neutrons). The data refer to a beam of ^{16}O of 400 MeV/u which hits against a 1 cm thick $(C_2H_4)_n$ target.*

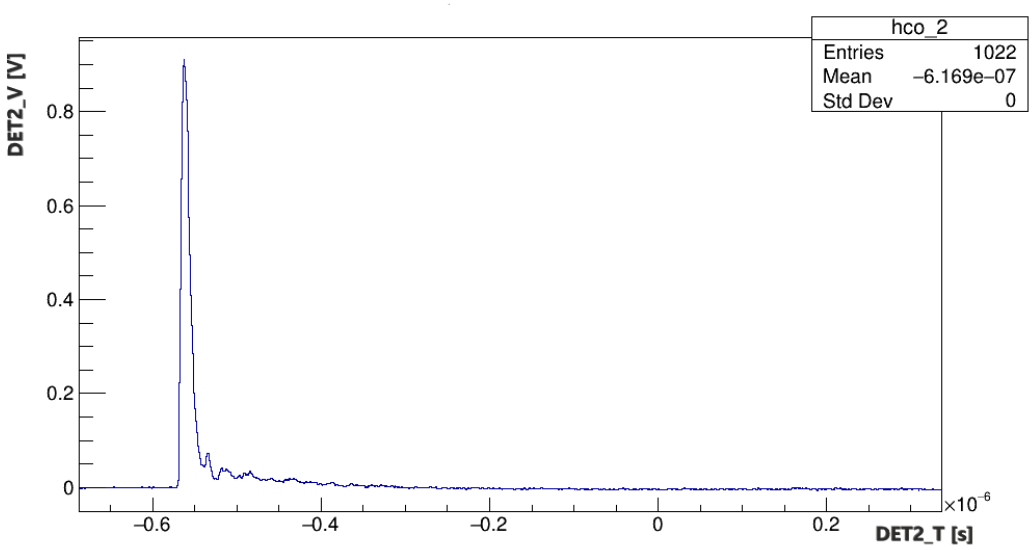

Figure 3.11: *Signal of the second BC-501A for signals in coincidence with the veto detector (i.e. charged particles). The data refer to a beam of ^{16}O of 400 MeV/u which hits against a 1 cm thick $(C_2H_4)_n$ target.*

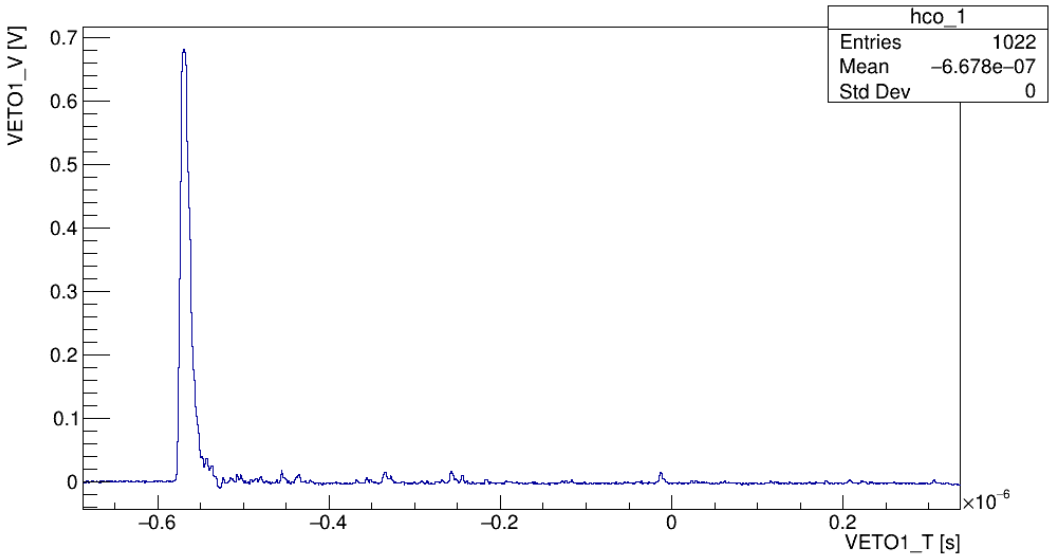

Figure 3.12: *Signal of the first veto detector. The data refer to a beam of* ^{16}O *of* 400 MeV/u *which hits against a* 1 *cm thick* $(C_2H_4)_n$ *target.*

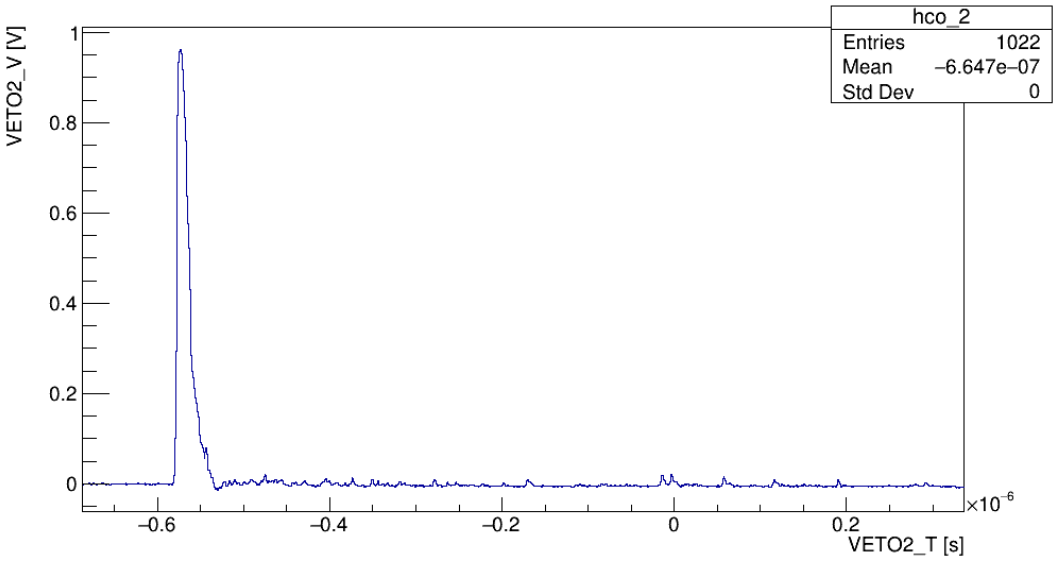

Figure 3.13: *Signal of the second veto detector. The data refer to a beam of* ^{16}O *of* 400 MeV/u *which hits against a* 1 *cm thick* $(C_2H_4)_n$ *target.*

Then, for each signal the amplitude is extracted and reported in a plot. In Figure 3.14, Figure 3.15, Figure 3.16, Figure 3.17 the spectra are shown.

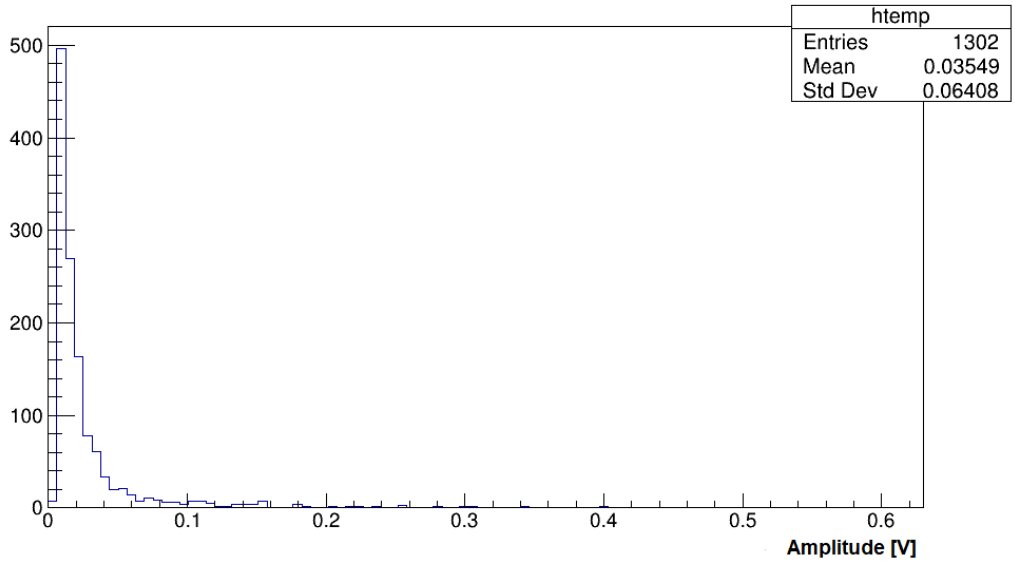

Figure 3.14: *Amplitude spectrum of the first BC-501A for signals in anticoincidence with the veto detector (i.e. gamma-rays and neutrons). The data refer to a beam of ^{16}O of 400 MeV/u which hits against a 1 cm thick $(C_2H_4)_n$ target.*

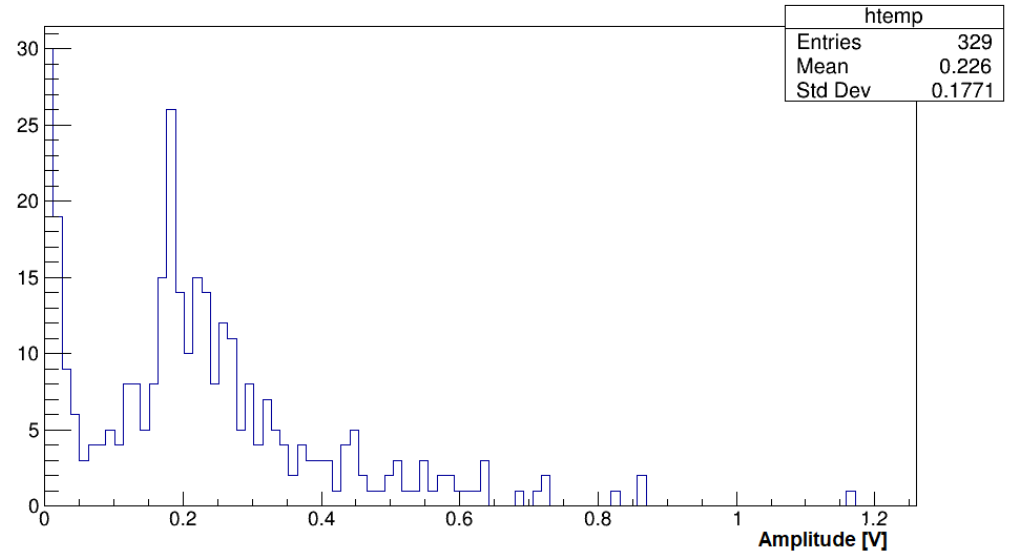

Figure 3.15: *Amplitude spectrum of the first BC-501A for signals in coincidence with the veto detector (i.e. charged particles). The data refer to a beam of ^{16}O of 400 MeV/u which hits against a 1 cm thick $(C_2H_4)_n$ target.*

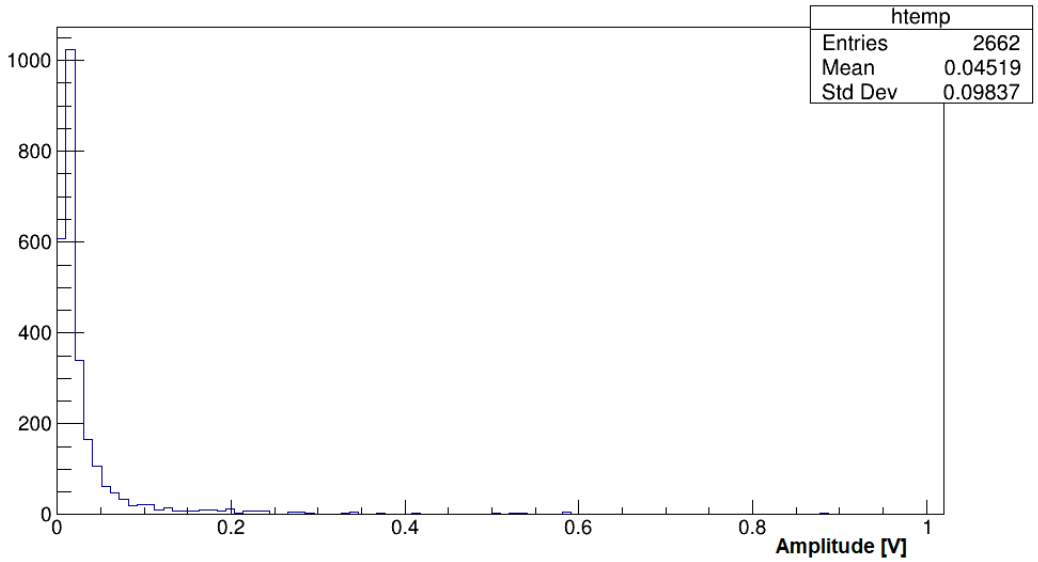

Figure 3.16: *Amplitude spectrum of the second BC-501A for signals in anticoincidence with the veto detector (i.e. gamma-rays and neutrons). The data refer to a beam of ^{16}O of 400 MeV/u which hits against a 1 cm thick $(C_2H_4)_n$ target.*

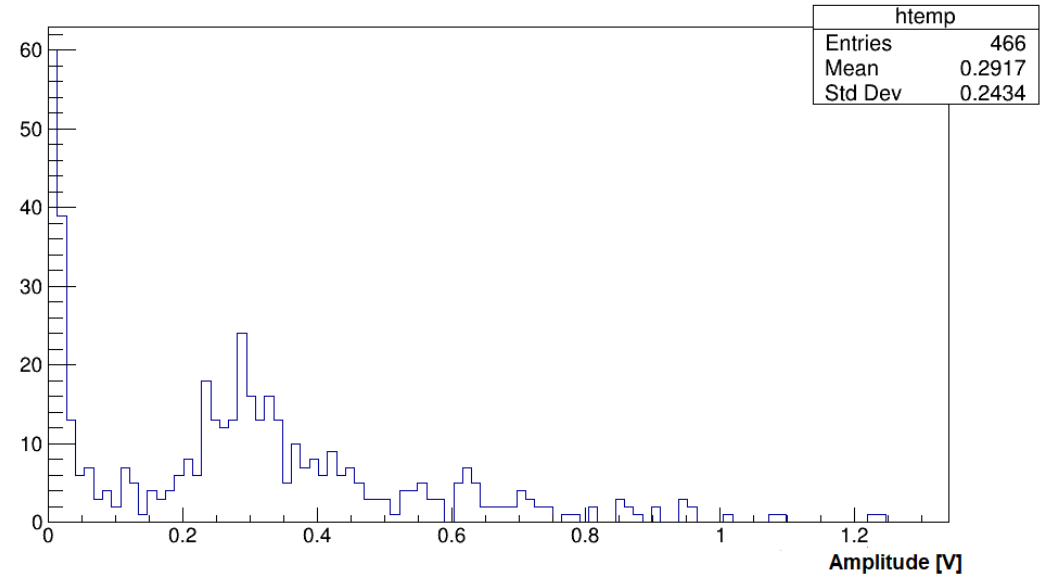

Figure 3.17: *Amplitude spectrum of the second BC-501A for signals in coincidence with the veto detector (i.e. charged particles). The data refer to a beam of ^{16}O of 400 MeV/u which hits against a 1 cm thick $(C_2H_4)_n$ target.*

In addition, the time at which the signal is at the 80%, 30% and 20% of the maximum are computed together with the first time the signal goes to zero after the peak. They are respectively called *t80*, *t30*, *t20* and *t0*. From these values the *signal duration* and the *rise time* are computed, they are given by the difference between *t0*, *t20* and *t80*, *t20*, respectively. The distribution of the signal duration is reported in Figure 3.18 whereas the rise time is shown in Figure 3.19.

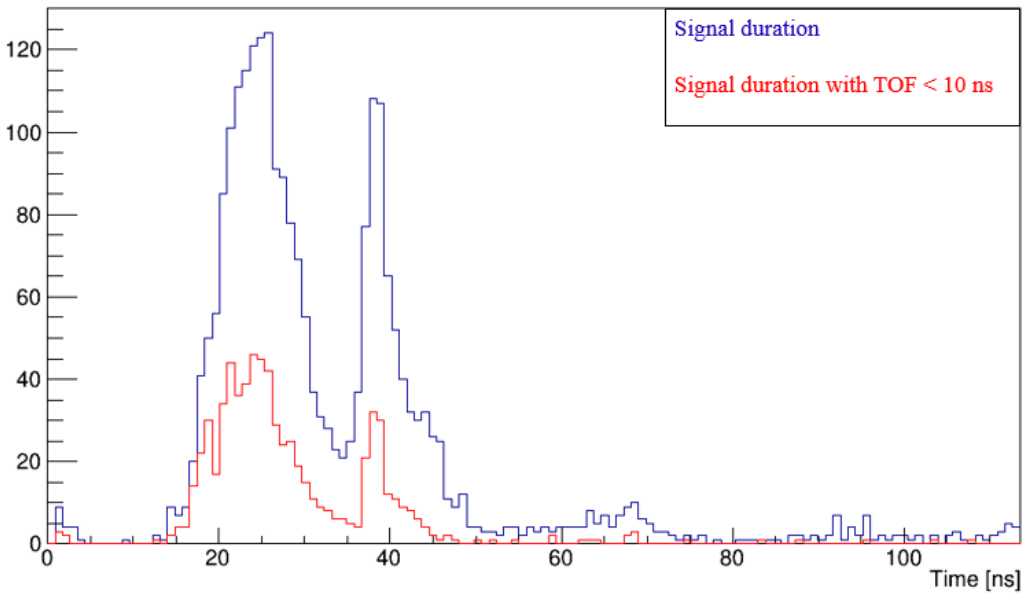

Figure 3.18: *Pulse duration of the second BC-501A for signals in anticoincidence with the veto detector (i.e. gamma-rays and neutrons). The blue distribution represents the signal duration of the all neutral particles whereas the red one stands for the events with the TOF* < 10 *ns (i.e. gamma-rays). The distribution in blue seems to show two data groups, possibly gammas and neutrons with different time. The distribution in red, however, shows that gamma rays are present in both the two data groups. So, this two different times are possibly due to the acquisition system. The data refer to a beam of* ^{16}O *of* 400 MeV/u *which hits against a* 1 *cm thick* $(C_2H_4)_n$ *target.*

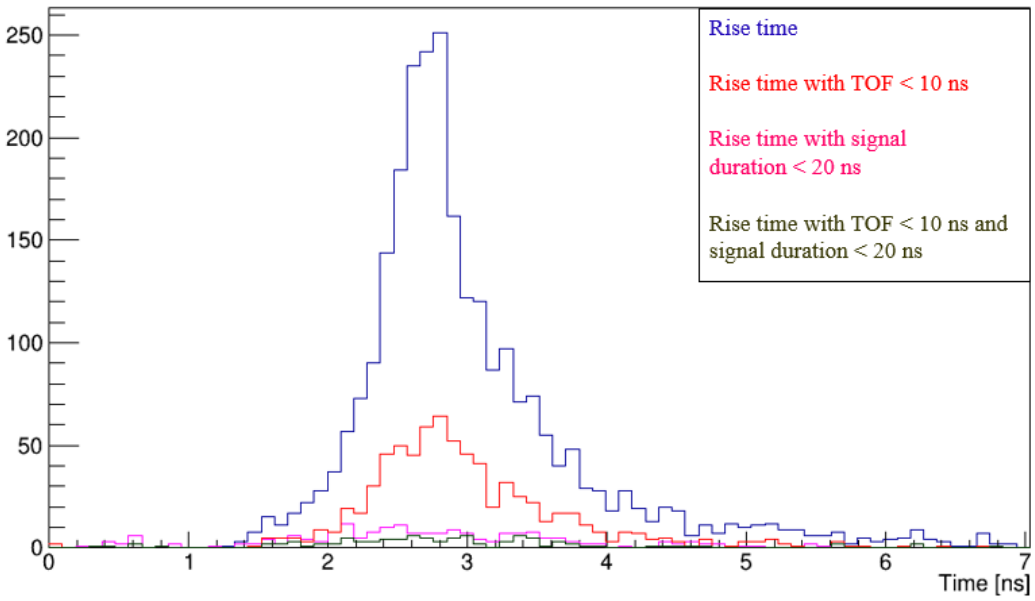

Figure 3.19: *Rise time of the second BC-501A for signals in anticoincidence with the veto detector (i.e. gamma-rays and neutrons). The distribution in blue represents the rise time of all neutral particles, whereas the red one and the magenta one stand for the rise time for the events with the TOF* < 10 *ns (i.e. the gamma-rays) and the signal duration* < 20 *ns, respectively. The distribution in dark green is the rise time for the events with both the TOF* < 10 *ns and the signal duration* < 20 *ns. The data refer to a beam of* ^{16}O *of* 400 MeV/u *which hits against a* 1 *cm thick* $(C_2H_4)_n$ *target.*

In order to discriminate between neutrons and photons it is necessary to separate the fast part of the signal which is called *area fast* and the slow component, that is called *area slow*. The area fast is constructed by taking the area of the signal from the rising edge to the time corresponding to 20% of the maximum after the peak itself. The area slow, instead, is obtained by taking the area of the signal from 20% of the maximum after the peak to the value of *t0*. The plots of the two areas are represented in Figure 3.20 and in Figure 3.21 respectively.

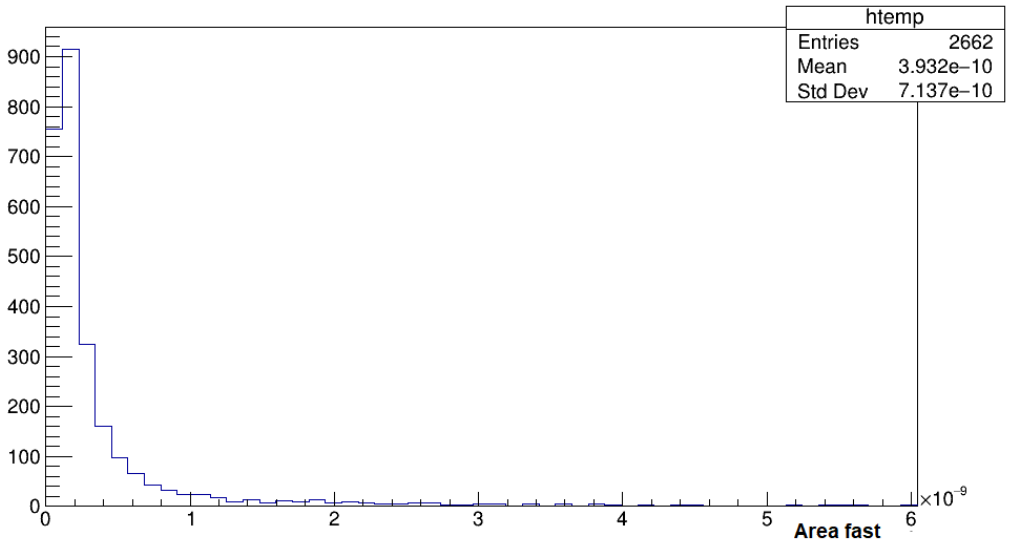

Figure 3.20: *Area fast of the second BC-501A for signals in anticoincidence with the veto detector (i.e. gamma-rays and neutrons). The data refer to a beam of ^{16}O of 400 MeV/u which hits against a 1 cm thick $(C_2H_4)_n$ target.*

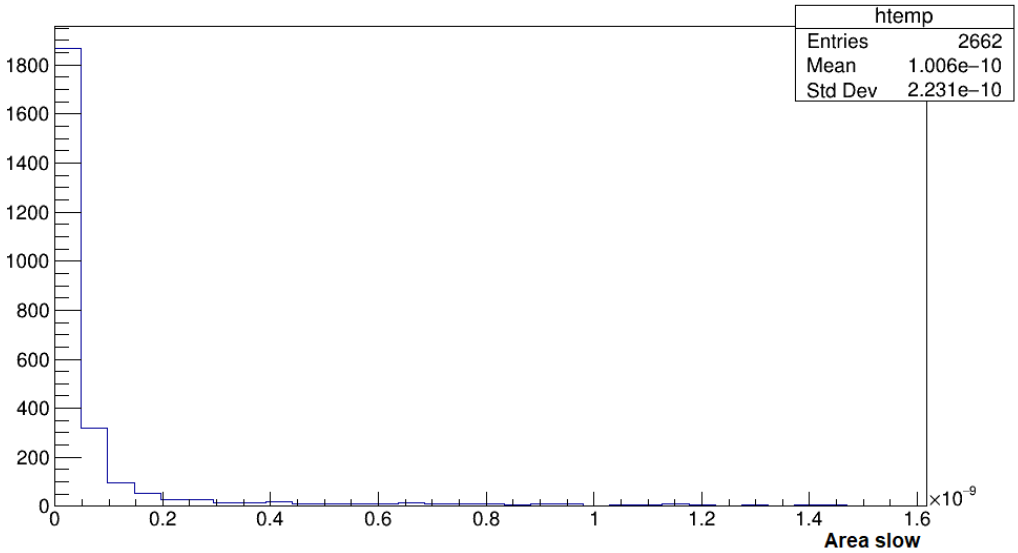

Figure 3.21: *Area slow of the second BC-501A for signals in anticoincidence with the veto detector (i.e. gamma-rays and neutrons). The data refer to a beam of ^{16}O of 400 MeV/u which hits against a 1 cm thick $(C_2H_4)_n$ target.*

All these studies are performed to find the better discrimination between neutrons

and gamma-rays. In particular, the selection is performed by imposing three cuts, one on the amplitude, another one on the TOF and the last one on the ratio between the area slow and the total area which is calculated by adding the area fast and the area slow. In Figure 3.22 the ratio between the two areas as function of amplitude is shown.

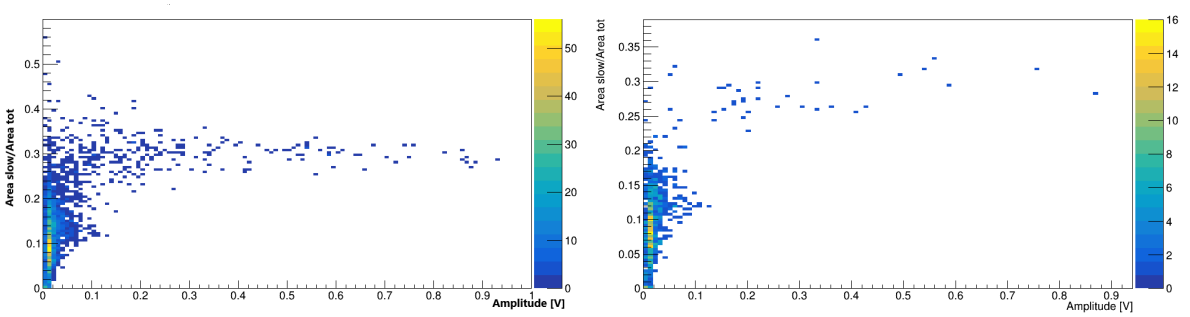

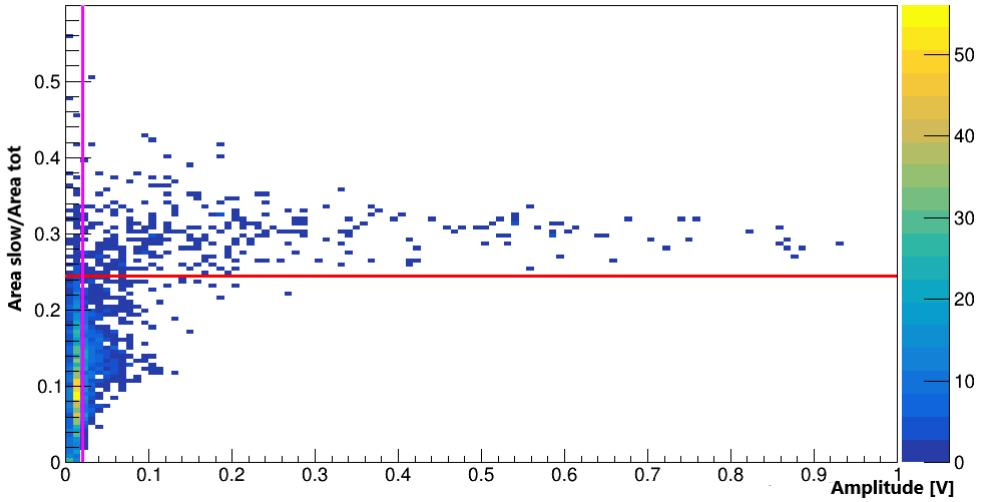

Figure 3.22: *The top panel shows, on the left sight, the Area slow/Area tot as function of amplitude on the second BC-501A for signals in anticoincidence with the veto detector (i.e. gamma-rays and neutrons), whereas, on the right sight, the Area slow/Area tot as function of amplitude for the events with TOF* < 10 *ns on the second BC-501A for signals in anticoincidence with the veto detector (i.e. gamma-rays). The plot below both the analysis selections made on Area slow/Area tot and amplitude are shown: the red line represents the Area slow/Area tot selection, while the magenta line represents the threshold on the amplitude. The neutrons are identified in the region where Area slow/Area tot* > 0.245 *and Amplitude* > 0.02*. The data refer to a beam of* ^{16}O *of* 400 *MeV/u which hits against a* 1 *cm thick* $(C_2H_4)_n$ *target.*

So, the analysis condition on the amplitude is Amplitude > 0.02 V and the analysis selection on the time-of-flight is TOF $> \mu + 2\sigma$ in which the values of μ and σ are reported in Table 3.3 and in Table 3.4. The values of the analysis condition found on the TOF are reported in Table 3.7 for what concern the detector 1 and in Table 3.8 for detector 2.

Table 3.7: *Analysis condition on the TOF for the detector 1.*

Beam energy [MeV]	Target	Target thickness [cm]	TOF [ns]
400	polyethylene	1.0	9.73
400	polyethylene	0.5	9.84
400	carbon	0.5	9.52
200	polyethylene	0.5	9.78
200	carbon	0.5	9.75

Table 3.8: *Analysis selection on the TOF for the detector 2.*

Beam energy [MeV]	Target	Target thickness [cm]	TOF [ns]
400	polyethylene	1.0	9.77
400	polyethylene	0.5	9.99
400	carbon	0.5	9.81
200	polyethylene	0.5	9.69
200	carbon	0.5	9.85

Once the conditions on the amplitude and on the TOF are applied, the distribution of the ratio between the area slow and the total area is constructed. This plot is shown in Figure 3.23 whereas in Table 3.9 and in Table 3.10 the values of the cuts on the area, which are taken when there is the separation between the two peaks, are reported respectively for detector 1 and detector 2.

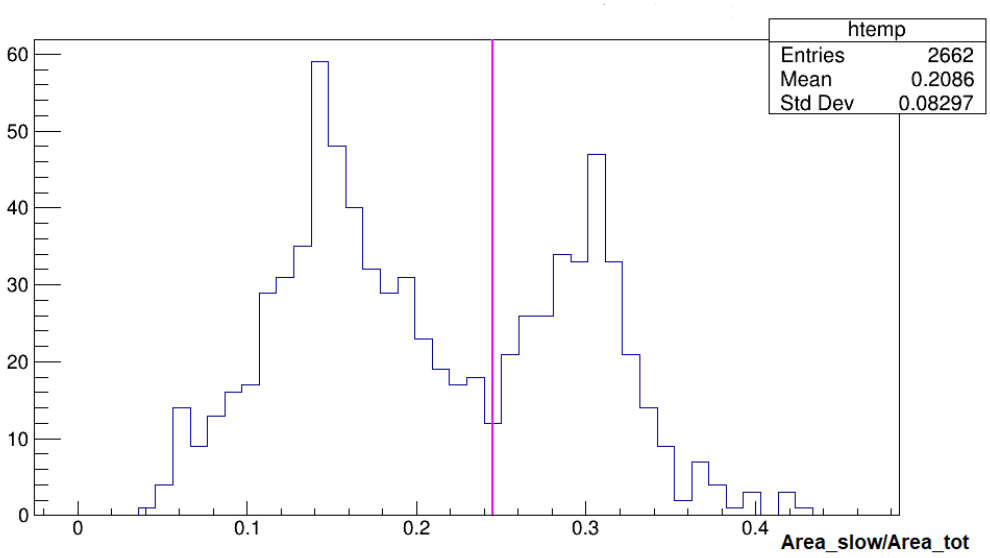

Figure 3.23: *Distribution of the ratio between the area slow of a pulse and its total component. The data refer to a beam of ^{16}O of 400 MeV/ which hits against a 1 cm thick $(C_2H_4)_n$ target.*

So, the ratio between the areas has to be more than the values found in Table 3.9 and in Table 3.10.

Table 3.9: *Condition on the area for the detector 1.*

Beam energy [MeV]	Target	Target thickness [cm]	Area slow/Area total
400	polyethylene	1.0	0.179
400	polyethylene	0.5	0.178
400	carbon	0.5	0.172
200	polyethylene	0.5	0.189
200	carbon	0.5	0.195

Table 3.10: *Condition on the area for the detector 2.*

Beam energy [MeV]	Target	Target thickness [cm]	Area slow/Area total
400	polyethylene	1.0	0.245
400	polyethylene	0.5	0.235
400	carbon	0.5	0.220
200	polyethylene	0.5	0.184
200	carbon	0.5	0.221

In the end, in Figure 3.24 and in Figure 3.25, the two amplitude spectra for neutrons and photons, when only the cut on the TOF is applied, are shown.

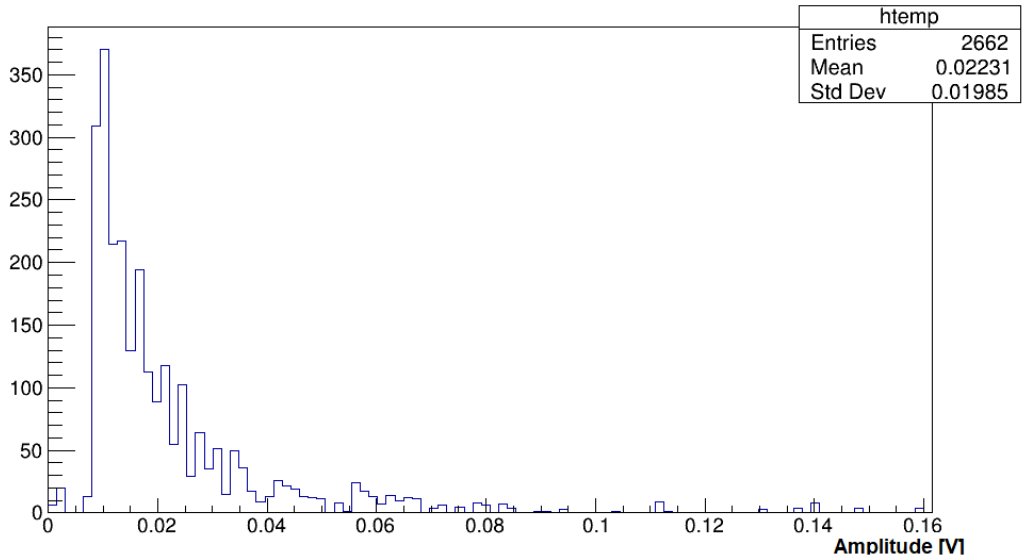

Figure 3.24: *Amplitude spectrum of the photons. The data refer to a beam of* ^{16}O *of* 400 *MeV/u which hits against a* 1 *cm thick* $(C_2H_4)_n$ *target.*

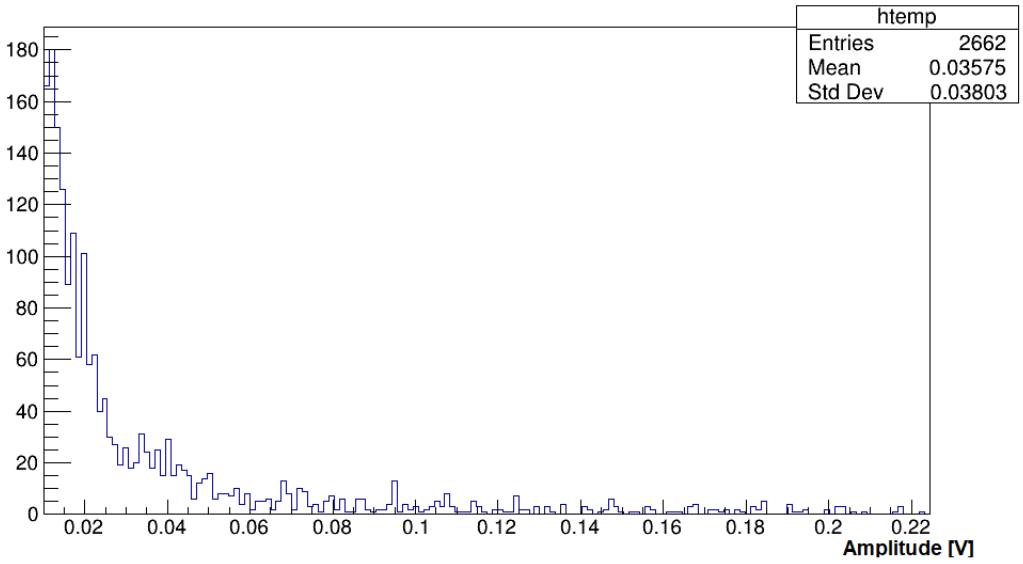

Figure 3.25: *Amplitude spectrum of the neutrons. The data refer to a beam of* ^{16}O *of* 400 *MeV/u which hits against a* 1 *cm thick* $(C_2H_4)_n$ *target.*

3.5 Kinetic energy spectra of neutrons

The kinetic energy of all neutral particles is found thanks to the following expression

$$E = m\,(\gamma - 1)\,, \tag{3.2}$$

in which m is the neutron mass, 939.565 MeV/c^2 [41], and the factor γ is given by:

$$\gamma = \frac{1}{\sqrt{1-\beta^2}}, \tag{3.3}$$

where β is the ratio between the particle velocity, v, and the velocity of light. The particle velocity is calculated as the ratio between the target-detector distance and the TOF. The same procedure is used in order to find the neutrons energy after the analysis conditions are applied on signal amplitude, TOF, and the areas ratio. In Figure 3.26 and in Figure 3.27 the energy plots on detector 1 and detector 2 are shown.

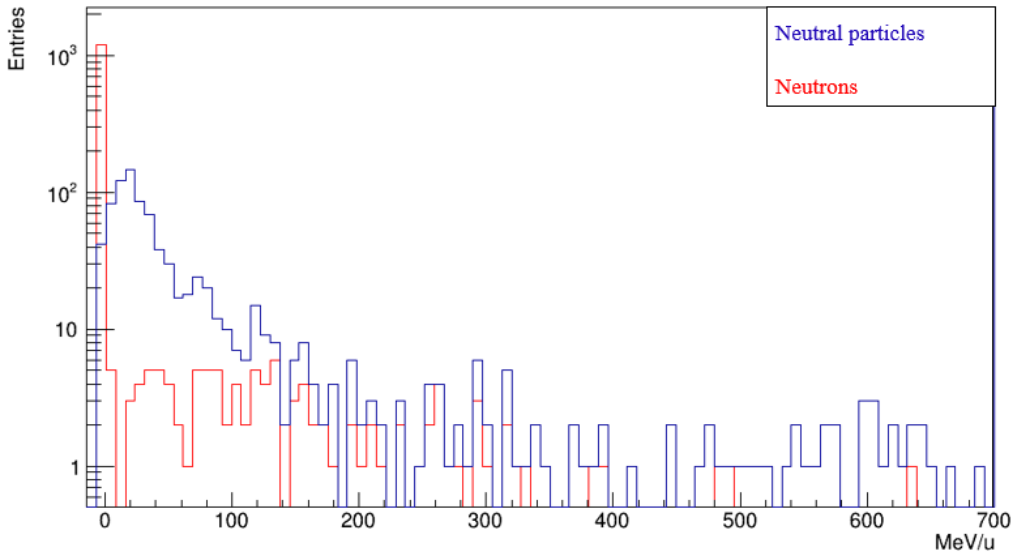

Figure 3.26: *Energy spectrum on detector 1 in logarithmic scale. The blue distribution represents all the neutral particles, while the red one stands for the neutrons. The data refer to a beam of ^{16}O of 400 MeV/u which hits against a 1 cm thick $(C_2H_4)_n$ target.*

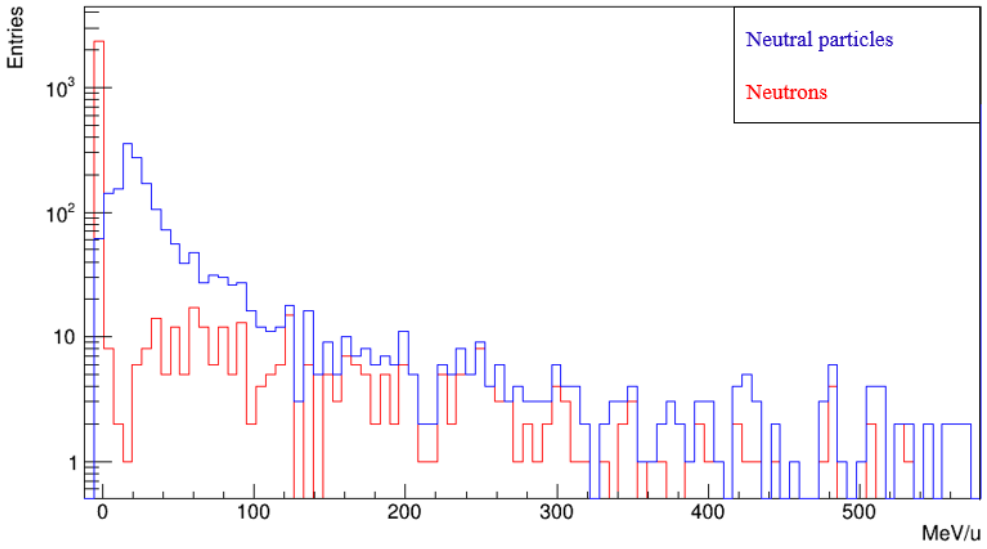

Figure 3.27: *Energy spectrum on detector 2 in logarithmic scale. The blue distribution represents all the neutral particles, while the red one stands for the neutrons. The data refer to a beam of* ^{16}O *of* 400 MeV/u *which hits against a* 1 *cm thick* $(C_2H_4)_n$ *target.*

Since neutron energy can not be greater than 400 MeV/u, the events with energies above this value are due to background events or to not optimal discrimination.
In Figure 3.28 the prompt photons amplitude is shown. From this spectrum it is possible to deduce that the threshold corresponds to few MeV as it is in the efficiency curve.

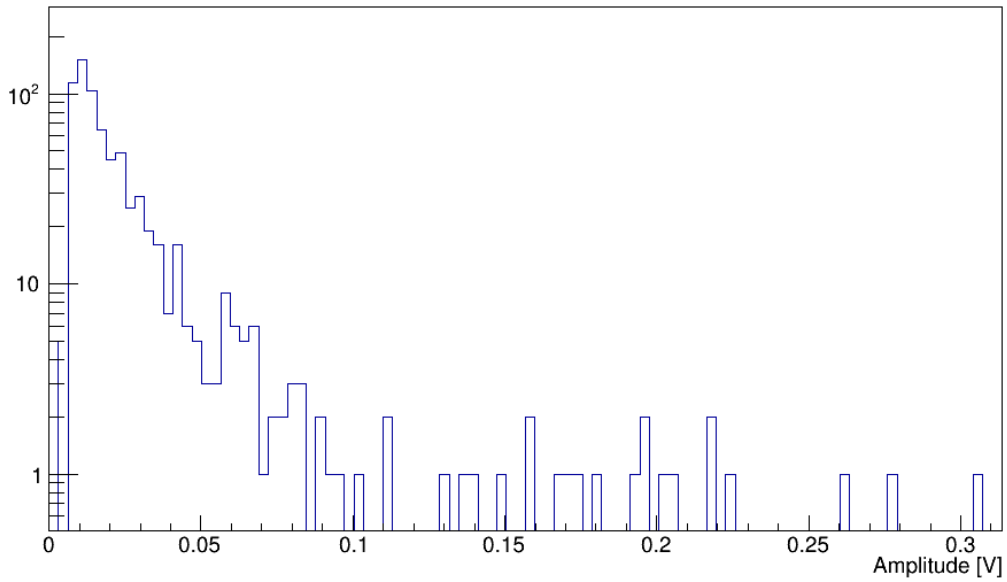

Figure 3.28: *Prompt photons amplitude on detector 2 in logarithmic scale. The data refer to a beam of ^{16}O of 400 MeV/u which hits against a 1 cm thick $(C_2H_4)_n$ target.*

3.6 Differential cross sections of neutrons

The cross section is calculated thanks to the formula:

$$\frac{d\sigma}{dE} = \frac{N_n}{N_p \Omega \mathcal{E} w N_{cs}} \tag{3.4}$$

In this formula, N_n corresponds to the number of neutrons detected by detector 1 and detector 2, which are reported in Table 3.11 and in Table 3.12 respectively.

Table 3.11: *Number of neutrons on detector 1.*

Beam energy [MeV]	Target	Target thickness [cm]	Number of neutrons
400	polyethylene	1.0	112
400	polyethylene	0.5	73
400	carbon	0.5	44
200	polyethylene	0.5	50
200	carbon	0.5	17

Table 3.12: *Number of neutrons on detector 2.*

Beam energy [MeV]	Target	Target thickness [cm]	Number of neutrons
400	polyethylene	1.0	294
400	polyethylene	0.5	249
400	carbon	0.5	120
200	polyethylene	0.5	191
200	carbon	0.5	79

The number of primaries, N_p, instead, is shown in Table 3.13.

Table 3.13: *Number of primaries.*

Beam energy [MeV]	Target	Target thickness [cm]	Number of primaries
400	polyethylene	1.0	3465891
400	polyethylene	0.5	2197839
400	carbon	0.5	1252568
200	polyethylene	0.5	12184634
200	carbon	0.5	8227337

The solid angle, Ω, being:

$$\Omega = \frac{A}{d^2} \tag{3.5}$$

in which A is the detector area that is equal to $A = \pi r^2$ with $r = 3.8$ cm and d is the distance between the target and the detector. The solid angle is a fixed value which is of the order of 0.82 msr for detector 1 and 0.81 msr for detector 2.

The number of scattering centers, N_{cs}, is found thanks to the following expression

$$N_{cs} = \frac{\rho d}{MM} N_A \tag{3.6}$$

where ρ is the material density which is equal to 1.83 g/cm^3 for carbon and to 0.94 g/cm^3 for polyethylene; d stands for the target thickness; N_A is the Avogadro's number that is $6.022 * 10^{23}$ mol^{-1}; MM represents the molar mass of carbon, 12.01 g/mol, and the molar mass of the monomer unity of the polyethylene, 28.053 g/mol.

The efficiency of the detector, instead, is simulated. In Figure 3.29 the fitted efficiency curves of BC-720 and BC-501A detectors are reported with the thresholds at 1 MeV and 3 MeV.

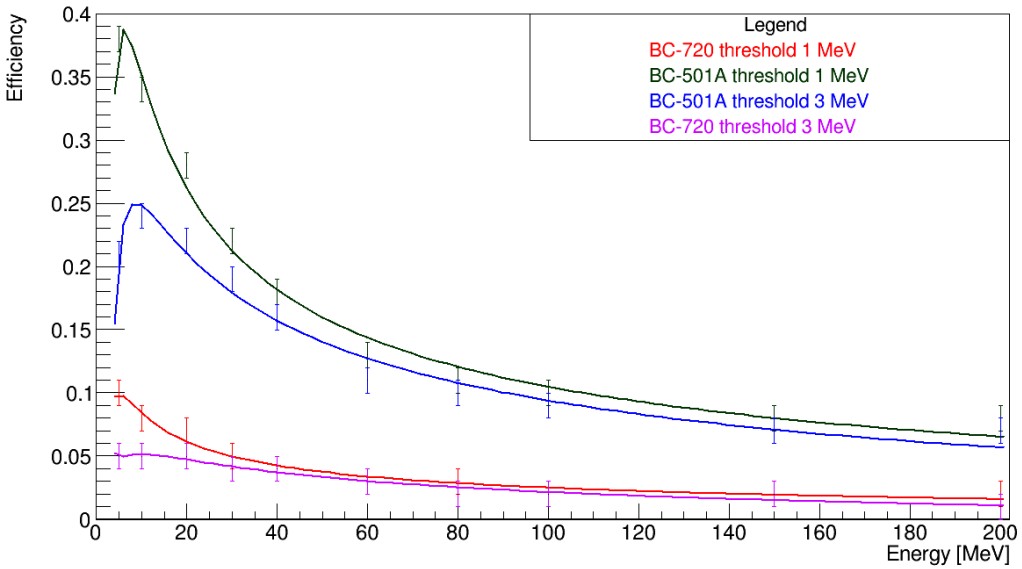

Figure 3.29: *Efficiency simulation of detectors BC-501A and BC-720 with threshold* 1 MeV/u *and* 3 MeV/u.

The curves are fitted with the following function:

$$\mathcal{E}(E) = \frac{a}{\sqrt{E}} + \frac{b}{E} + \frac{c}{\sqrt{E^3}} + \frac{d}{E^2} + e \tag{3.7}$$

whose parameters values are shown in Table 3.14.

Table 3.14: *Values of the fitted parameters of the efficiency curves regarding the BC-501A and BC-720 detector with threshold of* 1 *MeV/u and* 3 *MeV/u.*

BC-720 threshold 1 MeV/u	
Parameter	Fitted value
a	1.3571 ± 0.1000
b	0.0186 ± 0.5000
c	0.0186 ± 0.5000
d	-5.1299 ± 1.0000
e	-0.0307 ± 0.0100
BC-501A threshold 1 MeV/u	
Parameter	Fitted value
a	0.3115 ± 0.1000
b	0.0009 ± 0.5000
c	0.0009 ± 0.5000
d	-0.8516 ± 1.0000
e	-0.0061 ± 0.0100
BC-720 threshold 3 MeV/u	
Parameter	Fitted value
a	1.6062 ± 0.1486
b	-0.9731 ± 0.5274
c	-0.9731 ± 0.5274
d	-1.8286 ± 1.3556
e	-0.0471 ± 0.0120
BC-501A threshold 3 MeV/u	
Parameter	Fitted value
a	0.5570 ± 0.1486
b	-0.5790 ± 0.5274
c	-0.5790 ± 0.5274
d	1.3790 ± 1.3556
e	-0.0228 ± 0.0120

In the end, the cross sections on detector 2 is reported in Figure 3.30.

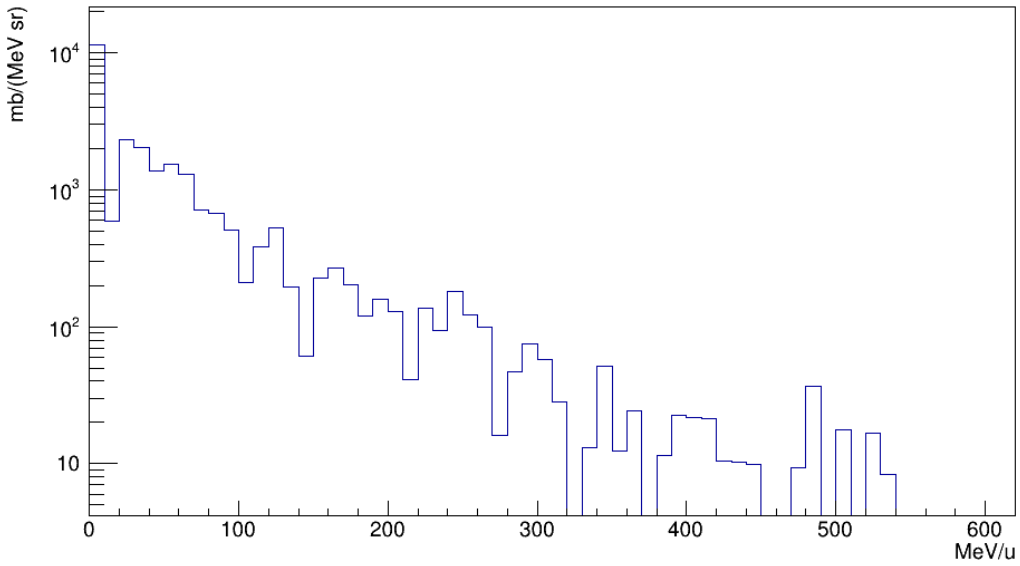

Figure 3.30: *Neutrons cross section on detector 2 as function of energy in logarithmic scale. The BC-501A threshold is* 3 *MeV/u and the data refer to a beam of* ^{16}O *of* 400 *MeV/u which hits against a* 1 *cm thick* $(C_2H_4)_n$ *target.*

3.7 Results and discussion

The procedure described before is performed on all the data sets and the energy-differential cross section for neutrons production in the reactions $^{16}\mathrm{O} + (\mathrm{C_2H_4})_n$ and $^{16}\mathrm{O} + \mathrm{C}$ are calculated. In Figure 3.31 and in Figure 3.32 the energy-differential cross section as a function of energy is shown for an oxygen beam at 200 MeV that hits against a 0.5 cm thick target of carbon and polyethylene respectively. The behaviour of the curves is similar: they have a peak at low energy which goes to zero with increasing energy.

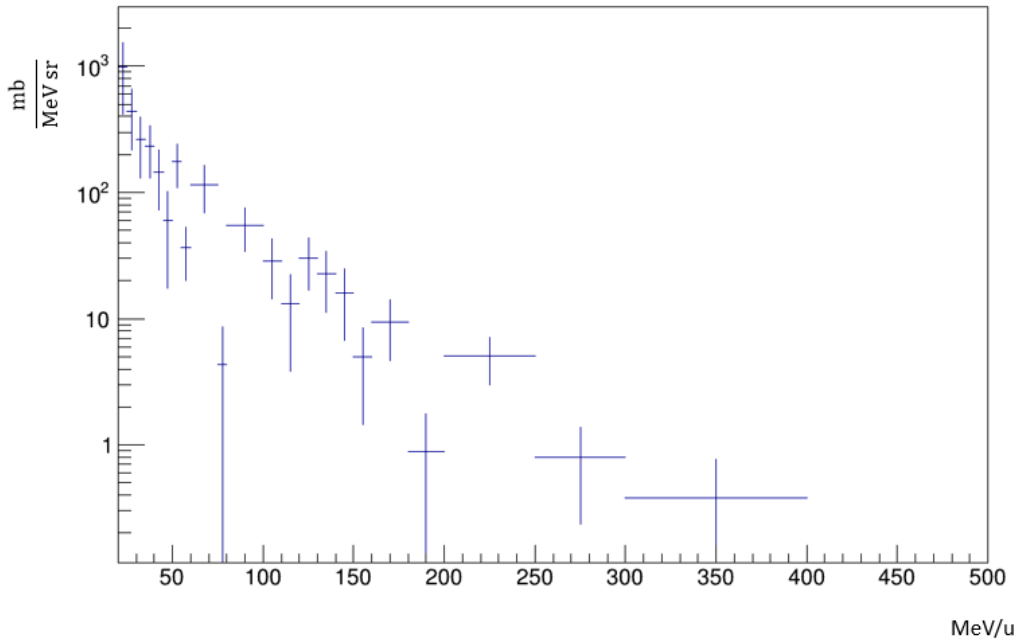

Figure 3.31: *Energy-differential cross section on detector 2 as a function of energy in logarithmic scale. The error on the energy is equal to the bin width, whereas the error associated to the cross section is given by* $\sigma\frac{1}{\sqrt{N}}$ *where N represents the number of counts. The data refer to a beam of* ^{16}O *of* 200 MeV/u *which hits against a* 0.5 *cm thick C target.*

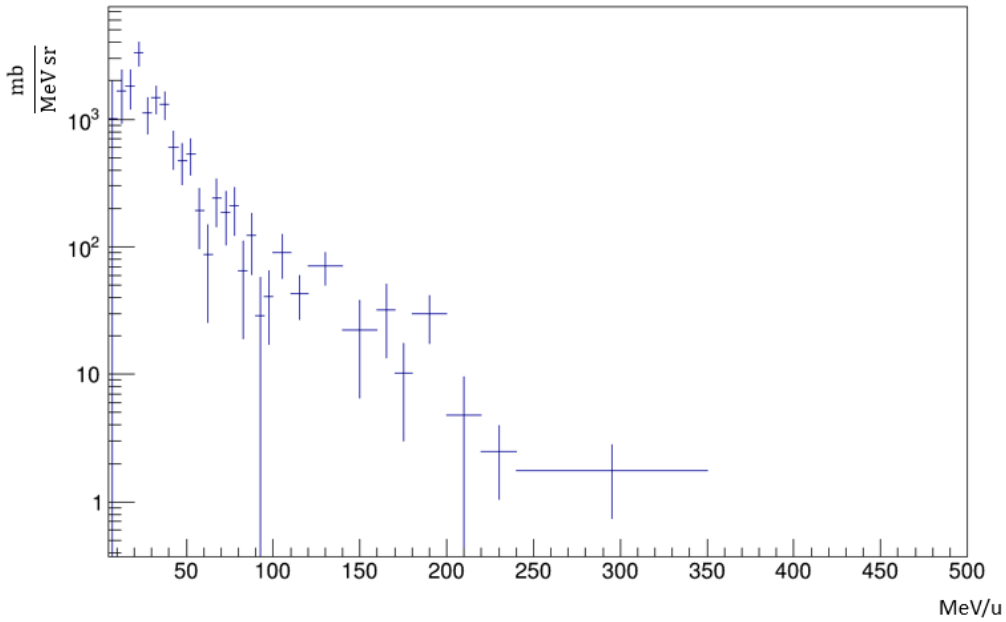

Figure 3.32: *Energy-differential cross section on detector 2 as a function of energy in logarithmic scale. The error on the energy is equal to the bin width, whereas the error associated to the cross section is given by* $\sigma\frac{1}{\sqrt{N}}$ *where N represents the number of counts. The data refer to a beam of* ^{16}O *of* 200 MeV/u *which hits against a* 0.5 *cm thick* $(C_2H_4)_n$ *target.*

In Figure 3.33, Figure 3.34 and in Figure 3.35 the energy-differential cross section for an oxygen beam hitting against a target of carbon and polyethylene with a thickness equal to 0.5 cm and a target of polyethylene 1 cm thick are reported respectively.

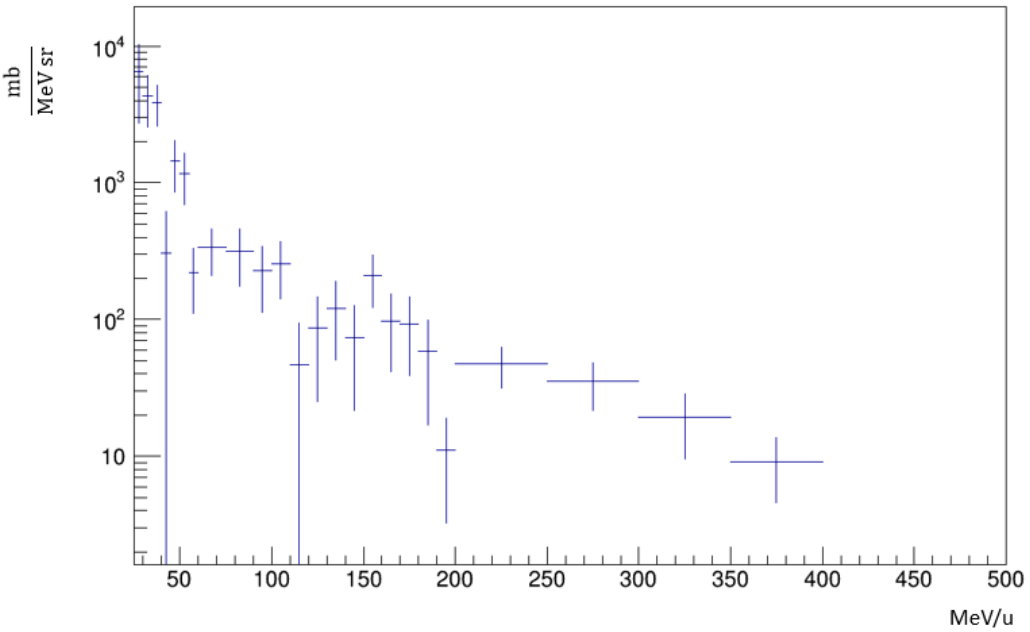

Figure 3.33: *Energy-differential cross section on detector 2 as a function of energy in logarithmic scale.The error on the energy is equal to the bin width, whereas the error associated to the cross section is given by* $\sigma\frac{1}{\sqrt{N}}$ *where* N *represents the number of counts. The data refer to a beam of* ^{16}O *of* 400 MeV/u *which hits against a* 0.5 *cm thick* C *target.*

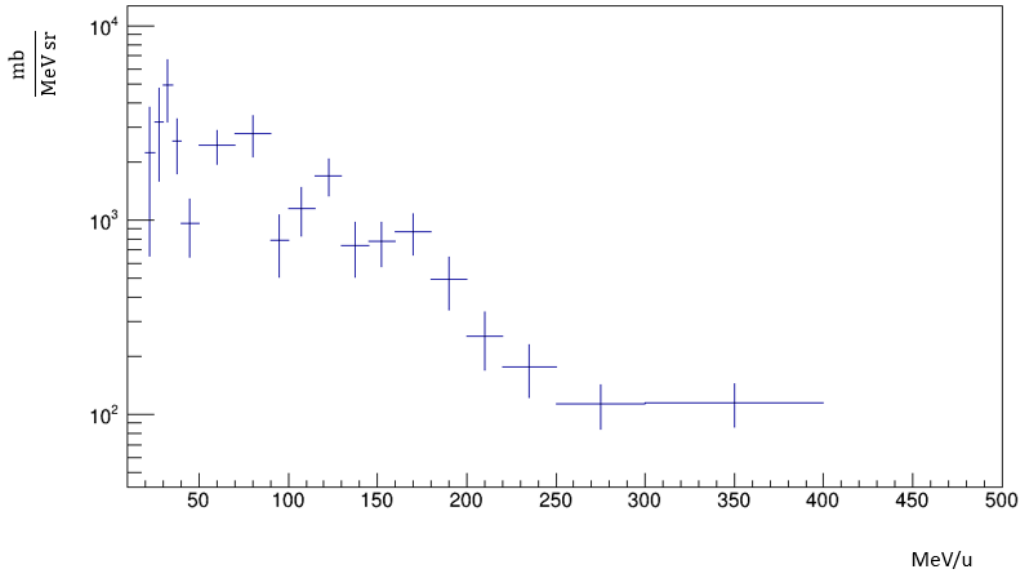

Figure 3.34: *Energy-differential cross section on detector 2 as a function of energy in logarithmic scale.The error on the energy is equal to the bin width, whereas the error associated to the cross section is given by* $\sigma\frac{1}{\sqrt{N}}$ *where N represents the number of counts. The data refer to a beam of* ^{16}O *of* 400 MeV/u *which hits against a* 0.5 *cm thick* $(C_2H_4)_n$ *target.*

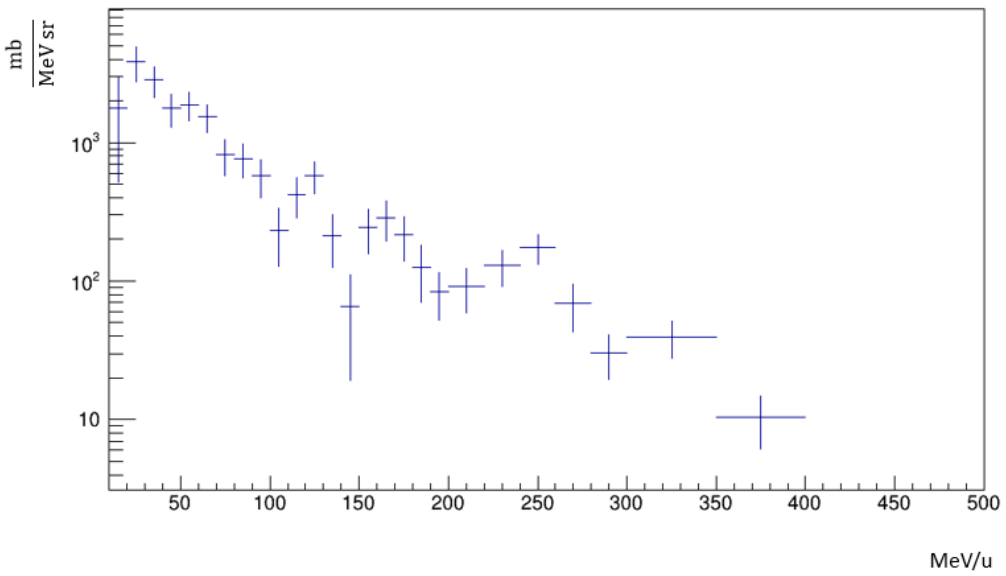

Figure 3.35: *Energy-differential cross section on detector 2 as a function of energy in logarithmic scale.The error on the energy is equal to the bin width, whereas the error associated to the cross section is given by* $\sigma\frac{1}{\sqrt{N}}$ *where N represents the number of counts. The data refer to a beam of* ^{16}O *of* 400 MeV/u *which hits against a* 1 *cm thick* $(C_2H_4)_n$ *target.*

The behaviour of the curves are similar. The peak amplitude is bigger and the energy range is wider if the beam energy is 400 MeV/u. The peaks are always under 50 MeV independently on the kind of material and target thickness.

Conclusions

The *FragmentatiOn Of Target* FOOT experiment has the aim to carry out measurements of differential cross section regarding the projectile and target fragments when the incoming ion beams (p, ^{4}He, ^{12}C, ^{16}O) hit against targets (H, C, O) of interest for hadrontherapy and radio protection in space. Of particularly interest is the study of the target fragmentation because the available data in literature is very poor due to the technical difficulty to detect them because of their low energy and therefore short range. FOOT faces this problem by means of an inverse kinematic approach i.e. inverting the beam and the target roles; the difficulty to have an hydrogen target forces the experiment to deal with polyethylene and carbon targets, thus retrieving the cross section on H by difference. Due to the low range, for the target fragmentation it is enough to evaluate the differential cross section with respect to kinetic energy, while for the projectile it is necessary to evaluate it also with respect to the production angle. In order to identify and track both the light and heavy charged fragments, a magnetic spectrometer and an emulsion chamber detector are used allowing a very good efficiency and identification capacity in a dynamical range that goes from protons to ^{16}O ions. Since during the fragmentation reactions also neutrons can be produced, an upgrade of the FOOT experiment is planned: the BC-501A liquid scintillator detector has been chosen for its timing properties and for a very good neutrons and gamma-rays discrimination capability.

In this thesis the analysis regarding the production of secondary particles is performed on several data sets, acquired at the GSI laboratory, in Darmstadt, Germany [38] with the aim to perform the neutron-gamma discrimination. The beam considered are ^{16}O ions, with energies of 200 MeV/u and 400 MeV/u, impinging on graphite and polyethylene targets with a thickness of 0.5 cm and 1 cm, respectively. In order to select only neutral particles, a plastic scintillator has been placed in front of the BC-501A as a veto to detect and inhibit charged fragments. The set-up consists of two BC-501A scintillators each one with its veto scintillator, put at angles of 26.8 deg and 24.5 deg with respect to the beam direction. Thanks to the veto scintillators a discrimination between charged and neutral particles has been performed and exploiting the electric pulse emitted by the organic liquid scintillators, a shape discrimination among gamma-rays and neutrons is performed. In this way, the neutrons characterization is performed and their energy and differential cross section are calculated.

The pulse shape discrimination is the technique used to distinguish neutrons from gamma rays and it consists of a signal shape analysis. The signal exiting from the neutron detector is composed by a prompt (given by gammas) and a slow (given by neutrons) component. In this work, three different analysis selections have been performed. In the first one, it is required to have the amplitude of the signals exiting from the neutron detector bigger than a fixed threshold. In order to apply the second and the third one, the time of flight and the area fast and area slow of each digitized signals are extracted. The gamma-rays time of flight is directly obtained by dividing the target to the detector distance by the velocity of light. For the other particles, the time-of-flight was experimentally measured from the difference between the start counter and the stop signal from the neutron detector. The time-of-flight distribution measured by the neutron detector is composed by a prompt (given by gamma- rays produced in the interaction of the primary beam with the target) and a slow (given by neutrons and also gamma-rays produced in the interaction of secondary particles with detectors and environmental materials) component, simultaneously fitted by two Gaussian distributions. In this way the signal attributable only to gamma-rays are separated from the ones generated by both neutrons and gamma-rays.

For what the Pulse shape discrimination concerns, the digitized signals from the BC-501A detectors were analyzed in term of the fast component and slow component. More in detail, the fast component of each signal has been found by taking the signal area from the rising edge to the time corresponding to 20% of the maximum after the peak itself. A similar procedure is applied to find the slow component in which it is taken the area of the signal from 20% of the maximum after the peak to the time value at which the signal goes to zero.The neutron-gamma discrimination has been obtained comparing the slow and the total area. The neutron-gamma discrimination has been obtained comparing the slow to the total area. The neutron energy is calculated through the time-of-flight method. Finally, the energy-differential cross section for the neutron production in the reactions $^{16}O + (C_2H_4)_n$ and $^{16}O + C$ is calculated. In order to find it, the detector efficiency has been evaluated with a Fluka simulation. The cross-section has a peak at low energy which goes to zero with increasing energy. The differential cross-section has been evaluated also with a larger energy beam of oxygen at 400 MeV/u showing that the behaviour of the curve is the same, the main difference is given by the peak amplitude which is bigger in the case of a polyethylene target. In all cases, the maximum of the differential cross section is below 50 MeV independently on the kind of material and target thickness. It is possible to notice that the number of neutrons tends to grow with the energy. In fact, 3 neutrons are produced for each primary when the beam energy is 200 MeV/u, whereas 10 neutrons are produced for each primary when the beam energy is 400 MeV/u. However, these results are upper limits because of the background.

The aims of this analysis, which was to study the performances of the neutron detector, has been achieved and the apparatus has discriminated the neutrons from the gamma-rays. A preliminary energy-differential reaction cross section for the production

of neutrons in the $^{16}O + (C_2H_4)_n$ and $^{16}O + C$ reactions has been calculated at two different beam energy even if the statistic collected was not very reach. New measurements should be done in order to increase the statistic and obtain more precise results.

Appendix A

Chemical structure of materials

Polymethyl methacrylate, PMMA [22]

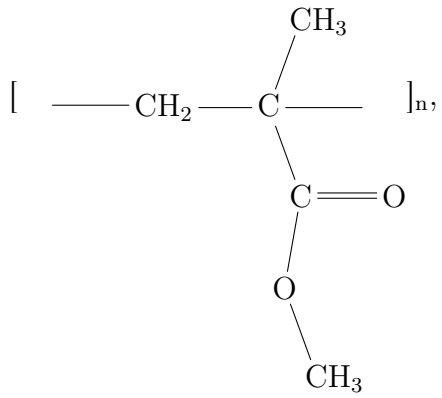

Mylar, polyethylene terephthalate [22]

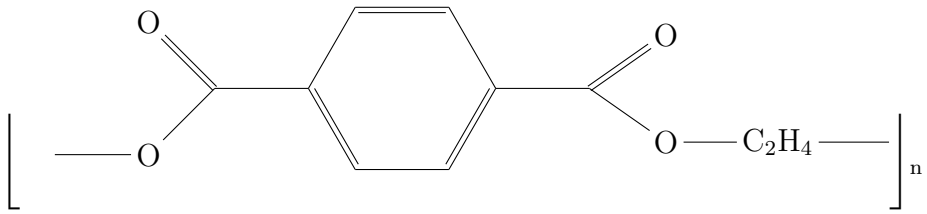

Benzene [22]

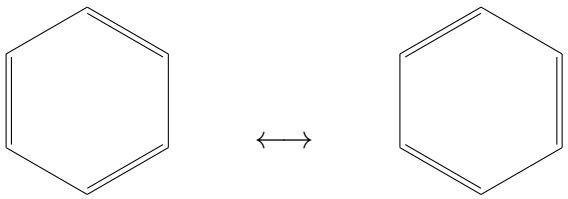

Anthracene, composed by three condensed benzene rings,[22]

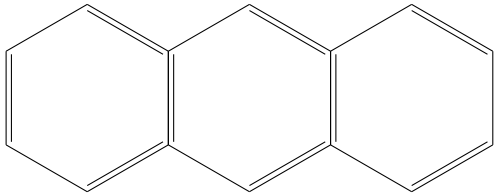

Naphtalene, composed by two condensed benzene ring, [22]

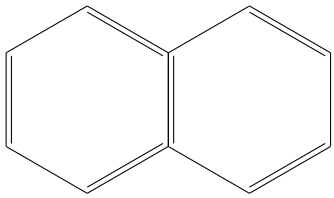

Trans-stilbene, i.e. trans-1,2-diphenylethene [22]

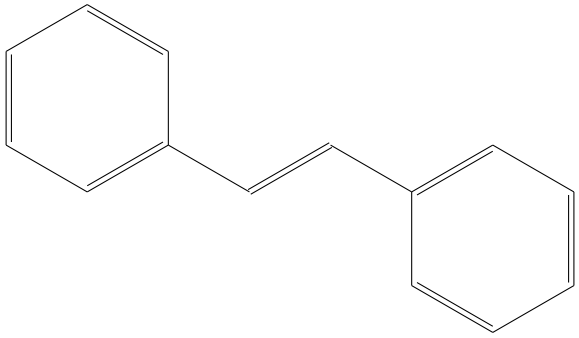

Polystyrene [22]

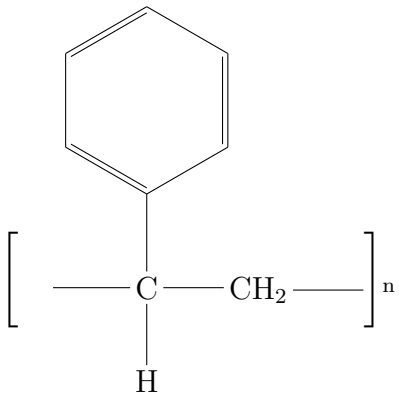

p-Therphenyl [22]

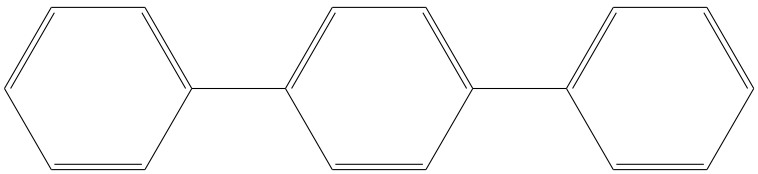

POPOP [22]

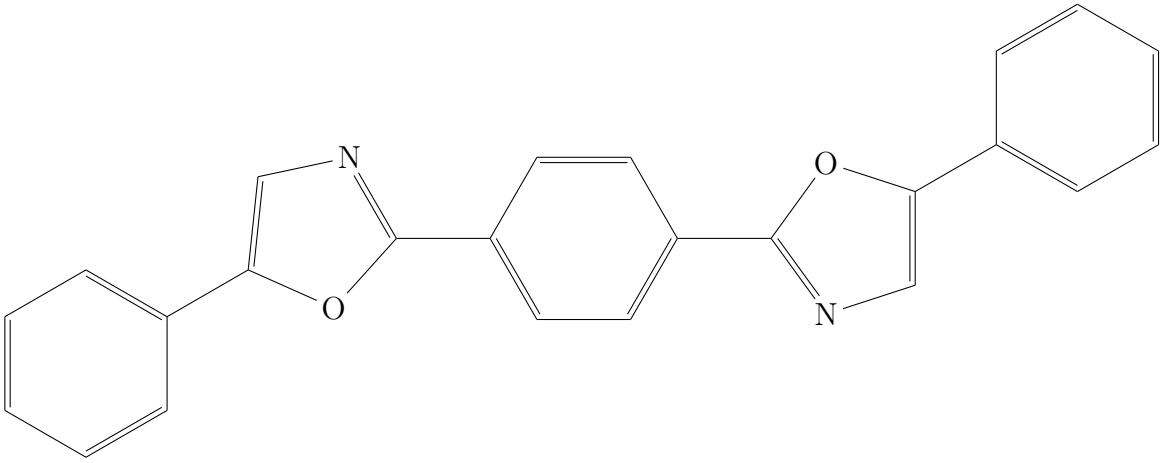

Toluene [22]

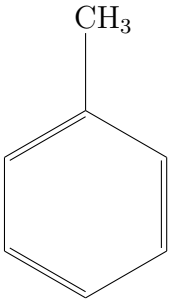

Xylene [22]

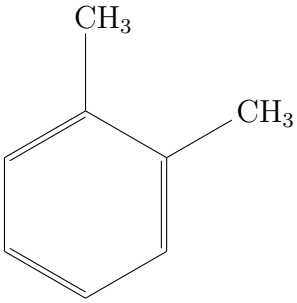

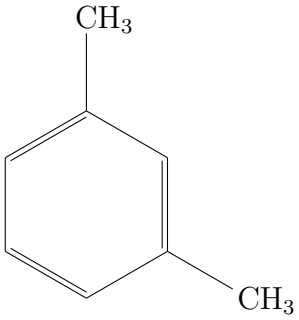

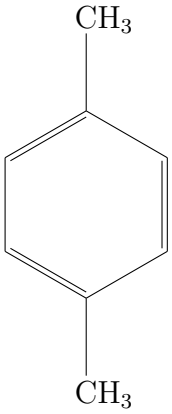

Decaline [22]

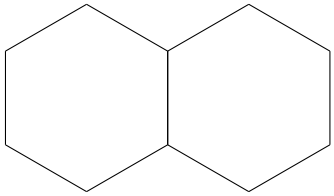

Bibliography

[1] W.R. Leo. *Techniques for Nuclear and Particle Physics Experiments: A How - To Approach.* Springer, 1987.

[2] Altieri. Interazione delle particelle cariche con la materia.

[3] Delmastro. particle interactions in particle detectors.

[4] W. H. Barkas. *Nuclear research emulsions.* Academic Press, New York and London, 1963.

[5] E. Gioscio. *Ottimizzazione di un metodo di ray tracing applicato a piani di trattamento adroterapici.* Master thesis, Sapienza, Università di Roma, Facoltà di Ingegneria Civile ed Industriale Corso di Laurea in Ingegneria Biomedica, 2012.

[6] G. Sartorelli. *Notes of the course of Laboratory of Nuclear and Subnuclear Physics 1.* University of Bologna, October 2018.

[7] S. Meroli. The straggling function. energy loss distribution of charged particles in silicon layers.

[8] R. Serber. *Nuclear reactions at high energy.* Physical Review Journals, 1947.

[9] G. Cuttone. Physics: Fragmentation, dosimetry, simulation, modeling.

[10] C. Zeitlin C. La Tessa. *The Role of Nuclear Fragmentation in Particle Therapy and Space Radiation Protection.* Frontiers, 29 March 2016.

[11] R. Spighi. *Notes of the course of Applied Nuclear Physics: Medicine.* University of Bologna, A.Y. 2019-2020.

[12] A. Bacquiasa V. Föhra D. Henzlovaa A. Kelić-Heil M.V. Ricciardi K.H. Schmidt. *Dispersion of longitudinal momentum distributions induced in fragmentation reactions.* Physical Review, November 8th, 2011.

[13] S. John L. W. Townsend J. W. Wilson and R. K. Tripathi. *Geometric Model From Microscopic Theory for Nuclear Absorption.* NASA Technical Paper 3324, July 1993.

[14] Freiburg University. Interaction of neutral particles with matter.

[15] H. Hirayama. *Lecture Note on Photon Interactions and Cross Sections*. KEK, High Energy Accelerator Research Organization, 2000.

[16] F. Operetto. Un'unit'a didattica sull'effetto compton a partire da dati sperimentali.

[17] G.F. Knoll. *Radiation detection and measurement*. John Wiley & Sons, Inc, Third edition.

[18] NASA Human Research Program Engagement and Communications. *Space Radiation*. NASA Human Research Program Engagement and Communications, 2019.

[19] A. Rizzo V. Zaconte L. Narici M. Casolino L. Di Fino M. Larosa P. Picozza. *Performances of Kevlar and Polyethylene as radiation shielding on-board the International Space Station in high latitude radiation environment*. Scientific Reports, 2017.

[20] DUPONT. Kevlar.

[21] G. De Leo S. Fasano E. Ginelli. *Biologia e Genetica*. Edises Università, 2020.

[22] T.W. Graham Solomons C.B. Fryhle. *Chimica organica*. Zanichelli, 2008.

[23] A.I. Kassis. *Therapeutic Radionuclides: Biophysical and Rdaiobiological Principle*. Harvard Medical School, Seminar in nuclear medicine, October 2008.

[24] Przemek M. Krawczyk Nicolaas A. P. Franken. *Comparison of RBE values of high-LET α-particles for the induction of DNA-DSBs, chromosome aberrations and cell reproductive death*. Academisch Medisch Centrum Universiteit van Amsterdam and Amsterdam University Medical Center, 2011.

[25] M. Endo. Robert r. wilson (1914–2000): the first scientist to propose particle therapy—use of particle beam for cancer treatment, October 2017.

[26] E. Bührer. Radiotherapy with particle beams.

[27] M. Anwar Chaudri. *Secondary Neutron Production from Patients during Hadrontherapy and their Radiation Risks: the Other Side of Hadrontherapy*. Institute of Biomaterials, F. A. University of Erlangen-Nuernbeg, 2013.

[28] Nasa. Space home, https://science.nasa.gov.

[29] L. Scavarda. *The Foot Experiment: Measuring Proton and Light Nuclei Fragmentation Cross Sections up to 700 MeV/A*. Bulletin of the Russian Academy of Sciences. Physics, 2020.

[30] S. Biondi. *The FragmentatiOn Of Target Experiment (FOOT) and its DAQ system.* ResearchGate, October 2020.

[31] S. M. Valle. *Design, simulation and performances study of the FOOT experiment.* Università degli studi di Milano, 2018-2019.

[32] G. Ambrosij S. Argiròb A. Alexandrova G. Battistoni N. Belcarid S. Biondie. *FOOT Conceptual Design Report.* ResearchGate, August 2017.

[33] G. Battistoni M. Toppi V. Patera The FOOT Collaboration. *Measuring the Impact of Nuclear Interaction in Particle Therapy and in Radio Protection in Space: the FOOT Experiment.* Frontiers in Physics, February 2021.

[34] F. Meng. Development and improvement of cerium activated gadolinium gallium aluminum garnets scintillators for radiation detectors by codoping.

[35] Wolle. Scintillators – general characteristics.

[36] R. Paschotta. Quenching.

[37] Saint-Gobain crystals. https://www.crystals.saint-gobain.com/radiation-detection-scintillators/liquid-scintillators/neutron-gamma-psd-bc-501a-bc-519.

[38] GSI. www.gsi.de/en/about_us.

[39] M. Sénoville F. Delaunay M. Pârlog N.L. Achouri N.A. Orr. *Neutron-γ discrimination with organic scintillators: Intrinsic pulse shape and light yield contributions.* HAL open science, 2021.

[40] J. Scherzinger R. Al Jebali J.R.M. Annand K.G. Fissum R. Hall-Wilton K. Kanak iM. Lundin B. Nilsson H. Perrey A. Rosborg H. Svensson. *The light-yield response of a NE-213 liquid-scintillator detector measured using 2–6 MeV tagged neutrons.* ELSEVIER, 2016.

[41] Particle Data Group. http://pdg.lbl.gov.